Tuning and Characterization of Self-assembled Plasmonic Nanoparticle Arrays

Oral Ualibek

School of Physics

Trinity College Dublin

A thesis submitted to the University of Dublin, Trinity College, in application for the degree of

Doctor of Philosophy

30th September 2014

Declaration

This thesis is submitted by the undersigned for examination for the degree of Doctor of Philosophy at the University of Dublin. It has not been submitted as an exercise for a degree at any other University.

Apart from the advice, assistance and joint effort mentioned in the under signed and in the text, is entirely my own work.
I agree, that the library may lend or copy this thesis freely upon request.

Oral Ualibek

Dated: September 2014

Summary

This thesis details the development and use of a novel nano-entity fabrication technique. The technique is based on a glancing angle deposition (GLAD) on transparent stepped templates. It is demonstrated that the technique is functionally independent of the deposited material as evidenced by the growth of ordered nanoparticle (NP) arrays of Ag, Au and Cu. Furthermore, the morphology of the systems grown can be changed through choice of the deposition parameters. This allows a complete tuning of the plasmonic resonances measured mainly with reflectance anisotropy spectroscopy. Finally, the self-assembled noble metal NP arrays have been used as building blocks for Surface Enhanced Raman Spectroscopy (SERS) experiments, demonstrating a strong enhancement in the Raman signal measured.

This thesis is divided into seven chapters. After a brief introduction, Chapter 1 provides an overview of the theoretical background of the plasmonic resonance and an outline of the current state of the art in this area. Chapter 2 describes experimental methods and equipment used throughout the whole thesis. The operating principles, particular features and special advantages of the equipment related to all experiments are shown. Also the theory of specific tools is described. Chapter 3 introduces the faceting mechanism and the tunable features of the different substrates such as Al_2O_3, MgO and $SrTiO_3$. The production process of the Ag NP arrays on the dif-

ferent substrates and tuning of the morphology by changing the substrate periodicity is shown. Chapter 4 describes the tuning of the morphology of the Ag NP arrays through choice of the substrate temperature and via post annealing. By fabricating arrays of Au and Cu NPs by the GLAD technique, it is also shown that the plasmonic resonance energy can be controlled through choice of NP material, initial stepped template periodicity and the deposition thickness. The influence of capping on the plasmonic resonances of Ag NP arrays will be investigated. Chapter 5 deals with experimental and theoretical investigation of out-of-plane optical responses of Ag and Au NP arrays. Chapter 6 demonstrates the application of GLAD-grown NP arrays for SERS substrates. Conclusions and future work are finally presented in the last chapter.

Acknowledgements

Let me use a couple of pages to thank a number of wonderful people that supported and helped me during these 4 years of study. Without their warm support and help I could not have carried out this study. Foremost, I want to thank my supervisor Prof. Igor Shvets, for giving me the opportunity to study a PhD in his research group, supporting me with useful advice and keeping me motivated. The biggest thanks to Dr. Ruggero Verre, I will forever be thankful for his supervision and warm support from beginning to end of my PhD studies. Thanks for teaching me this work, from experiment to theory. Even though he has moved to Sweden, he has still helped me as much as he can. At the very beginning I did not understand much about my research project, but he kindly taught me again and again until I understood, I thank him for his patience. I would like to especially thank Dr. Brendan O'Dowd for his help on how to use the experimental tools and how to use the software products related to the experiments. Thanks for his neat correction of my thesis; I will never forget all his help. He is one of the kindest and most helpful people I have ever met. A warm of thanks to Dr. Karsten Fleischer, for all his guidances, useful advices, discussions and clear explanations. Another big thanks to Dr. Victor Usov for being my first co-supervisor, and teaching me my research project. I'm very grateful for Ehsan's help, thanks for his working with me nearly for three years on the SERS project. The experiments were many times unsuccessful, but he did not stop helping and worked with me until we got results. Thanks for all his

patience. Thanks to Brendan Bulfin helping me with COMSOL simulations. Also I would like to thank to Dr. Danny Fox and Dr. Mircea Modreanu for their helping on transmission electron microscopy and spectroscopic ellipsometry. Thanks to Cormac, Barry, Leo, Daragh for giving me advice and correcting my PhD thesis. Thanks to Ellen Bowman and Jeanette Cummins for their big help with administrative issues. Thanks to all the Applied Physics Research Group and CRANN members.

I want to start a new paragraph, because their help will never ever be forgotten. Very big thanks to my best friends Olzat, Azat and Askar. We studied at the same university in Kazakhstan, then we came together to Ireland to study a PhD degree. During the past few years they have been very close to me, they always supported me when I hit any problems or difficulties. Also a great thanks to Saken, Ozhet and Nurlan. Thanks to my friends in Kazakhstan: Jumagali, Aidyn, Sagyndyk, Kairat and Aitkazy.

"Life is nothing without love" - is a nice quote. I really believe this and it is a real truth. Thanks to my fiancée Riza for her love and being with me through the ups and downs of life. Thanks for her sincerely support me all the time. A huge "thank you" to my parents for all the moral support and the amazing chances they have given me over the years. Also the greatest thanks to my brothers, sisters and sisters-in-law for all their support.

Lastly, thanks to my curators Meruert Sarsetova and Elvira Myrzaliyeva in the Center for International Programs, Kazakhstan. Finally, I would like to acknowledge the support of the Government of Republic of Kazakhstan under the Bolashak programme.

Publications:

1. **O. Ualibek**, R. Verre, K. Fleischer, B. Bulfin and I. V. Shvets .

   The influence of capping material on plasmonic resonances of self-assembled Ag NP arrays. (*In preparation*).

2. **O. Ualibek**, E. Rezvani, R. Verre, K. Fleischer, B. Bulfin, O. Toktarbaiuly, J. J. Wang, G. S. Duesberg and I. V. Shvets .

   Highly uniform and tunable SERS substrates produced by glancing angle deposition. (*In preparation*).

3. R. Verre, M. Modreanu, **O. Ualibek**, D. Fox, K. Fleischer, C. Smith, H. Zhang, M. Pemble, J. F. McGilp and I. V. Shvets.

   General approach to the analysis of plasmonic structures using spectroscopic ellipsometry. *Physical Review B*, **87**, 235428 (2013).

4. **O. Ualibek**, V. Verre, B. Bulfin, V. Usov, K. Fleischer, J. F. McGilp and I.V. Shvets.

   Manipulating and probing the growth of plasmonic nanoparticle arrays using light. *Nanoscale*, **5**, 4923 (2013).

5. R. Verre, K. Fleischer, **O.Ualibek** and I.V. Shvets.

   Self-assembled broadband plasmonic nanoparticle arrays for sensing applications. *Applied Physics Letters*, **100**, 031102 (2012).

List of Abbreviations:

AFM	Atomic Force Microscopy
ASEF	Anisotropic Surface Excess Function
EF	Enhancement Factor
EM	ElectroMagnetic
FEM	Finite Element Method
FF	Fill Factor
FIB	Focused Ion Beam
FOM	Figure Of Merit
FWHM	Full Width Half Maximum
GLAD	Glancing Angle Deposition
IR	Infrared
IT	Interband Transition
LPR	Localised Plasmon Resonance
NIR	Near Infra-Red
NP	Nanoparticle
PEM	Photoelastic Modulator
RAS	Reflectance Anisotropy Spectroscopy
R6G	Rhodamine 6G
SDA	Surface Dielectric Anisotropy
SE	Spectroscopic Ellipsometry
SERS	Surface-Enhanced Raman Spectroscopy
SEM	Scanning Electron Microscope
SERS	Surface Enhanced Raman Spectroscopy
TEM	Transmission Electron Microscope
UHV	Ultra High Vacuum
UV	Ultra-Violet
Vis	visible

Contents

Declaration i

Summary iii

Acknowledgements v

List of Publications vii

List of abbreviations ix

Introduction **1**

1 Theoretical Background **7**

1.1 The Optical Properties of Metals 9

1.1.1 Dielectric Function of a Material 9

1.1.2 Drude Model and The Dielectric Function of The Noble Metals 10

1.2 Mie Theory 12

1.3 Polarizability of A Small Metallic Particle 13

1.3.1 For A Small Sphere 13

1.3.2 For A Small Ellipsoid 15

1.3.3 For A Coated Particle 16

1.4 Substrate Effects on The Plasmon Resonance 18

1.5 Plasmonic Resonances in Nanoparticle Arrays 20

1.6 Models of Nanoparticle Arrays 21

1.6.1 Three Layer Model 21
1.6.2 The Transfer Matrix Formalism 23
1.6.3 Advanced Numerical Model 26

2 Experimental Methods **29**
2.1 Glancing Angle Deposition 29
2.2 The Deposition Chamber 31
2.3 Reflectance Anisotropy Spectroscopy 33
2.3.1 Applications and Theory 33
2.3.2 System Description 35
2.4 Ultraviolet-Visible Spectroscopy 36
2.5 Spectroscopic Ellipsometry 37
2.6 Atomic Force Microscopy 39
2.7 Scanning Electron Microscopy 40
2.8 Raman Spectroscopy 41
2.9 High Temperature Furnace 42

3 Substrate Preparation and Growth of the Nanoparticle Arrays **45**
3.1 Substrate Preparation: Faceting Mechanism 46
3.1.1 c-plane Al_2O_3 46
3.1.2 MgO and $SrTiO_3$ 48
3.2 Growth of Ag Nanoparticle Arrays 49
3.2.1 Experimental Procedure 49
3.2.2 Ag NP Grown on Different Substrates 50
3.2.3 The NP Morphology Dependence on Substrate Periodicity . . . 52

4 Tuning and Characterization of Plasmonic Nanoparticle Arrays **55**

4.1 The Optical Properties of Substrates 56
4.2 The Equivalence Between Absorption and RAS 57
4.3 The Plasmonic Resonance of Ag NP Arrays Grown on Different Substrates 59
4.4 The *In-situ* Plasmonic Resonances of Ag NPs on Al_2O_3 60
4.5 Temperature Controlled Manipulation of NP Properties 62
4.5.1 Dependency of the NP Morphology Upon Changes in the Substrate Temperature 62
4.5.2 Theory and Discussion 65
4.5.3 The Manipulation of Ag NP Arrays Using Radiation Annealing 70
4.6 Au and Cu NP Arrays 72
4.7 The Influence of Capping Material 76

5 Investigation of The Out-of-plane Optical Response 81
5.1 Introduction 82
5.1.1 Plasmonic Studies Using Spectroscopic Ellipsometry 82
5.1.2 ASEF and Plasmonic Modelling 83
5.2 Experiment 85
5.3 Results and Discussion 86
5.4 Extension to A More General Formalism 89
5.5 Extensive Investigation: Au NP Arrays 97

6 Ag Nanoparticle Arrays for SERS Applications 101
6.1 Introduction: SERS in Plasmonic Nanostructures 102
6.2 Experimental Details 103
6.3 Experimental Results 105
6.4 SERS Enhancement Dependence on Input Light Polarization 107
6.5 SERS Enhancement Dependence on Plasmonic Resonance Maximum . 109

6.6 Enhancement Factor, Comparison of Theory and Experiment 111

7 Conclusions and Future Work **113**

7.1 Conclusion 113

7.2 Future work 115

References **118**

References 118

Introduction

> If you thought that science was certain - well, that is just an error on your part.
>
> Richard P. Feynman

Metal nanoparticles (NPs) have attracted significant scientific attention in the last decade [1–3]. In particular, localised plasmon resonance (LPR) effects of the NPs have provided substantial advantages in many fields such as biological analysis by enhanced luminescence or Raman scattering [4, 5] and optical circuits[6, 7]. A wide range of applications is possible as the plasmonic properties of metal NPs can be tuned by changing their size and shape [8]. Particular interest has been focused in the area of coupled NPs [9, 10] as they provide more flexibility and advanced functionalities. Coupled NP arrays have been used as building blocks for wave guides [11–14] and to increase solar cell efficiency [15–17]. Furthermore, the local electric field enhancement in the gap region between closely spaced NPs has been utilised in surface enhanced Raman spectroscopy [18], second harmonic generation [19], enhanced fluorescence [20] and optical tweezers [21]. The majority of these devices are based on planar geometries, preferably with NPs uniformly dispersed over large areas.

Different methods have been developed to produce metallic NP arrays, but many challenges still remain. Among the various methods in fabrication, Electron Beam

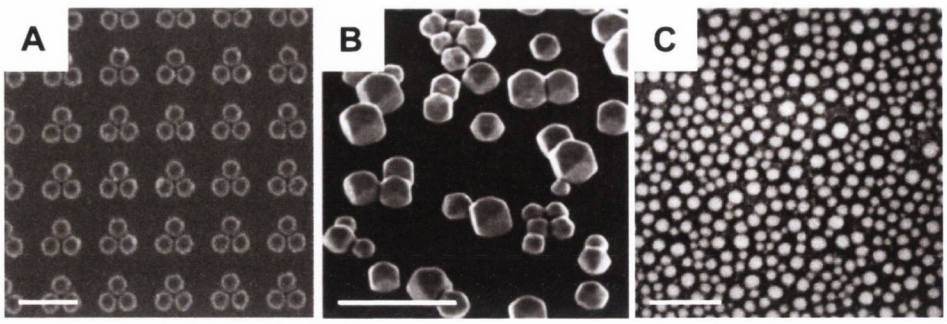

Figure 1: A set of SEM images of Au NPs produced by EBL (A), colloidal fabrication (B) and pulsed laser annealing (C). The scale bares are 400 nm (A), 100 nm (B) and 200 nm (C). The images taken from [25–27].

Lithography (EBL) is a well known technique for fabrication of a desired pattern with high controllability over size and position of patterned entities [22–24] (see Figure 1A). In EBL, a radiation sensitive polymer is coated on a conducting substrate and the required pattern is etched onto the resist polymer layer by a focused electron beam. This patterned resist layer is then used as a sacrificial mask for depositing a material. After growing the material, the mask is removed by a lift-off step. Finally, a desired structure appears on the substrate surface. However, this technique is limited in its applications: the whole production process is time-consuming, cannot be sufficiently up-scaled and requires a high cost clean room for fabrication. Nanosphere lithography [28] or nanoimprint lithography [29] can also produce these nanostructures. Nevertheless, these methods also are either time-consuming, expensive or not scalable. On the other hand, large-scalable non-lithographic nanofabrication methods such as pulsed laser annealing [30, 31] and colloidal nanoparticle synthesis [32, 33] are less expensive and much more simple. Unfortunately these methods also have drawbacks; the NPs produced by these methods are randomly distributed on the surface with random gap sizes (see Figure 1B and C), which makes it difficult to tune and model the optical properties.

Recently, we developed a different fabrication method based on deposition at a

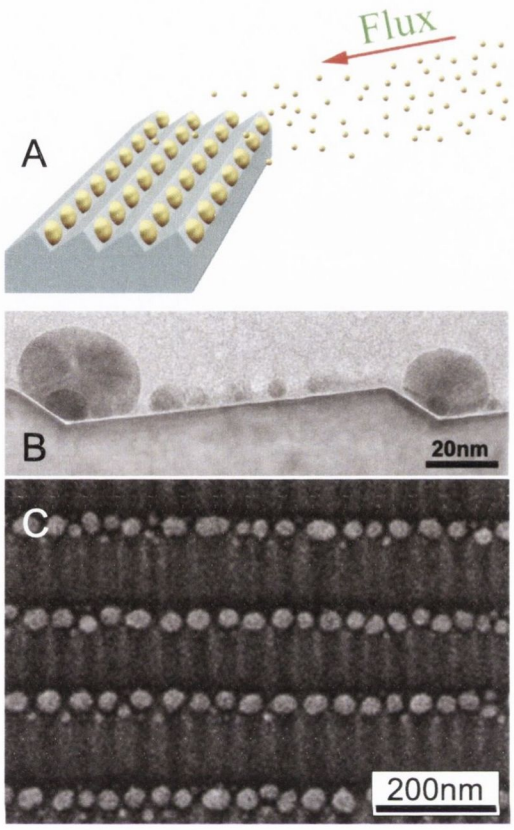

Figure 2: (A) A schematic view of the GLAD technique: a flux of collimated ad-atoms is sent towards the stepped template surface at a glancing angle (A). In this way one can grow asymmetric NP arrays. The cross section TEM (B) and in-plane SEM (C) images of Ag NP arrays grown by GLAD technique.

glancing angle on a stepped template [34–39]. Adatoms are evaporated towards a stepped template surface at shallow angles of incidence. The step edge shadows part of the surface during the deposition and highly ordered NPs are created by self-assembly on the step edge (see Figure 2). The principle, often referred to as glancing angle deposition (GLAD) [40, 41], is simple and is mainly based on geometrical considerations, rendering it largely independent of the deposited material in the case of step shadowing [42]. A typical example of GLAD-based Ag NP array is shown in Figure 2B and C. The surfaces are decorated by chains of highly ordered NPs.

Whenever NPs are deposited onto a substrate, an accurate control of the parameters

governing the growth is important for tailoring the resulting NP morphology and for growth reproducibility. Material properties, substrate temperature [43], adatom flux [44], step periodicities of the substrate [39], pressure and the direction of the adatom plume towards the substrate [45] play a crucial role in the growth. Changes in one or several parameters results in a modified plasmonic response due to changes in the NP morphology. However, the effect of each individual parameter is difficult to separate from the others. In order for such a self-assembled production method to be competitive, the effect of each deposition parameter on the growth condition needs to be well understood and controlled.

One solution is real time monitoring of optical properties of the system as it is being fabricated. This provides information on the growth mechanism and allows production of structures with the desired optical characteristics. In the case of physical vapour depositions this route is complicated as the growth is usually performed in a vacuum environment. Different optical methods, such as spectroscopic ellipsometry [46–48], polarized reflectivity [43] and reflectance anisotropy spectroscopy (RAS) [38], have been used for monitoring the growth evolution. We have recently utilised RAS to measure *in-situ* the optical response of NP arrays grown by the morphology of the NPs. In this thesis in particular, it will be shown:

- The GLAD-based NP arrays are highly ordered and strongly coupled.
- It is possible to monitor the real-time *in-situ* optical response of the system during material growth.
- The GLAD technique is a simple and alternative production method, independent on the deposition material. Ag, Au and Cu NP arrays can be grown.
- Ag NP arrays can be deposited on different (Al_2O_3, MgO and $SrTiO_3$) stepped substrates.

- The NPs morphology can be tuned through choice of the substrate temperature and via post annealing.
- This plasmonic resonance can be controlled over the visible range through appropriate choice of the step periodicity of the substrate and the deposition material.
- The out-of-plane optical response of Au and Ag NP arrays investigated with spectroscopic ellipsometry.
- It will be demonstrated that GLAD grown NP arrays can be used as a SERS substrate, and that the SERS enhancement depends on the plasmonic resonance energy and the input light polarization.

Chapter 1

Theoretical Background

> Theory helps us bear our ignorance of facts.
>
> George Santayana

When the dimensions of metallic nanoparticles (NPs) are very small, light can easily penetrate the NP and cause oscillation of the conduction band electrons. The interaction of electromagnetic radiation and NP results in a displacement of the conduction electrons with respect to the positive ion cores of that the metallic lattice (see Figure 1.1). A restoring force takes place due to Coulomb attraction resulting in an oscillatory

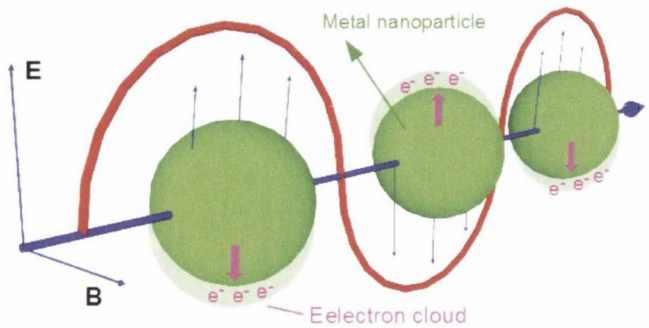

Figure 1.1: Schematic view of the plasmonic oscillation for a metal nanosphere, showing the displacement of the conduction electron charge cloud relative to the nuclei.

Figure 1.2: Lycurgus cup under ambient lighting appears green, but when illuminated from inside the cup it appears red. Image taken from [50].

behaviour. The oscillations do not distribute on a large distance and only occur within the NP scale, for this reason it is called "localised plasmon resonances" (LPRs). This particular optical feature of metallic NPs is different from solids and molecules. The exact energy of plasmon resonance depends on the geometry of the NP, it is dimensions, the effective electron mass, the density of electrons, the surrounding medium and dipolar coupling [49]. In this thesis a brief overview will be introduced to describe the plasmonic features of the metal NPs based on a classical theory.

One of the oldest manmade objects which utilises plasmonic phenomena is a 4^{th} Century Roman artefact known as the Lycurgus cup [50, 51]. Under ambient lighting it appears green, but when illuminated from inside, it appears red (see Figure 1.2). This fascinating behaviour has been explained by the plasmonic theory. The Roman cup is made of a ruby glass which contains small quantities of silver and gold NPs. The transmission and reflection properties of the cup are different due to the presence of plasmonic NPs. At the time of its manufacture, of course, the cause of this effect was was completely unknown, since the NPs are invisible even with the use of an optical microscope. In 1857, Michael Faraday prepared gold colloids by reduction of gold chloride solution with phosphorus. He observed that the colors of the NPs varied with their size [52]. Half a century later in 1908, Gustav Mie established a clear theory

on the scattering and absorption of electromagnetic radiation on small homogeneous spherical particles by solving the Maxwell equation [53]. This formalism is now known as *Mie theory* and it has been utilised by successors as a fundamental theory for the description of LPRs in metallic NPs.

Nowadays, the study of plasmonics has become a wide field in physics and many potential applications have been identified. The variety of the topics on plasmonics are derived in a part due to the scale and breadth of modern sciences. The following chapter will provide an overview of the theoretical background behind LPR and an outline of the current state of the art in this area.

1.1 The Optical Properties of Metals

1.1.1 Dielectric Function of a Material

Before discussing the optical properties of metals, the dielectric function of a material needs to be introduced. The dielectric function $\varepsilon(\omega)$ is a frequency-dependent complex quantity which describes the polarizability and absorption behaviour of a material, and can be written as

$$\varepsilon(\omega) = \varepsilon'(\omega) + i\varepsilon''(\omega), \tag{1.1}$$

where $\varepsilon'(\omega)$ and $\varepsilon''(\omega)$ are real and imaginary parts of the dielectric function. Generally speaking, $\varepsilon'(\omega)$ describes how much of a material is polarized when interacting with an electric field as a result of the generation of electric dipoles in the material. The absorption of a material is represented by $\varepsilon''(\omega)$, and so for a transparent material $\varepsilon''(\omega) \approx 0$. In addition, $\varepsilon'(\omega)$ is approximately constant for transparent materials, so the dielectric function $\varepsilon(\omega)$ is approximately constant. The plot of $\varepsilon(\omega)$ for metals, and in particular noble metals, is likely to have a sharp peak across a narrow frequency

region. A more detailed description of the optical features of the noble metals will be presented in the following sections. If a material is homogeneous and its optical response is linear across a certain range, then the dielectric function is directly related to the electric susceptibility $\chi(\omega)$

$$\varepsilon(\omega) = \chi(\omega) + 1. \tag{1.2}$$

The electric susceptibility measures a material's response to an applied electric field $\mathbf{E}$ and polarization $\mathbf{P}$ of average dipole moment $\mathbf{p}$ per unit value of the medium. The relation between $\mathbf{P}$ and $\mathbf{E}$ is known from the Maxwell's equation

$$\mathbf{P} = \varepsilon_0 \chi \mathbf{E}, \tag{1.3}$$

where ε_0 is the electric permittivity of free space.

1.1.2 Drude Model and The Dielectric Function of The Noble Metals

When the electronic and optical properties of a metal are related only to the conduction electrons, the metal is then known as a free-electron metal. These electrons can be easily excited by an electromagnetic wave, hence why they are referred as "free" electrons. Alkali metals in particular and in some cases noble metals are commonly refereed to as "free electron metals" [8].

The description of free-electron dynamics can be obtained from a simple approach called the Drude model [54] (in some literature called Drude-Lorentz-Sommerfeld model [55]). This model describes the influence of the external forces on the conduction electrons in a metal particle. In this model, the free-electron system is considered as

a damped harmonic oscillator, with all electrons acting in phase with one another. If the mass and charge of the electron are given by m_e and e respectively, and the electric field $\mathbf{E} = \mathbf{E}_0 e^{-i\omega t}$ oscillates with a frequency ω, then the expression for the motion of the electron is given by

$$m_e \frac{\partial^2 \mathbf{r}}{\partial t^2} + m_e \Gamma \frac{\partial \mathbf{r}}{\partial t} = e\mathbf{E}_0 e^{-i\omega t}, \tag{1.4}$$

where Γ is the phenomenological damping constant and $\mathbf{r}$ is the displacement from equilibrium. This differential equation presents the relaxation state of the system without any restoring force. The inclusion of the force originating from the dipole moment gives rise to well-defined eigenfrequencies of the oscillating electron. By considering the dipole moment $\mathbf{p} = e\mathbf{r}_0$ and the polarization $\mathbf{P} = N\mathbf{p}$, where N is number of the electrons per unit volume, the equation 1.4 can be easily solved. For simplification, let us assume the dielectric function is uniform throughout the particle, and that $\mathbf{P} \parallel \mathbf{E}$. We then obtain

$$\varepsilon = 1 + \frac{P}{\varepsilon_0 E}, \tag{1.5}$$

by inserting the $\mathbf{P} = N\alpha\mathbf{E}$ to the equation 1.5, the dielectric function of system my be written as

$$\varepsilon - 1 = \frac{1}{\varepsilon_0} N\alpha, \tag{1.6}$$

where α is the polarizability of system. Therefore, the dielectric function in equation 1.1 for alkali metals can be given by:

$$\varepsilon(\omega) = 1 - \frac{\omega_p^2}{\omega^2 + i\omega\Gamma} = 1 - \frac{\omega_p^2}{\omega^2 + \Gamma^2} + i\frac{\omega_p^2}{\omega(\omega^2 + \Gamma^2)}, \tag{1.7}$$

where ${\omega_p}^2 = Ne^2/m_e\varepsilon_0$ is the Drude plasma frequency and is a characteristic frequency that indicates the optical response of a material. The relaxation constant Γ is determined by the electron mean free path l with $\Gamma = \upsilon_F/l$, where υ_F is Fermi velocity. If

$\varepsilon \gg \Gamma$, the real and imaginary part of dielectric function of free-electron metals can be presented as:

$$\varepsilon'(\omega) \approx 1 - \frac{\omega_p^2}{\omega^2}, \quad \varepsilon''(\omega) \approx 1 - \frac{\omega_p^2}{\omega^3}\Gamma. \tag{1.8}$$

For certain materials such as Au and Cu the interband (IB) transitions play an important role in their optical response. In the visible range the equation 1.2 then becomes

$$\varepsilon(\omega) = 1 + \chi(\omega) + \chi^{IB}(\omega), \tag{1.9}$$

where $\chi^{IB}(\omega)$ is the interband transition susceptibility. Kreibig and Vollmer treated the $\chi^{IB}(\omega)$ in their study by using the band structure $E(\mathbf{k})$ and transition matrix elements M and by describing interband transitions between initial (i) and final (f) states [8]:

$$\chi^{IB} = \frac{8\hbar^3\pi e^2}{m_{eff}^2}\sum_{i,f}\int_{BZ}\frac{2d\mathbf{k}}{(2\pi)^3}|\mathbf{e}M_{if}(\mathbf{k})|^2\Big\{\frac{1}{[E_f(\mathbf{k}) - E_i(\mathbf{k})][(E_f(\mathbf{k}) - E_i(\mathbf{k}))^2 - \hbar^2\omega^2]}$$
$$+ i\frac{\pi}{2\hbar^3\omega^2}\delta[E_f(\mathbf{k}) - E_i(\mathbf{k}) - \hbar\omega]\Big\}, \tag{1.10}$$

where the integral is over the Brillouin zone (BZ) and $\mathbf{e}$ is the unit vector along the direction of the electric field. The calculated value of χ^{IB} for Au and Cu will be shown in Section 4.6 by an analytical simulation.

1.2 Mie Theory

The general approach for the diffraction problem of an isolated small metal sphere within the framework of electrodynamics was presented for the first time in 1908 by Gustav Mie [53]. He solved Maxwell's equations with a boundary condition in spherical coordinates by applying a multipole expansion of the incoming electromagnetic field.

The parameters of the calculations were the dimensions of the spherical particle and the dielectric function of both the particle itself and the material in which it was embedded. The scalar electromagnetic potentials were obtained from the various fields of each component, and the extinction and scattering coefficients were calculated as a solution.

In particular, when the radius of the particle R is much smaller than the wavelength of incident light $R \ll \lambda$, the dipolar mode is the dominant contribution and the absorption profile can be expressed as [56]:

$$\sigma_{abs} = 9\frac{\omega}{c}(\varepsilon_m)^{3/2}V_0\frac{\varepsilon''(\omega)}{(\varepsilon'(\omega) - 2\varepsilon_m)^2 + (\varepsilon''(\omega))^2}, \tag{1.11}$$

where V_0 is its volume and ε_m is the dielectric constant of the surrounding medium. However, Mie theory is limited within the frame of the electrodynamics of the plasmonic particles. In this model the particles are assumed isolated and the interactions of particles were not considered [3]. In addition, Mie theory is limited to the calculation of the optical properties of spherical particles only [55].

1.3 Polarizability of A Small Metallic Particle

1.3.1 For A Small Sphere

The following is a description of the plasmonic properties of a small metallic sphere using a classical quasi-static approximation when the radius of the sphere is much smaller than the exciting wavelength ($R \ll \lambda$). If is assumed that the dielectric function of the NP, ε_{NP}, is uniform throughout its volume. It is assumed that the positive charges in the metal sphere are immobile while the negative charges associated with the conduction electrons are movable under the effects of the external fields. Hence a

displacement of the negative charges with respect to the positive charges takes place if the sphere is located in an electric field. The external electric field $\mathbf{E}_0$ generates a charge only on the sphere surface and by using the boundary conditions the polarization at the sphere surface can be calculated. The internal field is

$$\mathbf{E}_i = \mathbf{E}_0 \frac{3\varepsilon_m}{\varepsilon_{NP} + 2\varepsilon_m}. \tag{1.12}$$

The polarizability α for a small sphere can be found through the relation between dipole moment and external field $\mathbf{p} = \varepsilon_m \alpha \mathbf{E}_0$, which gives us [8]

$$\alpha = 4\pi R^3 \frac{\varepsilon_{NP} - \varepsilon_m}{\varepsilon_{NP} + 2\varepsilon_m}. \tag{1.13}$$

The dielectric functions ε_m and ε_{NP} are to be substituted by their frequency dependent values $\varepsilon_m(\omega)$ and $\varepsilon_{NP}(\omega)$. In this case ε_m is taken as a real constant for the visible range and a resonance frequency for the system can be found. We can see that resonance occurs in equation 1.13 when the denominator is minimised, i.e. when

$$|\varepsilon_{NP} + 2\varepsilon_m| = \text{Minimum}, \tag{1.14}$$

in other words

$$[\varepsilon'_{NP}(\omega) + 2\varepsilon_m]^2 + [\varepsilon''_{NP}]^2 = \text{Minimum}. \tag{1.15}$$

This indicates that a negative ε'_{NP} is required to ensure a correct phase relation between the electric field and NP polarization. In the case where $\varepsilon''_{NP} \ll 1$ the resonance condition can simply be given by:

$$\varepsilon'_{NP} = -2\varepsilon_m. \tag{1.16}$$

This condition is suitable for noble metal NPs in the visible range. The absorption and scattering value of the metal NP (C_{abs} and C_{sca} respectively) are dependent on polarizability with [55]

$$C_{abs} = k\mathrm{Im}(\alpha) = k\frac{\varepsilon''_{NP}}{(\varepsilon'_{NP} - \varepsilon_m)^2 + (\varepsilon''_{NP})^2}$$
$$C_{sca} = \frac{k^4}{6\pi}|\alpha|^2, \tag{1.17}$$

where k ($k = \omega/c$) is the wave vector of the incident light.

1.3.2 For A Small Ellipsoid

The previous section described about the polarizability of a spherical metallic NP by applying the quasi-static approximation. However, the NPs grown by GLAD technique are ellipsoidal in shape as will be shown in Chapter 3, and so it will be necessary to formulate an expression for the polarizability of an ellipsoidal metallic NP. This can be achieved through the use of appropriate electromagnetic boundary conditions according to previous discussions. The standard equation for the surface of an ellipsoid with semi axes $R_i (i = x, y, z)$ is given by

$$\frac{x^2}{R_x^2} + \frac{y^2}{R_y^2} + \frac{z^2}{R_z^2} = 1. \tag{1.18}$$

By using equation 1.18 the correct potential can be defined with the coordinates of the ellipsoid and the polarizability of the ellipsoidal metallic NP can be written as [8, 55]

$$\alpha_i = \frac{4\pi R_x R_y R_z}{3}\frac{\varepsilon_{NP} - \varepsilon_m}{\varepsilon_m + L_i(\varepsilon_{NP} + \varepsilon_m)}, \tag{1.19}$$

where L_i is the shape depolarization factor (with $i = x, y, z$), which depends on the geometry of the NP. The shape depolarization factor must sum to 1, i.e. $\sum_i Li = 1$. In the special case of a sphere the three shape depolarization factor must be equal, i.e. $L_x = L_y = L_z = 1/3$, but for the general case of an ellipsoidal NP we have $L_x \neq L_y \neq L_z$. The individual L_i may be given by

$$L_i = \frac{R_x R_y R_z}{2} \int_0^\infty \frac{dq}{(R_i^2 + q) f(q)}, \tag{1.20}$$

where $f(q) = [(q + R_x^2)(q + R_y^2)(q + R_z^2)]^{1/2}$ and q being point charge associated with the dipole moment $p = qd$.

While a spherical NP will have resonance frequency ω_{res} independent of the direction of **E**, an ellipsoidal NP will have resonance values associated with each axis. Hence, the resonance frequencies are a function of the geometry of the ellipsoidal NP. The resonance frequency $\omega_{res,i}$ for an electric field direction along i-axis is found in previous literature by using equation 1.7 and 1.19 [57]

$$\omega_{res,i} = \sqrt{\frac{\omega_p^2}{\varepsilon_\infty + (\frac{1-L_i}{L_i})\varepsilon_m} - \Gamma^2}. \tag{1.21}$$

1.3.3 For A Coated Particle

In this present study, the material which coats the NPs will have a significant influence on their plasmon resonance, as will be shown in the Section 4.7. For this reason, it is necessary to calculate the polarizability of a coated ellipsoidal NP. If is assumed once more that the NP is embedded within a material with dielectric function ε_m, but in addition we now assume an ellipsoidal shell having semi axes $S_i (i = x, y, z)$ and dielectric function ε_s. It is further assumed that the core and shell have a similar aspect ratio, i.e. S_i/R_i is for constant for $i = x, y, z$. Since the shell is also an ellipsoid,

its surface can be given by

$$\frac{x^2}{S_x^2} + \frac{y^2}{S_y^2} + \frac{z^2}{S_z^2} = 1. \tag{1.22}$$

The shell thickness along the i-axis is given by $S_i - R_i$. The polarizability of the coated ellipsoidal NP can be written as [55]

$$\alpha = \frac{V\big((\varepsilon_s - \varepsilon_m)[\varepsilon_s + (\varepsilon_{NP} - \varepsilon_s)(L_c - \zeta L_s)] + \zeta\varepsilon_s(\varepsilon_{NP} - \varepsilon_s)\big)}{\big([\varepsilon_s + (\varepsilon_{NP} - \varepsilon_s)(L_c - \zeta L_s)][\varepsilon_m + (\varepsilon_s + \varepsilon_m)L_s] + \zeta L_s\varepsilon_s(\varepsilon_{NP} - \varepsilon_m)\big)}, \tag{1.23}$$

where $V = 4\pi S_x S_y S_z/3$ is the total volume of the NP including the shell, $\zeta = R_x R_y Rz/S_x S_y S_z$ is the fraction of the whole NP volume occupied by the core ellipsoidal NP, and L_c and L_s are the depolarization factor of the core and shell respectively. For the shell ellipsoid the shape depolarization factor can be written as

$$L_{s,i} = \frac{S_x S_y S_z}{2} \int_0^\infty \frac{dq}{(S_i^2 + q)f(q)}. \tag{1.24}$$

In a special case where the coated NP is spherical in shape, the shape depolarization factors must be identical, i.e. $L_{c,x} = L_{c,y} = L_{c,z} = L_{s,x} = L_{s,y} = L_{s,z} = 1/3$ and polarizabilities assume same values $\alpha_x = \alpha_y = \alpha_z$. Hence, the polarizability of the coated spherical NP is written as

$$\alpha = 4\pi R^3 \frac{(\varepsilon_s - \varepsilon_m)(\varepsilon_{NP} + 2\varepsilon_m) + \zeta(\varepsilon_{NP} - \varepsilon_s)(\varepsilon_m + 2\varepsilon_s)}{(\varepsilon_s + 2\varepsilon_m)(\varepsilon_{NP} + 2\varepsilon_m) + \zeta(2\varepsilon_s - 2\varepsilon_m)(\varepsilon_{NP} - \varepsilon_s)}. \tag{1.25}$$

The influence of the coated layer on the resonance condition is related to the dielectric function of shell material and its thickness. This effect has been studied experimentally and theoretically, the results will be shown in Section 4.7.

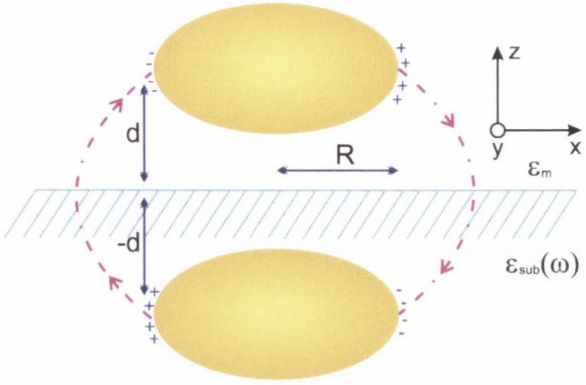

Figure 1.3: A schematic view of the real and image dipole. The centre of the NP is placed above a flat substrate at the distance d, and a point dipole moment $\mathbf{p}$ is located at the centre of the NP. The presence of the substrate is modelled by considering an image dipole moment $\mathbf{p}'$ placed within the substrate. The electric field produced by the image dipole modifies the electric field in the vicinity of the NP.

1.4 Substrate Effects on The Plasmon Resonance

In the previous section, the plasmon resonance of an isolated NP in a uniform dielectric medium was described by a dipolar approximation. When the NP is placed on a substrate an interruption of the homogeneity takes place in the dielectric medium and the dielectric function of the surrounded medium assumes different quantities. Hence, the substrate influences the anisotropic optical response of the NP due to the polarizability of the substrate material and in turn this effect causes a red shift of the resonant frequency in the calculation [58].

The substrate effect on the plasmon resonance is treated by use of an image charge method within the quasi-static approximation [59]. In this approach, the center of the NP is placed above a flat substrate at a distance d, a point dipole moment $\mathbf{p}$ is located at the centre of the NP (see Figure 1.3). The presence of the substrate is modelled by considering an image dipole moment $\mathbf{p}'$ placed within the substrate [58–60]. When an electric field is applied parallel or perpendicular to the substrate surface, the real

dipole and image dipole are related by

$$\mathbf{p}' = F\mathbf{p}, \tag{1.26}$$

where F is the image factor written as

$$F = \frac{\varepsilon_{sub} - \varepsilon_m}{\varepsilon_{sub} + \varepsilon_m}, \tag{1.27}$$

where ε_{sub} is the frequency dependent dielectric function of the substrate and ε_m is the dielectric function of the medium in which the NP is embedded. An electric field is produced by the image dipole which will influence the NP.

The image charge effects on the optical response of the oblate ellipsoidal NP is clearly explained in recent literature by M. Valamanesh *et al.* [61]. In this study the cause of the red shift of the plasmon resonance was found to be the small distance between the dipole and its image dipole. In the following the main results of the image charge effects will be shown by using the dipolar and quadrupolar approximation.

In this approach we consider an oblate spheroidal NP and an axis of revolution perpendicular to the substrate surface. For the case of a spherical NP the shape depolarization factors can be written as [58, 59]:

$$\begin{aligned} \tilde{L}_{x,y} &= L_{x,y} - \frac{1}{24}\frac{R^3}{d^3}F \\ \tilde{L}_z &= L_z - \frac{1}{12}\frac{R^3}{d^3}F, \end{aligned} \tag{1.28}$$

where $\tilde{L}_i$ are the effective shape depolarization factors of the spherical NP, and L_i are the shape depolarization factors for the simpler case where no substrate is present. Valamanesh *et al.* showed that this approach can be adapted for the case of a spheroidal

NP (having $R_x = R_y > R_z$) as follows:

$$\tilde{L}^*_{x,y} = L_{x,y} + \frac{1}{2}F\left(1+\xi^2\right)\left\{\left(\frac{3}{2}+\xi^2\right)\xi^2 \ln\left(1+\frac{1}{\xi^2}\right) - \xi\,\mathrm{atan}\left(\frac{1}{\xi}\right) - \xi^2\right\}$$
$$\tilde{L}^*_z = L_z + F\left(1+\xi^2\right)\left\{\left(\frac{3}{2}+\xi^2\right)\xi^2 \ln\left(1+\frac{1}{\xi^2}\right) - \xi\,\mathrm{atan}\left(\frac{1}{\xi}\right) - \xi^2\right\}, \qquad (1.29)$$

where $\tilde{L}^*_i$ are the effective shape depolarization factors and $\xi = 1/(r^2-1)^{1/2}$ is a function of the aspect ratio ($r = R_x/R_z$) of the spheroidal NP. It transpires that the effective distance of the image change from the substrate surface, d^* is greater than d. The effective distance is found in previous literature [57] by using equations 1.28 and 1.29

$$d^* = \left(-\frac{R_x R_y R_z}{12(1+\xi^2)\{(\frac{3}{2}+\xi^2)\xi^2 \ln(1+\frac{1}{\xi^2}) - \xi\,\mathrm{atan}(\frac{1}{\xi}) - \xi^2\}}\right)^{\frac{1}{3}}. \qquad (1.30)$$

The effect of the image charge is to cause a red shift or a reduction in the excitation energy.

1.5 Plasmonic Resonances in Nanoparticle Arrays

The previous discussion relates solely to the case of isolated NPs. When the NPs are arranged in an array and exited by an electromagnetic field, a strong near-field coupling between the NP takes place, and the resonance energy is shifted relative to that of the isolated NPs. When the electric field is aligned with the chains of NPs (see Figure 1.4A), the negative charges of the NPs are displaced towards the positive charges of their neighbours, which causes a reduction in the plasmonic excitation energy. Conversely, when the electric field is directed perpendicularly to the chains NPs (see Figure 1.4B), the distribution of the charge density involves a repulsion between neighbouring NPs, causing an increase in the excitation energy. The magnitude of these red and blue shifts depends on the dimensions of the NPs and the inter-particle separation.

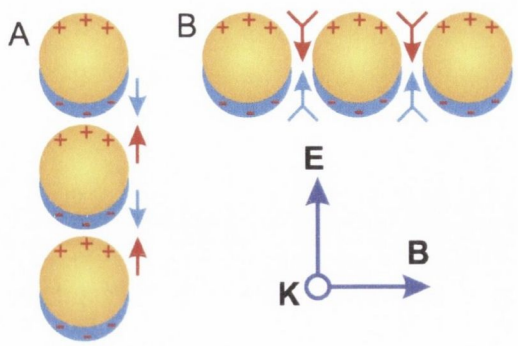

Figure 1.4: A schematic illustration of interparticle attraction. **K** is the travelling direction of the electromagnetic wave (if the wave is travelling into or out of the page).

1.6 Models of Nanoparticle Arrays

1.6.1 Three Layer Model

The following section will describe an analytical model for simulating plasmonic behaviour of the NP arrays. The model was originally developed by J. D. E. Mcintyre and D. E. Aspanes [62] and was modified to allow for anisotropic media by R. Verre *et al.* [39, 57]. The system under consideration is a three layer structure, consisting of an array of ellipsoidal metallic NPs sandwiched between two homogeneous layers, namely the substrate and the vacuum or capping layer. The top and bottom layers are optically isotropic, while the NP array layer has an effective dielectric function ε_L given by

$$(\varepsilon_L - \varepsilon_m)\mathbf{E} = N\varepsilon_m \alpha \mathbf{E}_{loc}, \tag{1.31}$$

where N is number of NPs per unit area, $\mathbf{E}$ is the electromagnetic field inside the anisotropic layer and $\mathbf{E}_{loc}$ is the local electric at each of the individual NP. The local field $\mathbf{E}_{loc}$ is given by the sum of the applied electric field $\mathbf{E}_{ext}$, the field generated by the substrate (calculated by considering an "image charge", as discussed in Section

1.4) $\mathbf{E}_{im}$, and the electric field generated by neighbouring NPs $\mathbf{E}_{int}$, i.e.

$$\mathbf{E}_{loc} = \mathbf{E}_{ext} + \mathbf{E}_{im} + \mathbf{E}_{int}. \tag{1.32}$$

These electric fields can be separately written as

$$\begin{aligned} E_{int,i} &= \frac{1}{4\pi}\alpha_i E_{loc,i}\Upsilon_i \\ E_{im,i} &= \frac{1}{4\pi}\alpha_i E_{loc,i} F\Upsilon_{im,i} \\ E_{ext,i} &= E_{loc,i}(1+\alpha_i\beta_i), \end{aligned} \tag{1.33}$$

where Υ and β are equal to

$$\Upsilon_i = \sum_j \frac{3\cos^2\theta_{ij} - 1}{r_j^3}, \quad \beta_i = \frac{1}{4\pi}(-\Upsilon_{int,i} - F\Upsilon_{im,i}), \tag{1.34}$$

where θ_{ij} is the angle between the axes of the dipoles of neighbouring NPs and r_j is the center-to-center distance of dipoles in array. Finally, the authors [39, 57] derived the dielectric function of the ellipsoidal NP arrays using equations 1.31 and 1.33 with $\xi = (x, y)$ by applying boundary conditions of the Maxwell equations

$$\begin{aligned} \varepsilon_{L,\xi} &= \varepsilon_m\left(1 + \frac{N\alpha_\xi}{1+\alpha_\xi\beta_\xi}\right) \\ \frac{1}{\varepsilon_{L,z}} &= \frac{1}{\varepsilon_m}\left(1 - \frac{N\alpha_z}{1+\alpha_z\beta_z}\right). \end{aligned} \tag{1.35}$$

This approach was applied to simulate the plasmon resonance of the NP arrays and the results will be shown in Chapter 4 and 5.

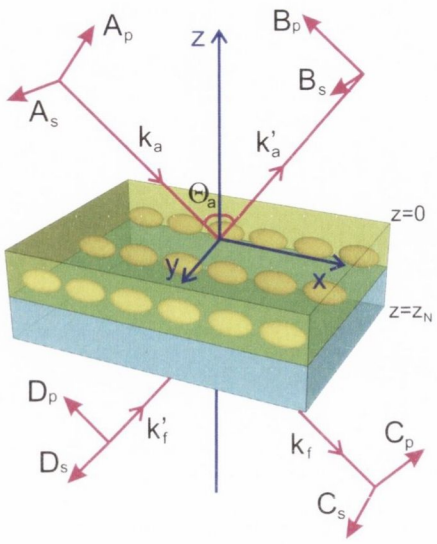

Figure 1.5: The polarized p and s modes of the incident $\mathbf{k}_a$, reflected $\mathbf{k}'_a$ and transmitted $\mathbf{k}'_f$ wave vectors. The back side incoming wave vector is not included to the system, i.e. $D_p = D_s = 0$.

1.6.2 The Transfer Matrix Formalism

The previous section described how a three layer model can be used to simulate the optical response of the NP arrays. However, this model has several strict conditions. It applies to a three layer phase system (substrate, plasmonic layer and air), the nanocomposite layer must be thin, the substrate response must be isotropic, and optical axes are assumed to be aligned with the high symmetry axes of the system. In particular, this approach becomes inaccurate when multilayer structures or thick plasmonic layers are considered, rendering its application limited to very specific cases. In this section a more general formalism based on a transfer matrix approach will be shown. This model was originally formulated for an isotropic system [63], and later it was adapted for anisotropic layers by Berreman [64] and Schubert [65, 66].

This formalism may be applied to a layered structure with parallel interfaces. An incident electromagnetic wave with the wave vector $\mathbf{k}_a$ is sent to the incident media at an incident angle Θ_a and then it is reflected with a wave vector $\mathbf{k}'_a$ (see Figure

1.5). The complex amplitudes of the incident wave are given by A_p, A_s, where p and s denote the p and s polarised modes. Similarly the complex amplitudes of the reflected wave are given by B_p, B_s, and those of the exit wave $\mathbf{k}_f$, which is transmitted through the system, are given by C_p, C_s. There is no incoming wave from the back side ($\mathbf{k}'_f$), therefore the complex amplitudes of $\mathbf{k}'_f$ are both equal to zero, i.e. $D_p = D_s = 0$. The polarized p and s components of the electric and magnetic field vectors ($\mathbf{k}_a, \mathbf{k}'_a, \mathbf{k}_f, \mathbf{k}'_f$) can defined by a general 4×4 transfer matrix for a layered structure

$$\begin{pmatrix} A_s \\ B_s \\ A_p \\ B_p \end{pmatrix} = \mathbf{T} \begin{pmatrix} C_s \\ D_s \\ C_p \\ D_p \end{pmatrix} = \begin{pmatrix} T_{11} & T_{12} & T_{13} & T_{14} \\ T_{21} & T_{22} & T_{23} & T_{24} \\ T_{31} & T_{32} & T_{33} & T_{34} \\ T_{41} & T_{42} & T_{43} & T_{44} \end{pmatrix} \begin{pmatrix} C_s \\ 0 \\ C_p \\ 0 \end{pmatrix}. \tag{1.36}$$

The transfer matrix $\mathbf{T}$ can be given by the product of partial transfer matrices $\mathbf{t}_i$ (where i denotes the i^{th} of N layers within the structure) as well as the incident and exit matrices, $\mathbf{L}_a$ and $\mathbf{L}_f$ respectively. I.e.

$$\mathbf{T} = \mathbf{L}_a^{-1} \prod_{i=1}^{N} \mathbf{t}_i(-d_i)\, \mathbf{L}_f \tag{1.37}$$

where d_i is the thickness of the i^{th} layer. The individual partial transfer matrices can each be given as a sum over complex scalars β_j

$$\mathbf{t}_i = \exp\left(i\frac{\omega}{c}\mathbf{\Delta} d_i\right) = \beta_0 \mathbf{I} + \beta_1 \mathbf{\Delta} + \beta_2 \mathbf{\Delta}^2 + \beta_3 \mathbf{\Delta}^3 \tag{1.38}$$

where $\mathbf{I}$ is the unit matrix, ω is the angular frequency, $\mathbf{\Delta}$ is a matrix related to the dielectric tensor of the system and wave vector components. β_j must obey the following

equation [65]:

$$\exp\{i\frac{\omega}{c}q_k d\} = \sum_{j=0}^{3} \beta_j q_k^j, \quad k = 1, ..., 4, \tag{1.39}$$

where q_i are the eigenvalues of matrix $\mathbf{\Delta}$. The matrix $\mathbf{\Delta}$ of the capping layer and the NP layer is given by [67]

$$\mathbf{\Delta} = \begin{pmatrix} 0 & 0 & 0 & 1-(\sin^2\Theta/\varepsilon_z) \\ 0 & 0 & -1 & 0 \\ 0 & -\varepsilon_y + \sin^2\Theta & 0 & 0 \\ \varepsilon_x & 0 & 0 & 0 \end{pmatrix}. \tag{1.40}$$

It is assumed that in the case of the capping layer, the dielectric function is constant, i.e. $\varepsilon_x = \varepsilon_y = \varepsilon_z = \varepsilon_{cap}$.

The inverse of the incident and exit matrices $\mathbf{L}_a$ and $\mathbf{L}_f$ introduced in equation 1.37 can be given by

$$\mathbf{L}_a^{-1} = \begin{pmatrix} 0 & \frac{1}{2} & -\frac{1}{2}\sec\Theta & 0 \\ 0 & \frac{1}{2} & \frac{1}{2}\sec\Theta & 0 \\ -\frac{1}{2}\sec\Theta & 0 & 0 & \frac{1}{2} \\ -\frac{1}{2}\sec\Theta & 0 & 0 & \frac{1}{2} \end{pmatrix}, \tag{1.41}$$

$$\mathbf{L}_f = \begin{pmatrix} 0 & 0 & \sqrt{1-(\sin^2\Theta/\varepsilon_{sub})} & 0 \\ 1 & 0 & 0 & 0 \\ \sqrt{\varepsilon_{sub} - (\sin^2\Theta/\varepsilon_{sub})} & 0 & 0 & 0 \\ 0 & 0 & \sqrt{\varepsilon_{sub}} & 0 \end{pmatrix}. \tag{1.42}$$

Where ε_{sub} is the dielectric function of the substrate. The complex reflection coefficient of the system is required to simulate the optical response, which is given by using the

components of **T**

$$r_{ss} = \frac{B_s}{A_s} = \frac{T_{21}T_{33} - T_{23}T_{31}}{T_{11}T_{33} - T_{13}T_{31}},$$
$$r_{pp} = \frac{B_p}{A_p} = \frac{T_{11}T_{43} - T_{13}T_{41}}{T_{11}T_{33} - T_{13}T_{31}}. \tag{1.43}$$

Finally the pseudo-dielectric function $< \varepsilon_i >$ $(i = x, y)$ of the system for spectroscopic ellipsometry is given by

$$< \varepsilon_i >= \sin^2\Theta + \sin^2\Theta\tan^2\Theta\Big(\frac{T_{21}T_{33} - T_{11}T_{43}}{T_{21}T_{33} + T_{11}T_{43}}\Big)^2. \tag{1.44}$$

The dielectric functions of the capping, substrate and NP material are known. The dimensions, separations and capping thickness were chosen to match experimental conditions. This model was used to describe the samples measured experimentally, and as shall be shown in Chapters 4 and 5, a good agreement was found between the experimental and theoretical results.

1.6.3 Advanced Numerical Model

The previous sections have described the analytical models for anisotropic optical responses of NP arrays. However, certain aspects such as quadrupolar resonances, estimations of the electrical field distribution between the NPs, or the influence of the NP shape (spherical, hemispherical, truncated spheres) cannot be investigated by simple analytical models. For a more general approach, numerical simulations were performed using the finite element method (FEM) COMSOL Multiphysics® package.

NPs enclosed within a box segmented into 28,000 tetrahedral elements were simulated. The mesh was distributed so that the elements were approximately four times denser in the vicinity of the nanoparticles than they were at the extremities of the

bounding box. For a mesh of this density no noticeable change in the solution was seen by further increasing the mesh. The model was solved in the stationary state with periodic boundary conditions at the side walls of the box (physically equivalent to an infinite array in the x and y directions). The upper boundary was set to scattering boundary condition with an input electric field to simulate incident light. The light was allowed to escape from the bottom boundary by setting another scattering boundary condition. The FEM simulation used the bulk Ag dielectric function with a correction in the IR free electron response to take into account the reduced dimensions of the NPs [61, 68].

For an oscillating field the solution also has cyclic behaviour with the same period as the frequency of the light. This means the problem can be reduced to a time independent partial differential equation, if both the input field and the solution are given a complex phase factor of $e^{i\omega\pi}$, where ω is the angular frequency of the light. Electromagnetic wave propagation of Maxwell's equation in frequency range:

$$\nabla \times \frac{1}{\mu_r}(\nabla \times \mathbf{E}) - k_0^2\Big(\varepsilon_r - \frac{j\sigma}{\omega\varepsilon_0}\Big)\mathbf{E} = 0, \tag{1.45}$$

where $k_0 = \omega/c$ is the free space wave number, $\sigma = 0$ and μ_r is set to 1. $\varepsilon = (n - ik)^2$, where n and ik real and imaginary part of the materials refractive index. The real part is the electric field and the imaginary is cycle phase. Then the wave equation is

$$\nabla \times \nabla \times \mathbf{E} = k_0^2\mu_r\varepsilon_r\mathbf{E}. \tag{1.46}$$

For the periodic boundaries, the electric field vector is simply forced to take the same value and direction at every corresponding mesh point on opposite surfaces. The

scattering boundary conditions are

$$\mathbf{n} \times \nabla E \times -ik\mathbf{n} \times (E \times \mathbf{n}) = \mathbf{n}(\times E_0 \times (-ik(\mathbf{n} - \mathbf{k}_{dir})))e^{-i\mathbf{k}_{dir} \cdot \mathbf{r}}, \tag{1.47}$$

where E_0 is for defining incoming light. So this was used on our top surface. $\mathbf{n}$ is the unit normal to the surface, k_{dir} is direction of k and i presents imaginary. In summary the model solves these equations to a high level of tolerance but makes the space discrete(mesh). The solution is only calculated at the mesh points. In the color visualisations it may even be connected quadratically. This is relevant, as all details extracted were for the discrete form of the solution.

Chapter 2

Experimental Methods

> How wonderful that we have met with a paradox. Now we have some hope of making progress.
>
> Niels Bohr

This chapter will describe the experimental methods and equipment used throughout the remainder of this thesis. The operating principles, particular features and special advantages of the equipment used in each experiment will be shown. Also the theory of specific tools will be described.

Fabrication and analysis of the plasmonic nanostructures was accomplished following a three step procedure. The first step is preparing the stepped substrates, the second step is to grow the NPs on the stepped templates at a glancing angle and the final step is to characterize the samples by optical means.

2.1 Glancing Angle Deposition

Glancing angle deposition (GLAD) is a technique used for the fabrication of nanostructures wherein material is deposited onto a textured surface at an oblique angle [69].

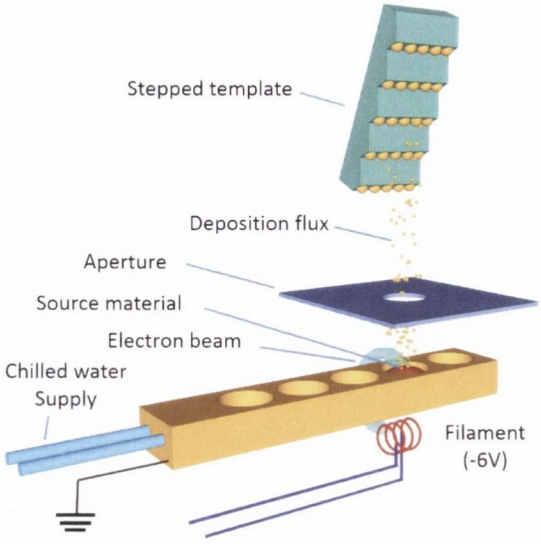

Figure 2.1: A schematic view of the GLAD technique: A flux of collimated evaporated material is directed towards the stepped template at a glancing angle of incidence, thus forming the NP arrays.

The origin of phenomenon of this technique was demonstrated in 1979 [70, 71], when the possibility of fabricating the structures below the photolithographic limit of the time was shown. The principal attraction of GLAD is its relative simplicity as it does not involve any lithographic steps. This technique is not only applicable to specific combinations of materials for the substrate and nanostructure, and material chosen for deposition can include metals, semiconductors and oxides. This technique has been developed in recent years by our research group as an alternative nano-fabrication method [36, 37, 72]. Its main purpose has been to grow planar arrays of semiconductors and magnetic nanowires, and arrays of plasmonic NPs. In this present work, glancing angle deposition is achieved by directing a collimated deposition flux towards a stepped surface at a shallow angle of incidence (typically $\leq 6°$). The step edge shadows part of the surface during the deposition and highly ordered NPs are created by self-assembly of the adatoms (see Figure 2.1).

The possibilities of producing Ag NP arrays on the stepped sapphire templates

was demonstrated in 2008 by our research group [37]. The size of NPs were tuned by changing the deposition thickness and optical response of the polarized light for longitudinal and transversal components were studied. A few years later, GLAD was systematically studied and it was demonstrated that the dimensions of the plasmonic NPs could be controlled by changing the substrate periodicity [38, 39]. Recently we have demonstrated that arrays of NPs composed of noble metals such as Au and Cu can be produced by GLAD, and that the plasmonic resonance can be tuned over the whole visible range [42].

This thesis will build on existing work in demonstrating the use of GLAD as an alternative technique for fabrication of nanostructure arrays. It will be shown that GLAD can be used for a variety of materials for the nanostructure as well as stepped templates. Furthermore, it will be shown how the morphology and dimensions of the NPs can be tuned both by heating the substrate during the growth and via a post-anneal. These advantages of GLAD will be shown in Chapter 4. The SERS application of GLAD based NP arrays will be demonstrated in Chapter 6.

2.2 The Deposition Chamber

For the growth of NP arrays two different ultra high vacuum (UHV) chambers were utilised. These chambers have the same working principles and capabilities. One of these chambers is shown in Figure 2.2A, C. The deposition chamber is made from stainless steel with 6″ diameter flanges. A turbo molecular pump (Osaka TG550, with pumping speed of 550 l/s) is connected to the chamber and a rotary vane pump is used as a backing pump. this chamber has a base pressure of approximately 10^{-8} Torr. This chamber is not equipped with a load-lock, and so must be vented pumped from atmosphere each time a new sample is to be grown. The distance between the source

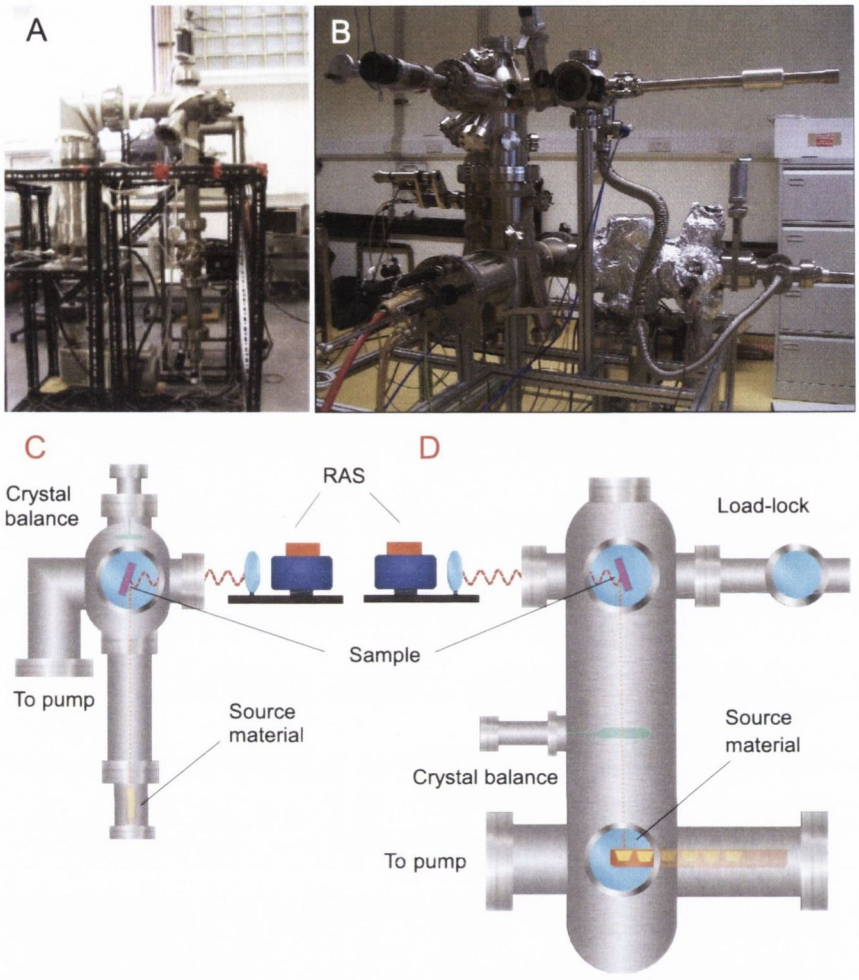

Figure 2.2: The photographs (A, B) and schematic view (C, D) of two different deposition chambers for growing the NP arrays.

and the sample is approximately 70 cm. The sample is mounted in the centre of the deposition chamber on a sample manipulator. The alignment angle is measured by the deflection of a laser spot pointing towards the sample surface. The sample stage has a resistive heater to control the temperature of the sample during deposition. The deposition material thickness is measured with a crystal balance monitor. A strain free window is placed exactly in front of the sample to allow for *in-situ* measurement of the optical properties of the sample. The main advantages of this chamber is that it

uses a k-cell which can be used to evaporate materials such as Au, which cannot be evaporated by the other system that described in the following.

A second system with a 6 pocket e-beam evaporator was also used for fabrication of NP arrays. (see Figure 2.1 and Figure 2.2B, D). This chamber is evacuated by a rotary backing pump, an ion pump and turbo-molecular pump. There is also a smaller turbo-molecular pump with a diaphragm backing pump connected to the load-lock. The chamber is divided into two regions for DC-annealing and deposition by a pneumatic gate valve. Samples are delivered from the load-lock by a magnetically coupled linear drive to the chamber. As mentioned above, this system has a 6 pocket e-beam evaporator, and is therefore useful for preparing samples which have an additional capping layer added without exposure to atmosphere. The e-beam evaporator heats the source by means of an electron beam which is produced from a system filament via thermionic emission. A large voltage (6.5 kV) and a permanent magnet guide the electron electrons towards the sample crucible. Sweep coils near the crucible specify the precise area to be heated and generate a heating pattern. The deposited material thickness was monitored with a quartz crystal microbalance. The distance between source and sample is around 40 cm. A strain free window is also attached to this system to allow monitoring the *in-situ* optical responses of samples.

2.3 Reflectance Anisotropy Spectroscopy

2.3.1 Applications and Theory

Reflection anisotropy spectroscopy (RAS) is a refection based non-destructive optical probe for surfaces and it is capable of operating in a wide range of environments [73]. In particular, it was proved by our group that RAS is a tool capable of measuring *in-situ* optical properties of the anisotropic NP arrays [38]. It probes the difference

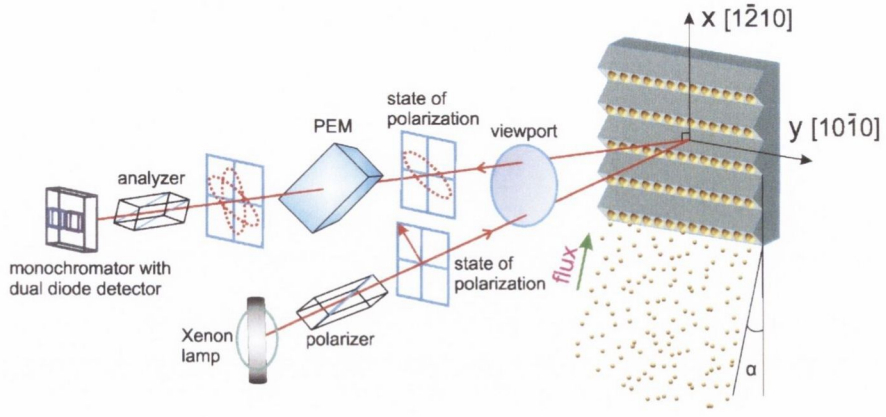

Figure 2.3: Schematic of the set-up used for the *in-situ* RAS measurements during the NP growth. The stepped surface is oriented to allow for measurements of the optical anisotropy and simultaneous deposition at a glancing angle α.

in the complex Fresnel reflection coefficients of the whole sample Δr at near normal incidence between two orthogonal directions in the surface plane (x, y), normalized to the mean value (r) [73, 74]:

$$\frac{\Delta r}{r} = \frac{2(r_x - r_y)}{r_x + r_y}. \tag{2.1}$$

As the RAS signal for an isotropic substrate is zero, the measured signal only arises from anisotropic regions in the sample. The technique measures the complete expression (2.1) directly, not the individual components (r_i), and due to the inherent self-normalisation by the total reflectance is very stable in terms of sample misalignment, background lighting and spectral shape of the light source, which makes it ideally suited for *in-situ* monitoring [73, 75]. The RAS signature of measured quantities also can be simulated by the transfer matrix formalism as was described in the Section 1.6.2

$$\frac{\Delta r}{r} = \frac{2(r_{pp} - r_{ss})}{r_{pp} + r_{ss}}. \tag{2.2}$$

The advantages of RAS compared to standard spectroscopic methods are its surface sensitivity and the possibility of measuring in a UHV environment. In this thesis

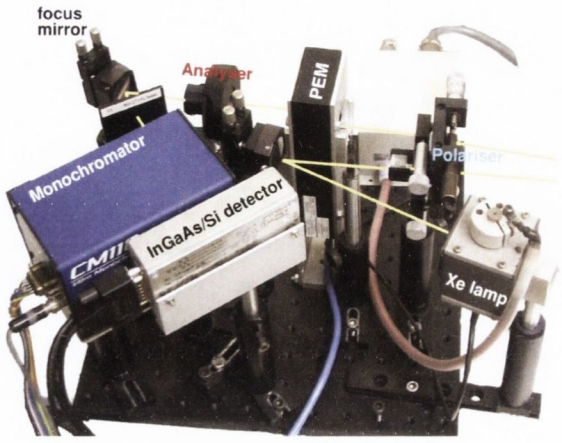

Figure 2.4: A photograph of the custom made RAS setup.

RAS was used to extract information on the growth mechanisms of the NP arrays (see Figure 2.3). As the NP optical response is measured directly in a vacuum environment no tarnishing or oxidation takes place and the exact origin of the optical resonances can be determined. The *in-situ* measurement also allows for tailoring of the NP morphology by changing the deposition parameters.

2.3.2 System Description

In this study, a custom-made RAS system was utilised for in-plane *in-situ* and *ex-situ* optical characterization (see Figure 2.4). A Xe lamp produces a bright white light that provides a broad and homogeneous spectrum in the measurement ranges. The light is sent to a Rochon polarizer and the polarized light passes through a strain free window, entering into the UHV chamber. After hitting the sample, the reflected light passes through a photoelastic modulator (PEM) and an analyser. A double grating monochromator (which allows for broad spectral range coverage) and double detector (InGaAs and Si) system are finally used. The detected signal is amplified and digitized using a DSP Lock-in Amplifier. The periodic retardation introduced by the PEM is

extracted and the RAS signal is related to the measured DC and the AC level [73]. Measurements were performed over a broad spectral range, from 0.76 eV up to 4.5 eV. An InGaAs for 0.75-1.4 eV and Si detector for 1.4-4.2 eV were utilised.

2.4 Ultraviolet-Visible Spectroscopy

Ultraviolet-visible (UV-Vis) spectroscopy is a well known widely used spectroscopic technique for measuring the transmission and absorption in the ultraviolet-visible spectral region. It measures the transmittance (T) which is the proportion of light that is transmitted by a sample (I) relative to that which would be measured if the sample was absent (I_0). Transmittance ($T = I/I_0$) is expressed as a percentage. It also measures the reflectance R which is the ratio of light intensity reflected from a sample relative to that reflected from a white tile. Reflectance also expressed as a percentage. Some UV-Vis spectrometers include additional features such as an integrating sphere which can measure all of the light scattered by a sample.

The radiation source consists of a deuterium lamp and a halogen lamp to cover the working spectral range of the spectrometer. The deuterium lamp is for operation in the UV range and the halogen lamp for near the infra-red (NIR) and visible range. There is a mirror which automatically changes the source during the monochromator slewing. The radiation from the respective source lamp is reflected from a mirror and arrives to an optical filter on the filter wheel assemble. The filter wheel is used for wavelength selection and it is operated by a stepping motor to be in synchronization with the monochromators. The filtered light is collimated via a mirror and enters the monochromator through the entrance slit to the grating, and the light is dispersed at the grating to generate a spectrum. There are two gratings, one for the detection of the light in the UV-Vis rage and the other for in the NIR range. A selected beam

from the monochromator is reflected via a toroidal mirror to the chopper assembly. The chopper consists of a mirror segment, a window segment and two dark segments. When the chopper rotates the beam alternately passes through the window segment and reflects from mirror segment. The passed beam from window segment is utilised as a reference light. The beam that is reflected from the mirror of the chopper passes through the sample and finally comes to the detector assembly. The reference beam is also passed to the detector assembly. There are two different detectors used for UV-Vis and NIR range, the beam is automatically directed to detectors via rotating mirrors. A R955 photomultiplier detector is utilised for the UV-Vis range and a lead sulfide detector is used for the NIR range. The computer digitises the detected signal from the detectors and displays the spectra of the sample. In this thesis, a Lambda 650 UV/Vis spectrophotometer was used for measuring the transmission and reflection of the samples.

2.5 Spectroscopic Ellipsometry

Spectroscopic ellipsometry (SE) is an optical surface sensitive technique used for the characterization of thin films and multi-layer structures [76]. SE can be carried out over a wide spectral range, including UV-Vis and IR. In SE, p and s polarized light is incident on a sample at an oblique angle and changes in the polarization state due to transmission or reflection are measured. It measures the two values, the amplitude ratio $\tan(\Psi)$ and phase difference Δ between p and s.

$$\rho = \tan(\Psi)e^{i\Delta} = \frac{r_p}{r_s}. \tag{2.3}$$

In the polar coordinate system the amplitude reflection coefficients and the phase difference δ can be written as

$$\tan \Psi = |r_p|/|r_s| \quad \cos \Delta = \delta_p - \delta_s. \tag{2.4}$$

An analytical approach can treat the optical response of the system for homogeneous and isotropic material, and the dielectric function of the material ε is related to ρ and oblique angle Θ by [57]

$$\varepsilon = \sin^2 \Theta_0 + \sin^2 \Theta_0 \tan^2 \Theta_0 \Big(\frac{1-\rho}{1+\rho}\Big)^2. \tag{2.5}$$

If the system comprising of multilayer or mixture of different materials, the equation 2.5 gives overall optical response of the system. The pseudo-dielectric function can be written as

$$\langle \varepsilon \rangle = \sin^2 \Theta_0 + \sin^2 \Theta_0 \tan^2 \Theta_0 \Big(\frac{1-\rho}{1+\rho}\Big)^2. \tag{2.6}$$

This equation will be fitted to experimental data in order to find the dielectric function of the system.

The operation setup of the SE is similar to the RAS system. A Xe lamp produces a bright white light that covers a large spectral range. The light passes through a polarizer and the polarizer establishes a linear polarization. The linear polarized light arrives at the sample at an incident angle and is reflected towards the PEM. The PEM modulates the polarization state of the light. After the light passes through the second polarizer (analyzer), the beam finally arrives at the detectors. Two types of detectors are applied to the system, photomultipliers for the UV-VIS spectral range and InGaAs photodiodes for NIR spectral range. The rotation of the polarizers are operated by step motors and are fully automated.

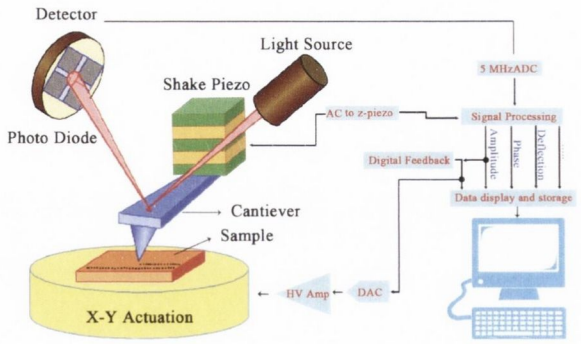

Figure 2.5: Simple schematic sketch for understanding the concept of the AFM working mechanism.

The SE measures only the relative difference between r_p and r_s, the measurements are independent from the absolute intensity. Thus, SE measurement is very sensitive and highly accurate. However, there are a few restrictions of the SE measurement. Characterization is indirect and an optical model is necessary in data analysis. When surface roughness is high, then the intensity of the reflected light may be reduced and it can be become difficult to measure the polarisation states [76].

A Woolman M-2000 ellipsometer has been used for all ellipsometry measurements to investigate the out-of-plane optical response of the samples. The beam diameter is 150 µm and the sample can be automatically rotated through 360 °. The widest spectral range is from 193 nm to 1690 nm and the measurements were performed between 245-1600 nm taking 670 points. The sample was measured with variable incidence angle with rotation accuracy ±5°.

2.6 Atomic Force Microscopy

The Atomic Force Microscope (AFM) is a tool designed to measure nanometre scale morphologies by analysing atomic forces acting between a sharp Si tip and the sample surface [77]. There are a variety of different scanning methodologies possible using an

AFM [78]. In the present work the only method used was in air AC mode (see Figure 2.5), which will presently be described.

In air AC mode a silicon cantilever is attached to a piezoelectric manipulator. An AC voltage is applied to the piezo, causing if to vibrate, which in turn causes the cantilever to oscillate at a certain frequency, behaving like a simple harmonic oscillator. The voltage is automatically adjusted so that the cantilever is oscillating at its resonant frequency. The motion of the cantilever is monitored by means of a laser beam which is directed at its reflective to face. The reflected light is measured by a grid of photodiodes which calculate the amplitude, frequency etc. of the oscillating cantilever. As the tip is lowered towards the sample surface its amplitude of oscillation decreases. The digital feedback loop adjusts the tip-sample separation to maintain a constant altitude. By rastering the tip on the sample plane the morphology of the surface is obtained.

In this thesis results were obtained with an Asylum Research MFP-3D^{TM} Atomic Force Microscope. Tap 300-G cantilevers, with a single tip fabricated from silicon were used. The radius of the tip is less than 10 nm and the Si cantilever has a nominal resonant frequency of approximately 300 kHz.

2.7 Scanning Electron Microscopy

The scanning electron microscope (SEM) uses a focused beam of high-energy electrons to generate a variety of signals at the surface of solid specimens.

A SEM usually consists of three main constituents [79]:

- Electron-optical 'column'
- Vacuum system
- Electron and display system

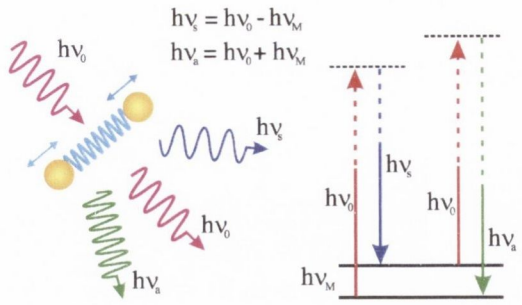

Figure 2.6: Schematic diagram of the Stokes and anti-Stokes scattering.

The electron beam is produced from an electron gun via field emission and applying a high negative voltage (typically 0.5-30 kV) which accelerates the electron beam towards the sample. The beam is then focused by magnetic condenser lenses and sent to the sample surface as a circular spot of diameter ~ 1 nm. Deflection coils finally deflect the beam in the in-plane directions and the chosen area of the specimen is scanned point by point.

Different kinds of electrons are produced by the interaction of the electron beam with the specimen. Usually, backscattered electrons are used in SEM image formation. The former have the advantage of a greater surface resolution while the latter gain whenever material recognition needs to be achieved. The electrons produced are finally collected by a detector and the chosen signals are processed by the software and an image is displayed. In this study a Zeiss ULTRA Plus field emission SEM was used for imaging all samples.

2.8 Raman Spectroscopy

Raman spectroscopy is a sensitive technique for fundamental surface studies [80]. Raman spectroscopy is based on the inelastic scattering process between a photon and a specimen. A Raman spectroscopy typically consists of four main components:

- Excitation light source (Laser).
- Sample illumination system and light collection optics.
- Wavelength selector (Filter or Spectrophotometer).
- Detector (Photodiode array, CCD or PMT).

A monochromatic light, usually produced by a laser source is focused by the optical lenses and sent towards the sample. The specimen elastically scatters most of the light. However, a small fraction of the incidence power is absorbed as phonons in a crystal or as vibrational states within a molecule and a signal at different frequency is obtained (see Figure 2.6). The scattered photon will have an energy less $h\nu_s$ than (called Stokes scattering) or greater $h\nu_a$ than (called anti-Stokes scattering) the incident photon $h\nu_0$. A wavelength selector filters out the excitation frequency and the prism (or diffraction grating) separates the rest of the light into different frequencies, detected and finally analysed via computer. Each system presents excitation peaks at particular characteristic positions, rendering Raman spectroscopy particular convenient for chemical recognition and material analysis in solid state physics. However, the main drawback of this method is the small scattering cross section, thus requiring a large active volume for any quantitative and precise measurement. In this study a WITec Alpha 300R Raman spectrometer and a Renishaw inVia Raman spectrometer were utilized for scanning.

2.9 High Temperature Furnace

The stepped substrates were prepared in a high temperature furnace (GSL 1600 X, Corporation MTI, USA). The system consists of four cylindrical SiC heating elements which generate the heating by Joule effect. A high purity alumina tube is placed at

the centre of the heating elements and it is used to load the sample. The maximum working temperature is 1550 °C with an accuracy of ±5 °C. The constant temperature zone is along a length 5 cm in the middle of the alumina tube. A B-type thermocouple is attached close to the alumina tube to measure the furnace temperature. The desired temperature is regulated by a PID controller.

Chapter 3

Substrate Preparation and Growth of the Nanoparticle Arrays

> If we knew what we were doing, it wouldn't be called research, would it?
>
> Albert Einstein

The first step in GLAD is preparation of suitable stepped templates, as the substrate plays an important role in controlling the NP dimensions and plasmonic behaviour. This chapter will introduce the faceting mechanism and the tunable features of the different substrates such as Al_2O_3, MgO and $SrTiO_3$. The production process of the Ag NP arrays on the different substrates and tuning of the morphology by changing the initial substrate periodicity will also be shown.

3.1 Substrate Preparation: Faceting Mechanism

3.1.1 c-plane Al_2O_3

In order to produce NPs arrays using the GLAD technique, ordered stepped templates are required. Following previous reports [38], single crystal c-plane Al_2O_3 (0001) templates were used during the experiments. Al_2O_3 is a good insulator and transparent between 0.45 - 6.5 eV and crystallizes in an hexagonal unit cell composed of 32 atoms [57]. Previous studies have demonstrated that a periodic arrangement of the steps and terraces can be produced upon annealing at high temperature [81–83]. Different facets of the steps align to specific crystallographic orientations such that the resulting surface morphology corresponds to the equilibrium state of the system. For these reasons c-plane Al_2O_3 was chosen as a suitable template for the development of the GLAD technique. Over the last few years, the tuning of faceting of the Al_2O_3 crystals was systematically investigated by our group, examining factors such as annealing atmosphere, time, off-cut and azimuthal orientations [84]. This was of particular interest for our purposes, as it was notably demonstrated that the surface periodicity could be tuned by changing the annealing temperature.

To produce stepped templates, single side polished c-plane α-Al_2O_3 (MTI K.J group, USA) crystals were used. The obtained substrates were off-cut along the $[1\bar{2}10]$ by 6°. The sapphire samples were then cleaned in an ultrasonic bath using solvents (methanol, acetone, high purity isopropanol) and loaded in the high temperature furnace. The samples were then annealed at temperatures between 1350 - 1550 °C for 15 hours in air and the morphology subsequently investigated using AFM. As a typical example, a sample annealed at 1400 °C is shown in Figure 3.1A, B and C. As can be seen, the surface has a highly uniform periodic step and terrace structure with a periodicity l of 100±17 nm. To achieve tuning of the template periodicity, the dependency of the

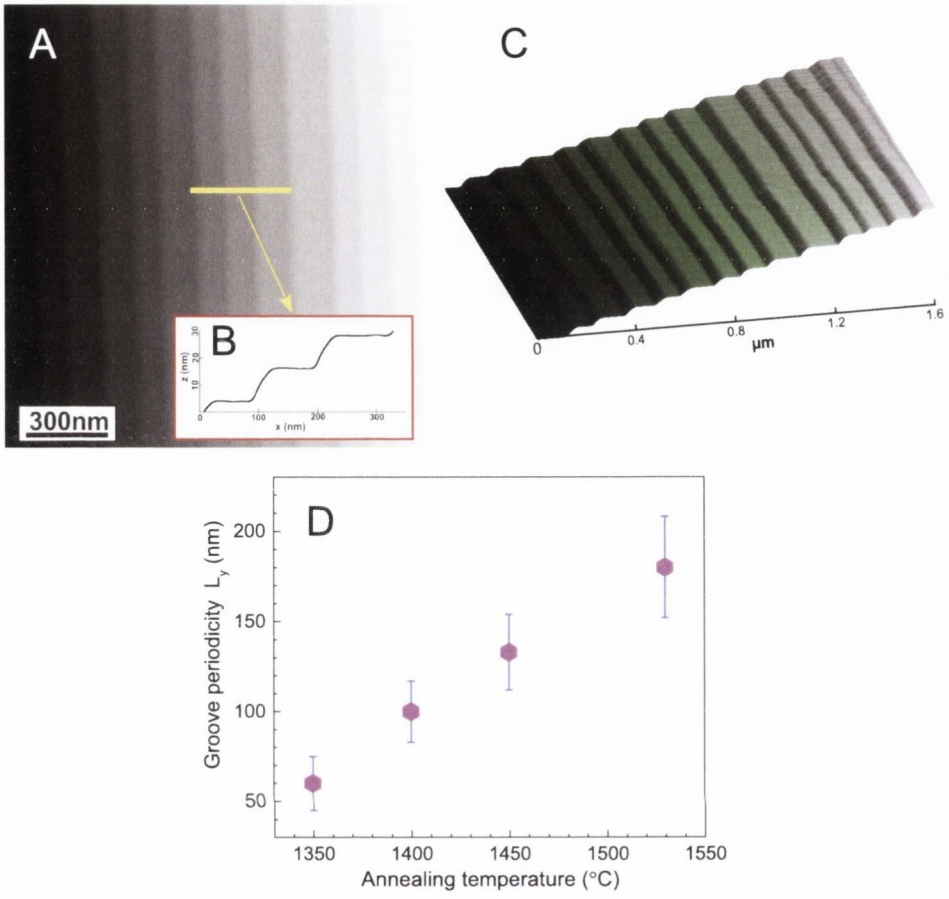

Figure 3.1: Typical 1.6×1.6 µm AFM image of c-plane sapphire with a miscut in the $[1\bar{2}10]$ direction after annealing at 1400 °C (A). (B) is height profile scan corresponding to the yellow line in A. (C) The 3D view of the faceted surface of the sample. The surface appears covered by a periodic arrangement of alternating facets. Such surfaces can be used as templates for the GLAD technique. The step periodicity dependence on the annealing temperature as a function of the annealing temperature (D).

sample periodicity as a function of the annealing temperature was also investigated (see Figure 3.1D). In agreement with previous findings [38, 81, 84], if it is seen that periodicity increases with annealing temperature. As has been outlined in previous reports [81, 83] the procedure can be considered to be a thermally activated diffusion process, wherein the periodicity of the resulting steps is assumed to be equivalent to the average adatom displacement, D. The relationship between D and temperature

(T) is giving by the Einstein relation:

$$D = D_0 \exp(-E_{ac}/k_B T), \tag{3.1}$$

where E_{ac} is the activation energy and k_B is the Boltzmann constant.

3.1.2 MgO and $SrTiO_3$

In order to produce other patterned substrates for GLAD, magnesium oxide (MgO) and strontium titanium oxide ($SrTiO_3$) crystals were also annealed. The faceting of the (110) and (111) MgO surfaces via thermal annealing was demonstrated by V. Henrich in 1976 [85]. Temperature dependent faceting of the symmetric (310) and asymmetric (100) $SrTiO_3$ was reported by Lee *et al.* [86]. More recently, the faceting behaviour of vicinal MgO (100) and $SrTiO_3$ (100) have been systematically studied by our research group and tunable step arrangements were demonstrated [87, 88].

In this thesis, the faceting processes of the MgO and $SrTiO_3$ were extensively studied for the growth of NP arrays by GLAD. To produce the stepped templates single side polished 10×10×0.5 mm MgO and $SrTiO_3$ (MTI K.J group, USA) crystals were used, off-cut along the (010) by 3 - 4°. The samples were also cleaned with methanol, acetone and high purity isopropanol. The cleaned MgO and $SrTiO_3$ crystals were individually loaded in a high temperature furnace and annealed at 1250 - 1300 °C for 3 hours. The surface of each sample was characterized with AFM. Sample AFM images are shown in Figure 3.2. The average periodicities of the MgO and $SrTiO_3$ templates are 100±26 and 120±37 nm respectively. Previous studies have shown that the facets of the steps make an angle with the (100) terrace of 10° in the case of MgO and 45° in the case of $SrTiO_3$ [87, 88].

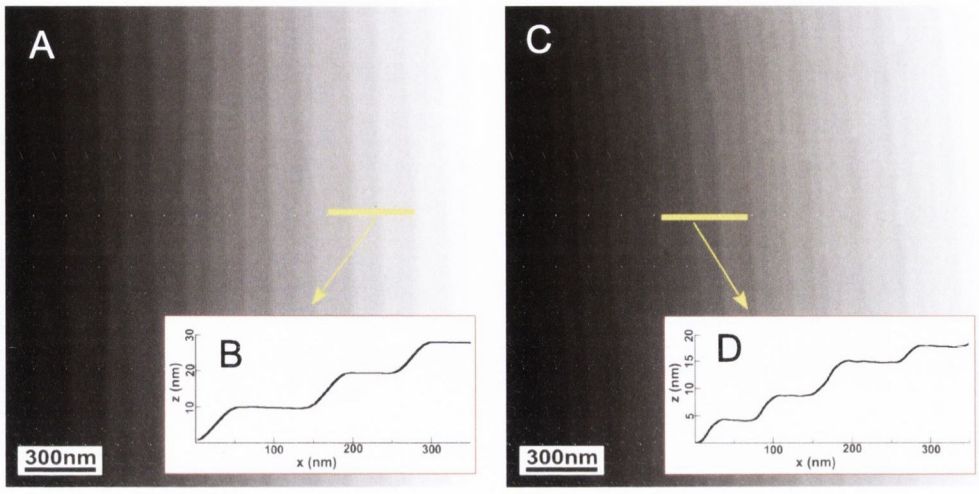

Figure 3.2: Typical 2×2 µm AFM images of MgO (A) and $SrTiO_3$ (C) substrates after annealing at 1250 °C and 1300 °C for 3 hours. B and D are height profile scans corresponding to the yellow lines in A and C.

3.2 Growth of Ag Nanoparticle Arrays

3.2.1 Experimental Procedure

After AFM was used to confirm the morphology of the stepped surfaces, the faceted samples were cut into four square or three rectangular pieces using a diamond saw. This allowed fabrication of NP arrays prepared using different growth technologies on initial substrates. Each piece was cleaned in an ultrasonic bath using acetone, methanol and high purity isopropanol. The cleaned samples were attached onto the sample manipulator and loaded into the growth chamber. The sample surface was tilted to a grazing angle $\alpha = 6°$ (see Figure 2.3) with respect to the adatom flux. This deposition angle was previously demonstrated to to produce NP arrays with the greatest possible uniformity [38]. The material was deposited at a chamber pressure of approximately 4×10^{-8} mbar and with a flux rate (Φ) at normal incidence of 2.5 nm/min. The deposition time t was kept constant at 30 minutes for all samples. Due to the inclination of the sample within the flux, the nominal thickness T of the deposited material is much lower

according to

$$T = t \times \Phi \times \sin\alpha \times \frac{l}{d_w}, \tag{3.2}$$

where d_w is the facet width. This nominal thickness is proportional to the actual amount of the deposited material. Due to the effect of shadowing and the reorganisation of the material into the NPs the actual height of the NPs will be higher. After exposure to atmosphere each sample was imaged with SEM.

3.2.2 Ag NP Grown on Different Substrates

After obtaining the stepped templates from the MgO, $SrTiO_3$ and Al_2O_3 substrates as described in Section 3.1, Ag NP arrays were grown on the substrates using the GLAD technique. In this section, we will demonstrate for the first time Ag NP arrays on MgO and $SrTiO_3$ using this technique. The average step periodicities of the templates MgO, $SrTiO_3$, Al_2O_3 were 100, 120 and 115 nm respectively. The Ag deposition for all substrates was performed at a glancing angle of 6° as described previous section. The same deposition time and growth rate were used for all samples.

The SEM images in Figure 3.3 show typical results for each substrate. As can be seen, each surface is decorated with ordered chains of NPs, confirming the suitability of these substrates for GLAD. The NPs are quite well contained within the boundaries of the step facets, and are slightly elongated along the step edge direction. The morphology of the NPs is consistent with a 3D cluster growth mechanism with a diffusion barrier between facet and terrace [39]. Due to the texturing of the template and the glancing angle of the flux, adatoms land on the step and NPs are formed as Ag does not wet the substrate. As the terraces also have the low surface free energy, the adatoms cannot overcome the diffusion barrier between step and terrace and all the material distributes on the steps only.

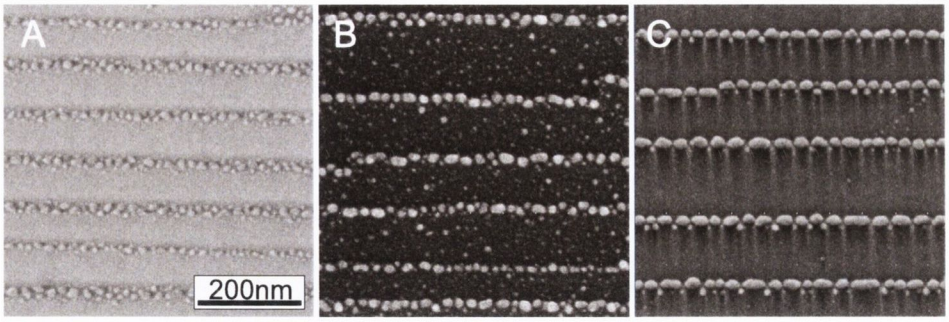

Figure 3.3: A set of SEM images of Ag NP arrays grown on the different substrates such as (A) MgO , (B) $SrTiO_3$ and (C) Al_2O_3, the deposition time and growth rate were kept for all samples. Scale bar in the same for all SEM images.

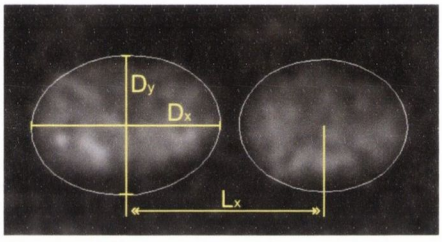

Figure 3.4: Image taken in AutoCAD® of elliptical shapes being fitted to images of NPs. D_x and D_y are the major and minor axes of the NPs while L_x is the center-to-center distance along the x-axis, which is taken parallel to the step-edges.

In order to obtain an accurate statistical analysis of the in-plane dimensions of the NP arrays AutoCAD® software was used for analysing the SEM images. Parameters measured using this software includes the major D_x and minor D_y diameters of the NPs, the center-to-center distances both along and perpendicular to the step edges (L_x and L_y respectively) and the inter-particle spacing gap d_x. This data is necessary for modelling the optical features of NP arrays. Elliptical shapes were fitted to the SEM images of the NPs in AutoCAD® and the statical information was extracted (see Figure 3.4). At least 1000 NPs were examined from each SEM image for accurate statistics and the morphological parameters are summarised in Table 3.2. The height D_z of the NPs was calculated using equation 3.2.

It was found that the most ordered and uniform Ag NPs were produced using Al_2O_3

Dimensions, nm	D_x	D_y	D_z	L_x	L_y	d_x
MgO (A)	8±6	7±5	8	10±6	100±26	2±1
$SrTiO_3$ (B)	18±7	15±6	11	22±9	120±37	4±2
Al_2O_3 (C)	21±6	18±4	12	24±7	120±23	3±2

Table 3.1: Average morphological parameters of Ag NP arrays were grown on MgO, $SrTiO_3$ and Al_2O_3 as derived from a statistical analysis of the SEM images. The plus-minus values indicate the standard deviation.

substrate. The NPs on MgO are smaller and not well-arranged in a chain compared with Al_2O_3 and $SrTiO_3$. Nice arrangements of the NP also were grown on the $SrTiO_3$, however, randomly distributed smaller NPs on the terraces can be seen. The surface free energy of the Al_2O_3 is relatively higher than one of the MgO and $SrTiO_3$ [89–91]. The higher surface free energy leads the larger diffusion length of the adatoms and increases the adatom mobility on the surface. Hence, the sizes of the particles can be larger and more ordered structures are formed on Al_2O_3. For these reasons the Al_2O_3 substrate were selected for further growth of the NP chains in this thesis.

3.2.3 The NP Morphology Dependence on Substrate Periodicity

In the previous section the most ordered Ag NP arrays were produced using the Al_2O_3 substrate. In order to investigate the dependency of Ag NP morphology on the initial substrate periodicity, three stepped Al_2O_3 templates with periodicities 60±15, 115±19 and 180±28 nm were chosen and loaded together into the deposition chamber. Ag was deposited at the same time onto all the substrates with the same deposition thickness. After growth of the NP arrays, the morphology was characterized by SEM. Typical SEM images of samples are shown in Figure 3.5. The statistical results are shown in 3.2 and from this analysis it is apparent that the NP arrays are highly ordered and are expected to be strongly coupled owning to the very small inter-particle spacing

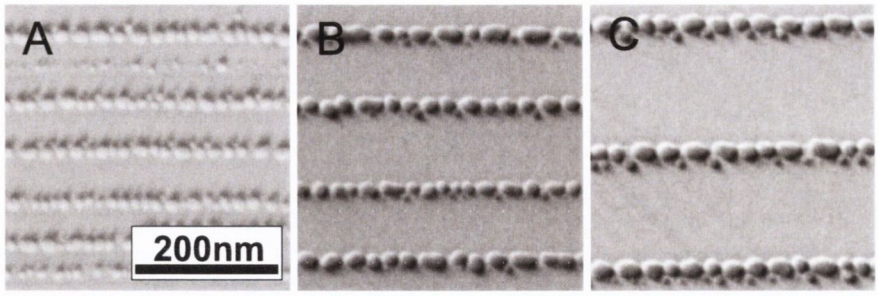

Figure 3.5: SEM images of Ag NP arrays were grown on Al_2O_3 templates with different step periodicities, are (A) 60±15, (B) 115±19 and (C) 180±28 nm, scale bar in the same for all SEM images.

Samples.	A (60 nm)	B (115 nm)	C (180,nm)
D_x (nm)	19±6	22±7	29±11
D_y (nm)	16±4	19±5	23±8
D_z (nm)	10	12	15
L_x (nm)	21±10	25±12	31±14
L_y (nm)	60±15	115±19	180±28
d_x (nm)	2±1	3±2	2±1

Table 3.2: Average morphological parameters of Ag NP arrays were grown on the differently stepped Al_2O_3.

($d_x, \approx 2$ - 3 nm). The average sizes of the NPs increase with increasing periodicity for the same deposition conditions. This tuning of the dimension of the NPs by changing the substrate periodicity has already been reported in previous studies [39]. Control over NP dimensions, as shown here is very important for the optical experiments that follow in subsequent chapters.

Conclusion

In this chapter it has been shown that ordered arrays of steps and terraces can be formed by annealing vicinal crystals of Al_2O_3, MgO and $SrTiO_3$, and furthermore that the periodicity of the steps can be tuned through appropriate choice of annealing temperature.

Growth of NP arrays using the GLAD techniques was carried out on substrates of all three materials, demonstrating their suitability for use in this process. Of the three substrates, it appeared that Al_2O_3 allowed the growth of NP chains with the best uniformity. Parameters related to the NP geometry and separations were extracted using AutoCAD® for each case.

Finally, it was shown that NP dimensions can be controlled through choice of substrate periodicity.

Chapter 4

Tuning and Characterization of Plasmonic Nanoparticle Arrays

> Science is a way of thinking much more than it is a body of knowledge.
>
> Carl Sagan

In the previous chapter it has been shown that different substrates and highly ordered arrays of tunable NPs can be fabricated. Now the optical responses of the substrates will be investigated with RAS and UV-Vis spectroscopy. The absorption and RAS spectra of the NP arrays will be measured, the results show the equivalence between RAS and absorption, and it proves that RAS can be used to measure the plasmonic resonance of the NPs. Optical responses of the Ag NP arrays grown on the different substrates such as MgO, $SrTiO_3$ and Al_2O_3 are characterized with RAS.

The possibility of tuning the NP shape by changing the substrate temperature during deposition will be shown. RAS is used to monitor the plasmonic evolution of the sample during the growth. The structures show a strong dichroic response related to NP anisotropy and dipolar coupling. Furthermore, multipolar resonances due to

sharp edge effects between NP and substrate will be investigated. Analytical and numerical methods will be applied to explain the experimental results and extract semi-quantitative information on the morphology of the NPs. The results provide insight on the growth mechanisms by glancing angle deposition. It will also be shown that the NP morphology can be manipulated by a simple illumination of the surface with an intense light source, inducing changes in the optical response. Moreover, alternative materials such as Au and Cu will be deposited onto the differently stepped Al_2O_3 substrates by GLAD. The dependence of the NP dimensions and plasmonic resonance on the substrate step periodicities will be studied. Finally, the influence of capping on Ag NP arrays will be described and the experimental results will be compared with the analytical and numerical simulations.

4.1 The Optical Properties of Substrates

Before discussing the optical properties of the NP arrays, the optical features of the substrates needs to be introduced. These play an important role in the optical characterization of the NPs and the optical response of the bare substrate should not present any distinct signal for carrying out an accurate measurement. Usually, transparent metal oxides give a constant value in the visible range in their optical response. It is possible, however, that the presence of a miscut or the annealing procedure which gives rise to faceting of the substrate may generate an anisotropic optical response. In order to rule out the possibility, UV-Vis spectroscopy and RAS measurements of bare MgO, $SrTiO_3$ and Al_2O_3 substrates after they had been subject to a high temperature annealing were carried out. The RAS spectra of the substrates are shown in Figure 4.1A. The amplitude of RAS signal is insignificantly smaller when compared to that originating from the NPs ($\sim$200 RAS units, as shall be shown in the next sections).

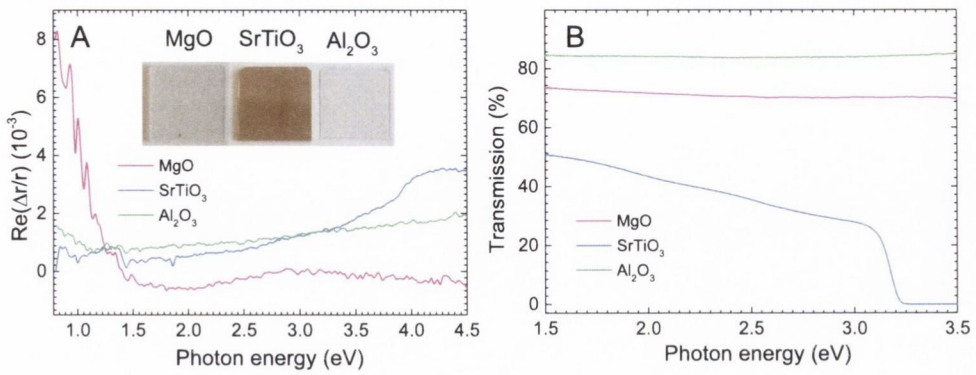

Figure 4.1: RAS spectrum (A) and transmission spectra (B) of the MgO, $SrTiO_3$ and Al_2O_3 substrates after high temperature annealing. The inset photograph in (A) shows bare MgO , $SrTiO_3$ and Al_2O_3 substrates after annealing.

The transmission spectra of substrates are shown in Figure 4.1B. The transmission percentage is approximately constant across the visible spectrum for MgO and Al_2O_3. For $SrTiO_3$, however, this value varies between 55% and 0%. This loss is largely brought about by the annealing process, after which the sample appears brown in color (see inset of Figure 4.1A).

The most ordered and uniform Ag NPs were produced using an Al_2O_3 substrate as shown in Section 3.2. As shown above, Al_2O_3 also has the greatest transparency, and has near constant transparency and RAS across the visible spectrum. For these reasons Al_2O_3 is the substrate chosen for accurate determination of the plasmonic properties of the NP arrays in all further experiments.

4.2 The Equivalence Between Absorption and RAS

In this chapter all optical responses of the NP arrays were investigated with RAS. Before discussing these measurements, the origin of the RAS response needs to be introduced. To understand this behaviour R. Verre *et al.* have shown for the first time the equivalence between RAS and polarized transmission spectroscopy for the

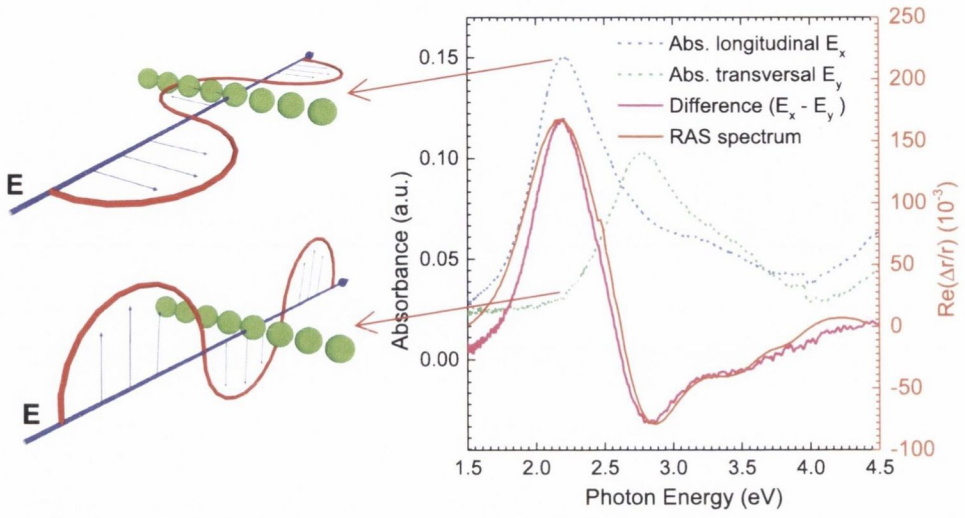

Figure 4.2: The comparison between the absorbance and RAS of Ag NP arrays grown on Al_2O_3.

Ag NP arrays investigated [38]. However, in their study only specular transmission was measured and it is not directly equivalent to the absorption of the sample due to presence of the reflection and scattering losses. In addition, single-side polished substrates were used for all experiments and their rough inverse sides cause significant loss of scattered light when the light passes through the sample.

In order to do an accurate measurement, Ag NP arrays were produced on the Al_2O_3 by GLAD technique as described previously in Section 3.2. A UV-Vis spectrometer with integrating sphere was utilized for measuring the transmission and reflection. The integrating sphere measures the diffuse transmittance and reflectance from all angles. I.e. scattering losses are avoided. Figure 4.2 shows the absorbance spectra of the sample, which were recorded with polarized light, both parallel (longitudinal component E_x) and perpendicular (transversal component E_y) to the NP chain (blue and green dashed lines, respectively). As can be seen, the absorbance profile for light polarized parallel to the chain has a peak at $\sim 2.2\,\text{eV}$, while that for light perpendicularly to the chain has a smaller peak at $\sim 2.8\,\text{eV}$. Also the intensity of the first peak is much higher

than the second one, because the plazmonic coupling along the chain is much stronger that perpendicular to the chain.

The difference $E_x - E_y$ of these two absorption peaks (light polarized parallel and perpendicular to the NP chain) is shown in Figure 4.2 (pink line). The *ex-situ* RAS spectrum is shown in same Figure 4.2 (orange line). One can clearly see that these profiles are very closely related. The positive and negative peaks of the RAS spectrum represent the plasmonic resonances along the x and y directions.

As mentioned in Section 2.3, RAS measures the difference in the complex Fresnel reflection coefficients $r_x - r_y$. The RAS spectrum of the sample can be simulated using the three layer model as described in Section 1.6.1. As shown in the previous literature [39, 57, 74], the anisotropy of the sample can be treated by two different diagonal tensor components $\varepsilon_{L,x}$ and $\varepsilon_{L,y}$, and the RAS equation 2.1 is then equal to:

$$\frac{\Delta r}{r} = \frac{4\pi i d\sqrt{\varepsilon_m}}{\lambda} \frac{\varepsilon_{L,x} - \varepsilon_{L,y}}{\varepsilon_{sub} - \varepsilon_m}, \tag{4.1}$$

where ε_{sub} and ε_m are assumed as a known value and the calculated RAS signal is only related to the response of the anisotropic layer $d(\varepsilon_{L,x} - \varepsilon_{L,y})$. In this case, d is constant, because one sample was used for both absorbance and RAS measurements. Therefore, the measured RAS signal is directly related to $E_x - E_y$.

4.3 The Plasmonic Resonance of Ag NP Arrays Grown on Different Substrates

The growth of Ag NP arrays on the MgO, $SrTiO_3$ and Al_2O_3 substrates was described in Section 3.2.2. The *ex-situ* optical responses of those three samples were characterized with RAS after growing the NP arrays. The typical results are shown in Figure 4.3.

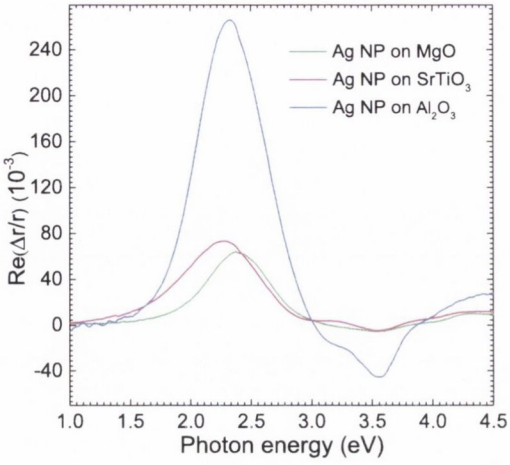

Figure 4.3: *Ex-situ* RAS spectra of Ag NP arrays grown on the MgO , $SrTiO_3$ and Al_2O_3 substrates.

The RAS spectra of these three samples appeared similar and no distinct signal arising from the substrate was observed. However, the RAS intensity of Ag arrays that were grown on MgO and $SrTiO_3$ are much lower than for those grown on Al_2O_3. As discussed in Section 3.2.2, the NPs grown on MgO showed poor uniformity and alignment. While NPs grown on $SrTiO_3$ had relatively larger major and minor axes with low standard deviation, a significant quantity of NPs were noticed on the terraces. Since these are isotropically arranged they cause a reduction in RAS intensity. The most ordered NP arrays were on Al_2O_3 without any isotropic deposition on the terrace. Therefore, the most intense RAS response was produced by this sample. For this reason, Al_2O_3 was chosen as the substrate to be used in further NP depositions.

4.4 The *In-situ* Plasmonic Resonances of Ag NPs on Al_2O_3

Ag NP arrays were grown on faceted Al_2O_3 using the procedure described in the previous Section 3.2. The morphology of the Ag NP array after deposition is shown in

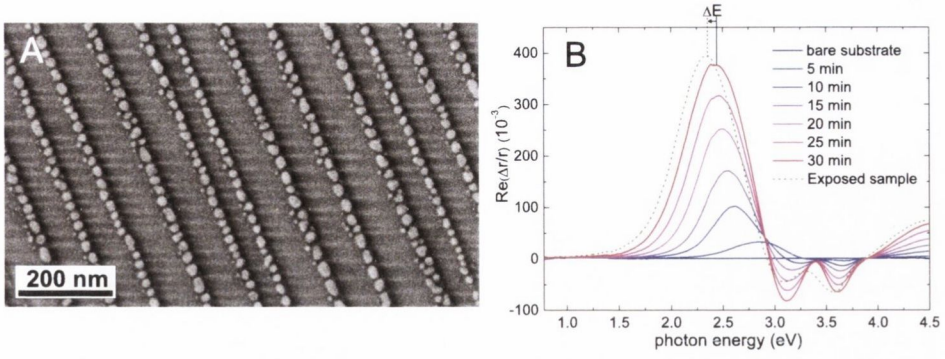

Figure 4.4: (A) SEM image of the Ag NP arrays grown on a faceted c-plane Al_2O_3 substrate at room temperature. (B) Evolution of the RAS spectra recorded during the growth. The dotted spectra were recorded after exposure of the thickest sample to air.

Figure 4.4A. The growth evolution was monitored using RAS *in-situ* and the results are shown in Figure 4.4B. The optical response of the bare substrate was to be isotropic, as expected for c-plane sapphire. Prominent features appear even after only 5 minutes of deposition. A positive peak develops around 2.5 eV and negative features are observed between 3.0 eV and 3.8 eV. The positive peak undergoes a red shift and the intensity of the peak increases with increasing deposition time. The positive peak red-shifts by an additional $\Delta E \sim 0.1$-0.2 eV and the negative features are smoothed upon exposure of the sample to atmosphere. This behaviour has been explained by the formation of a thin Ag_2O layer covering the NP upon exposure of the sample to atmosphere [39]. In particular, the strong positive peak describes the resonance along the NP array while the negative peaks arise from the in-plane resonance in the orthogonal direction. The additional negative features were assigned to quadrupolar resonances [56] due the abrupt bottom flat face of the NPs, as will be shown in the coming section. The development of the RAS signal upon deposition can hence be explained: there is an initial nucleation of small, relatively wide spaced, weakly interacting NPs. As deposition thickness is increased the NPs get bigger and more regularly spaced, leading to the larger amplitude of the RAS spectra. The gradual red-shift as growth progresses

can be attributed to the reduction of inter-particle separation as deposition continues.

As the resonance position changes with the deposition time, in principle the growth could be stopped to produce structures with resonance peaks at the required energy [42]. However, the possibility of modifying the optical properties of the structures is limited by factors such as the diffusion constant of the adatoms or the optical properties of the materials themselves. Other options for tuning the optical response include choosing alternative materials for the NPs (e.g. Cu, Au, as shown in Section 4.6) or by varying the template periodicity.

In this way the positive peak of the RAS spectrum can be positioned anywhere in the visible range [42]. However, modification of the deposition parameters also resulted in a decrease in the overall order of the structures. Consequently, broader plasmonic resonances occur, which potentially reduces the sensitivity of any optical biosensor based on refractive index changes around the NPs.

4.5 Temperature Controlled Manipulation of NP Properties

4.5.1 Dependency of the NP Morphology Upon Changes in the Substrate Temperature

Ag NP arrays were grown on an Al_2O_3 substrate with 80±15 nm periodicity using the same procedure as described in Section 3.2. Four samples were grown under identical conditions expect for substrate temperature, which was kept at 20 °C (RT), 100 °C , 200 °C and 300 °C for samples A, B, C and D respectively. The temperature was calibrated using a thermocouple with a sample surface temperature error of ±5 °C. *in-situ* RAS spectra were recorded at regular periods during the growth and *ex-situ*

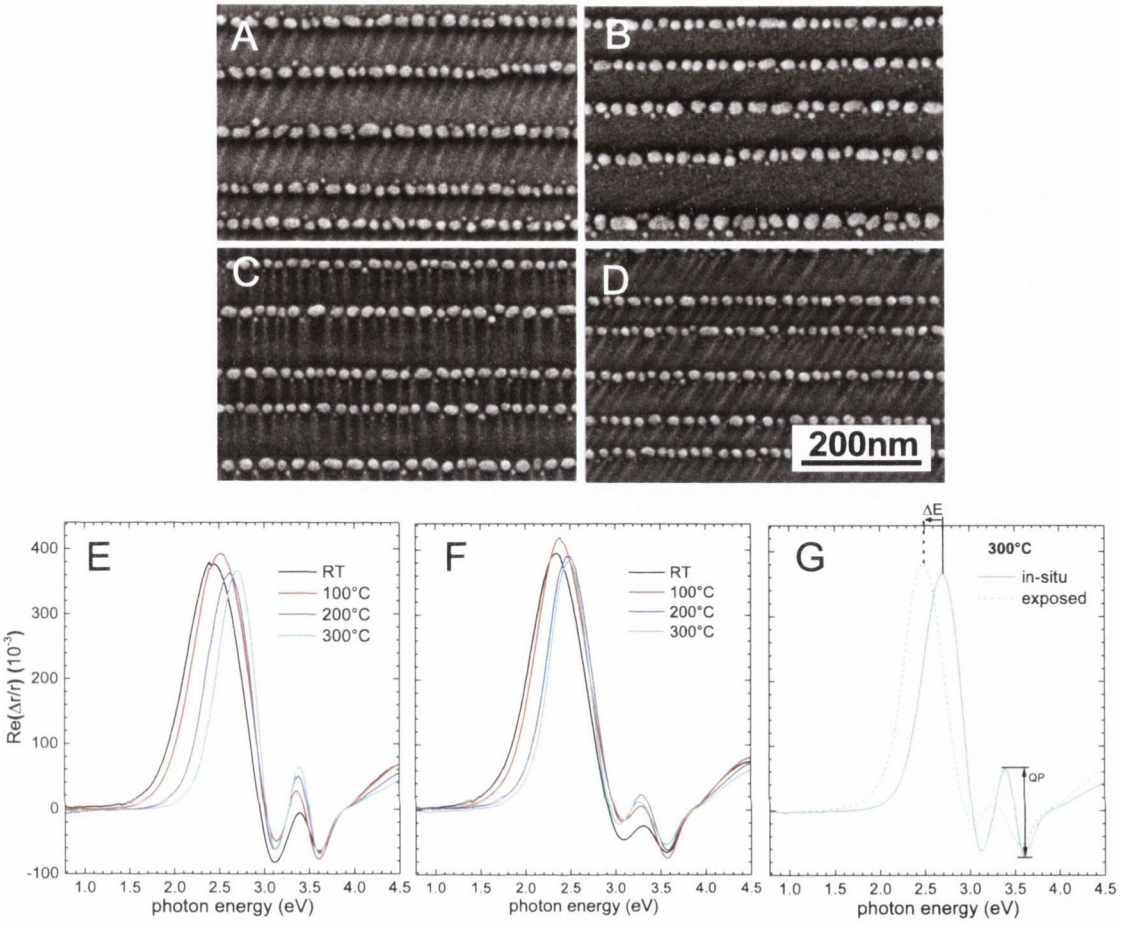

Figure 4.5: SEM images of Ag NP arrays grown at RT (A), 100 °C (B), 200 °C (C) and 300 °C (D). Deposition of Ag at higher temperature leads to more ordered and more spherical NPs. *In-situ* (E) and *ex-situ* (F) RAS spectra after the deposition of Ag NPs. (G) Compares the spectra of the sample grown at 300 °C before and after exposure. A red shift ΔE for the positive resonance is observed, together with a smoothing of the quadrupolar features (QP)

RAS spectra were recorded immediately after exposure of the sample to atmosphere.

Figure 4.5 shows the surface morphology for different substrate temperatures and the resulting RAS spectra before and after exposure of the sample to the atmosphere. SEM images have been analysed to give the sample statistics shown in Table 4.1. The in-plane centre-to-centre distance L_x slightly decreases with increasing substrate temperature. Also the average major axis of the NP along the chain is decreased while

T (°C)	20	100	200	300
D_x (nm)	25±10	25±11	21±7	20±6
D_y (nm)	21±6	21±7	19±5	18±5
Z_{NP} (nm)	9	9	10	10.5
$s = D_x/D_y$	1.21	1.19	1.13	1.09
L_x (nm)	26±11	28±13	24±10	22±10
L_y (nm)	80±15	80±15	80±15	80±15
N (μm^{-2})	490±23	450±22	520±24	550±27

Table 4.1: Average morphology of Ag NP arrays as a function of the substrate temperature. s is the aspect ratio and N is the number of particles per unit area. The nanoparticle height (Z_{NP}) values are obtained from the simulations of the optical spectra discussed in the following section.

the minor axis is almost constant, causing a decrease in the aspect ratio $s = D_x/D_y$ for increasing substrate temperature.

The changes can be explained using a simple diffusive picture. If Ag adatoms are deposited at room temperature, diffusion over the surface is limited. The seeds are formed at random positions; they grow and start merging together along the facets, resulting in elongated structures. However, if the Ag is deposited at higher temperatures, adatom diffusion is increased and more uniform arrangements are obtained. The NP axis length perpendicular to the array (D_y) is almost constant with increasing temperature due to the facet confinement, which explains the decrease in the NP aspect ratio at higher temperatures. Table 4.1 also shows that the NP size dispersion decreases at higher temperatures. The deposition time and angle were kept constant between samples, resulting in a consistent volume of deposited Ag (T = 30 min deposition). The changes in the NP height Z_{NP} (extracted from the optical model) are consistent with the expectation, as the average NP volume times the number of NPs should also be constant.

Changes in the peak positions of the RAS spectra have been also observed (see Figure 4.5). Due to a decrease in the aspect ratio s of the NP and reduced NP interaction

due to larger inter-particle separations, the positive resonance peak moves to slightly higher energies (blue shift) as substrate temperature increased. Interestingly, the plasmonic resonance peaks become sharper as the deposition temperature increases. This is expected, as the Gaussian broadening due to morphological dispersion decreases [38]. Reducing the size distribution is an important aspect, as it ensures higher sensitivity for potential applications such as a refractive index optical biosensor [92]. Finally the spectral feature at $\sim 3.4\,\mathrm{eV}$ increases in intensity and becomes positive at higher temperatures, but reduces in intensity on tarnishing by exposure to the atmosphere. As shall be shown in the coming section, these features can be attributed to quadrupolar resonances, which can be investigated by the abrupt edges of the NP base. Understanding this behaviour was one of the main motivations behind the numerical simulations outlined in the following section.

4.5.2 Theory and Discussion

The changes in the RAS spectrum discussed in the previous section will be now analysed in a semi-quantitative way and the dependence of the structure upon the various parameters involved in the simulation will be addressed. Once the anisotropic effective dielectric function is obtained, the in-plane complex reflection coefficients can be calculated using a transfer matrix formalism [65, 66] as shown Section 1.6.2 and the RAS simulated using equation 2.1.

Transfer matrix models and analytical expressions for a three layer model need a given optical thickness for the anisotropic dielectric medium. For thin films with a thickness $d \ll \lambda$, typically only the optical thickness d_ε can be analysed. In order to compare the simulated dielectric function ε of the NP layer with optical measurements, we need to define the thickness of the layer. While related to the NP height Z_{NP} this is not equivalent to it, as for an inhomogeneous system as ours, the reflectivity

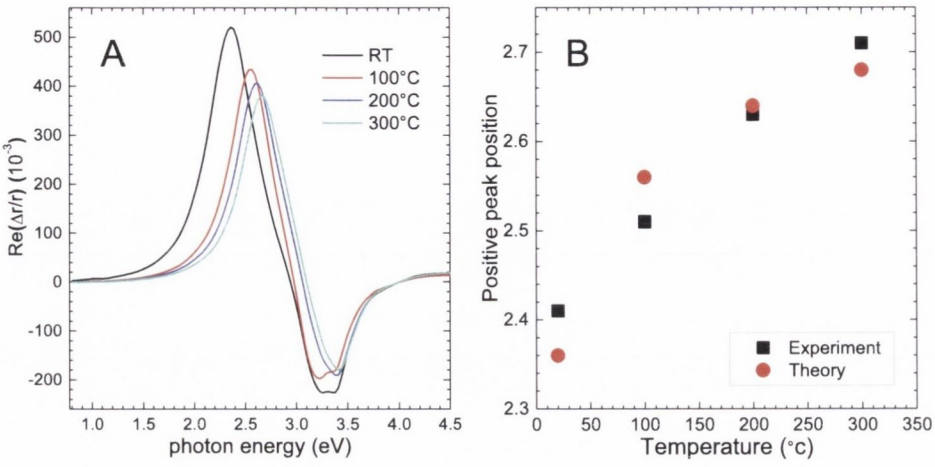

Figure 4.6: (A) Simulated RAS spectra of the Ag NP arrays calculated using an analytical model. (B) Position of the positive RAS peak for the samples grown at different substrate temperatures. Both experiment (square) and theory (circle) are indicated

of the uncovered terraces also contributes. To still be able to directly compare the measurements with the simulations, we assume that an effective thickness of the NP layer of $d = 7\,\text{nm}$ was used for all samples - in line with the nominal thickness of a smooth layer if grown under the same conditions, $t \times \Phi \times \sin\alpha = 7.4\,\text{nm}$. While this is a crude estimation, it resulted in calculated RAS amplitudes comparable to those measured.

To calculate the dielectric function of the NP layer, the measured parameters listed in Table 4.1 were used. Only one morphological parameter (the out-of-plane semi-axis, or NP height, Z_{NP}) was treated as a fitting parameter. The fitted NP height of $\approx 9\,\text{nm}$ was obtained under the constraint of a fixed overall Ag volume and is in agreement with the nominal thickness if we consider a filling factor of ≈ 0.09 as extracted from SEM analysis. The filling factor describes the area ratio between covered and total areas. Figure 4.6A shows the resulting spectra where the NP dielectric function has been scaled down by an additional 20% to take into consideration the broadening due to morphological dispersion. The simulation reproduces the shift in the positive

peak position (see Figure 4.6B) for different substrate temperatures. An analysis of the various parameters influencing the final spectral shape of the nanocomposite layer suggests that the shifts in the resonance position are related to an interplay between island anisotropy and NP dipolar coupling. More isotropic in-plane NPs and more separated NPs produce a blue shift of the original x resonance. However, as only dipolar resonances can be simulated with this analytical model, the negative peak appears as a single, sharp resonance present at higher energies than observed experimentally.

In order to investigate the origin of the additional features observed at higher energy, a FEM simulation has been performed as described in Section 1.6.3. The reflectance R_i for light polarised along a given direction $i = (x, y)$ was assumed to be proportional to the intensity of light exiting the top surface. A reflectance anisotropy $\Delta R/R = 2(R_x - R_y)/(R_x + R_y)$ can then be calculated. As the reflectance is linked to the complex Fresnel reflectivity of a sample as $R_i = |r_i|^2$ one can directly compare these simulated RAS spectra to measurements: $\Delta R/R \approx 2Re[\Delta r/r]$. However, due to small scaling differences (± 6 nm) caused by the size distribution in real samples when compared to ideal modelled structures, only normalised spectra will be compared in this work.

The analysis was simplified by assuming the NPs to be in-plane symmetric with $D_x = D_y = 22$ nm and a centre-to-centre distance of $L_x = 28$ nm and $L_y = 80$ nm. Any in-plane optical anisotropic response then arises from coupling between the NPs. The unit cell during the simulations consisted of a truncated Ag sphere resting on top of a transparent substrate with $\varepsilon_{sub} = 3.24$ (similar to the dielectric function of single crystal Al_2O_3). The choice of truncated spheres was motivated by TEM images of such NPs [39], and the fact that we did observe strong deviations from the simple dipolar model. For sharp edges, such as the edges of truncated spheres, stronger quadrupolar resonances would be expected.

The simulations were performed by truncating a silver sphere in different positions.

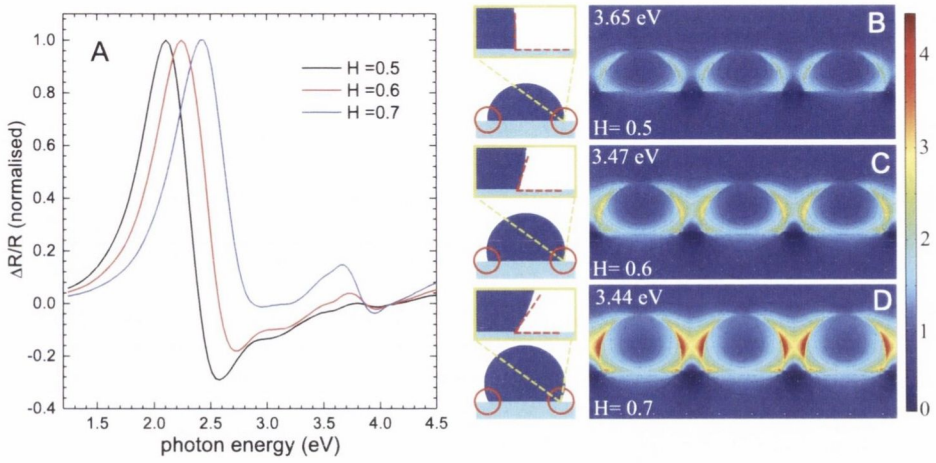

Figure 4.7: (A) Normalised RAS spectra of truncated Ag spherical NP arrays simulated using FEM for different truncation positions. For protruding extruded spheres ($H = 0.7$) a positive resonance is observable at high energy (~3.5 eV). This resonance arises from quadrupolar excitation modes from the sharp edges between NPs and the substrate. Sections of the electric field mapping along the array at the quadrupolar resonance energy for different spherical truncations are shown in B, C, and D respectively. A normalised incident electric field $E_0 = 1$ is assumed, and the same scale is used for all the images. A clear increase in the intensity of the electric field can be observed for the extruded NPs and it has been related to a decrease in the contact angle between substrate and NPs (see sketches on the left).

For convenience a parameter H was defined as the ratio between the height of the truncated sphere to its in-plane diameter. The simulations were performed with $H = 0.5$ (truncated hemisphere), 0.6 and 0.7. The normalised simulated RAS spectra are shown in Figure 4.7A. The positive feature at ~ 3.5 eV appears in the RAS spectra for extruded NPs ($H = 0.7$), similar to that in Figure 4.5E. The increase in intensity as H increases can be explained by observing a section of the electric field mapping along the array at the quadrupolar resonance energy for different spherical truncations. A much greater enhancement of the local electric field is observed for the protruded NPs, particularly where the curvature is greatest in the contact region with the substrate. The more intense field produces an increase in the resonance intensity at ~ 3.5 eV. It is also noticed that upon increasing H, the main positive peak is blue-shifted slightly.

This is similar to the behaviour seen for NP arrays grown while the substrate was heated (see Figure 4.5E). It is therefore likely that increasing substrate temperature during growth causes an increase in H and also the contact angle between the NP and the underlying surface.

As the FEM simulation deals with truncated spheres rather than ellipsoids, the assignment of the features at $\sim 3.5\,\mathrm{eV}$ in Figure 4.7A and C to quadrupolar effects appears reasonable. The statistical analysis show an increase in NP height, together with a decrease in the lateral dimensions, as the substrate temperature is increased (Table 4.1). This is consistent with the evolution of NP shape represented schematically in Figure 4.7. The decrease in intensity in this spectral region on exposure to the atmosphere (Figure 4.5G) can be explained by the reduction in curvature of the NPs on tarnishing. The FEM method suggests that the different quadrupolar intensities observed from the experiment are related to the different contact angles between the substrate and NPs. This can be controlled via the substrate temperature as the final NP morphology is governed by surface energy considerations.

The substrate/air interface of Al_2O_3 has a lower surface free energy than the substrate/Ag interface [93]. Therefore, the metal does not wet the surface and the contact area between NP and substrate tends to be minimised. This phenomenon is more pronounced at higher substrate temperatures when the adatoms have enough energy to rearrange on the substrate. This increase in the adatom mobility produces the extrusion from the surface by decreasing the contact area. Such changes in the NP morphology have already been observed for different metals on oxide surfaces [94], supporting this interpretation of the results. It is important to note that the sticking coefficient of Ag on Al_2O_3 does not vary significantly with the substrate temperature [94] and is therefore unlikely to be responsible for the large changes in the in-plane morphology of the samples observed by micrograph analysis.

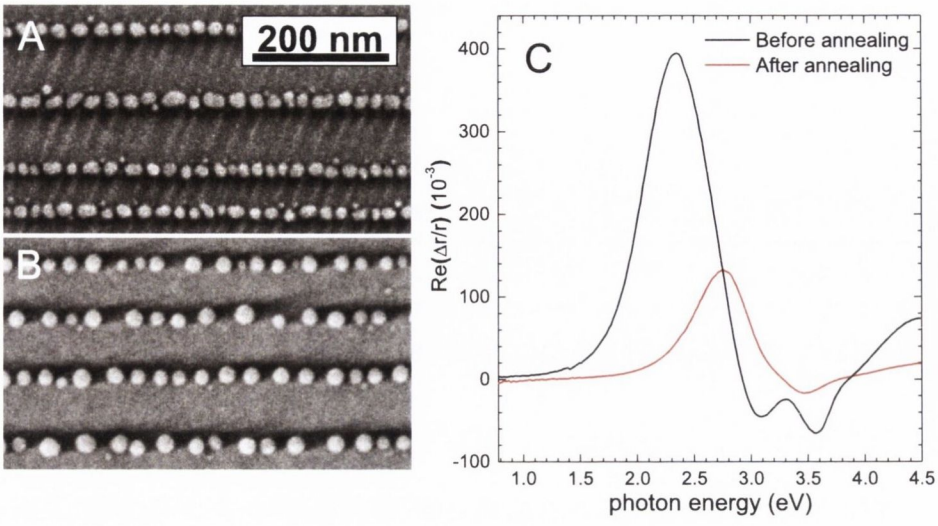

Figure 4.8: SEM images of the Ag NP arrays before (A) and after (B) annealing using a Xe lamp. Exposure of the sample to intense focused light modifies the morphology of the NP arrays. (C) RAS spectra of the Ag NP arrays before and after the annealing

4.5.3 The Manipulation of Ag NP Arrays Using Radiation Annealing

In the previous sections it was shown that the final morphology of the NPs can be tuned by varying the substrate temperature during the growth. The changes were ascribed to an increase in the adatom mobility, resulting in a different morphology of the NPs. Changing the morphology should also be possible if the adatoms can be rendered mobile after deposition. This has been achieved by illuminating the surface using intense focused light. Such phenomena were discovered almost 20 years ago [95] and are known as plasmon manipulation [96]. A sample consisting of Ag NPs arranged in an array was reported as discussed previously, and examined from the sample is shown shown in Figure 4.8A. The sample was illuminated by a Xe-lamp and Figure 4.8B shows a SEM image of the surface after annealing. From a comparison with Figure 4.8A it is evident that the NP morphology has been substantially modified. The NPs now appear

circular as viewed from above ($D = 26\pm4\,\text{nm}$) and the separation between the NPs is increased ($L_x = 33\pm8\,\text{nm}$). In our experiment the surface is illuminated by light with a homogeneous spectrum over the whole visible range. This leads to resonances in each NP and, due to the intense light source power, causes localised absorption and heating. The NPs redistribute more homogeneously on the surface. As a result, the separation between NPs increases. As the NPs are polycrystalline [39] there is no preferential growth direction and NPs assume a spherical shape. It is interesting to note that the larger changes in the morphology have been obtained using a Xe lamp and not, as previously utilised [96], a focused Gaussian laser beam. This approach allows easier up-scaling, as larger areas can be illuminated at once. As a broad band illumination source is utilised, all NPs can undergo resonant absorption at the same time, even in samples with originally inhomogeneous NP size distribution. By illuminating specific areas of the device using distinct powers, one could also produce different optical responses in the same device. Finally, the incident power of the light source in the spectral region where we expect resonant absorption (1.8-2.8 eV) is $\sim$10 W cm^{-2}. Such a value is much smaller than that previously required to produce a migration of NPs on the surface [97]. The approach developed here therefore provides significant advantages compared to previously reported methods.

RAS spectra recorded before and after plasmon manipulation are shown in Figure 4.8C. The resonance shifts towards the blue on annealing as a consequence of the more spherical shape of the NPs and an increase in the NP separation. Also, as the sample is more isotropic, the RAS amplitude decreases. Furthermore, since the annealing was done at atmospheric pressure, the NP is significantly tarnished, resulting in the complete disappearance of the quadrupolar features.

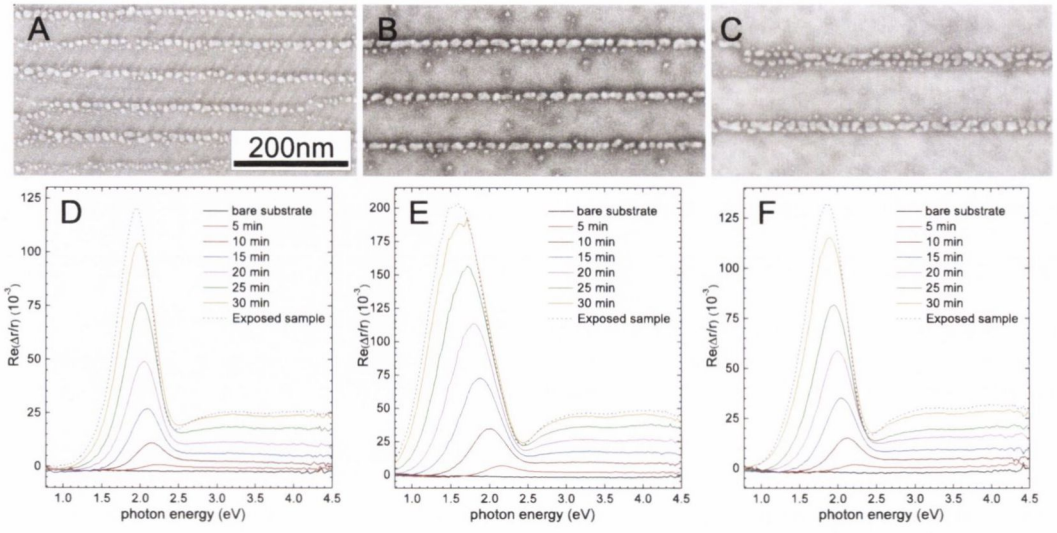

Figure 4.9: SEM images and RAS spectra of the Au NP arrays grown by GLAD deposition for 60 nm (A), 100 nm (B), 140 nm (C) template periodicity.

4.6 Au and Cu NP Arrays

So far, the study of morphology and optical properties of NP arrays has dealt solely with Ag NPs. The following section will demonstrate the broader potential of GLAD by investigating NP arrays composed of other materials namely Au and Cu. A systematic study has been performed with different stepped sapphire templates.

Three Al_2O_3 templates with step periodicities 60±15, 100±21 and 140±28 were obtained by high temperature annealing and Au and Cu NP arrays were grown on these substrates as described in Section 3.1 and 3.2. The morphology of the NPs are shown in Figure 4.9 and 4.10. Regardless of the initial template periodicity, both Cu and Au NP arrays were effectively realised. The morphological information for each of the Au and Cu NP arrays is shown in Table 4.2. The analysis show that the dimensions of Au and Cu NPs can be tuned by changing the step periodicities.

As a result, the RAS spectra of Au and Cu arrays present remarkable differences to Ag (Figure 4.9A, B, C and 4.10A, B, C). For both Au and Cu samples there is an

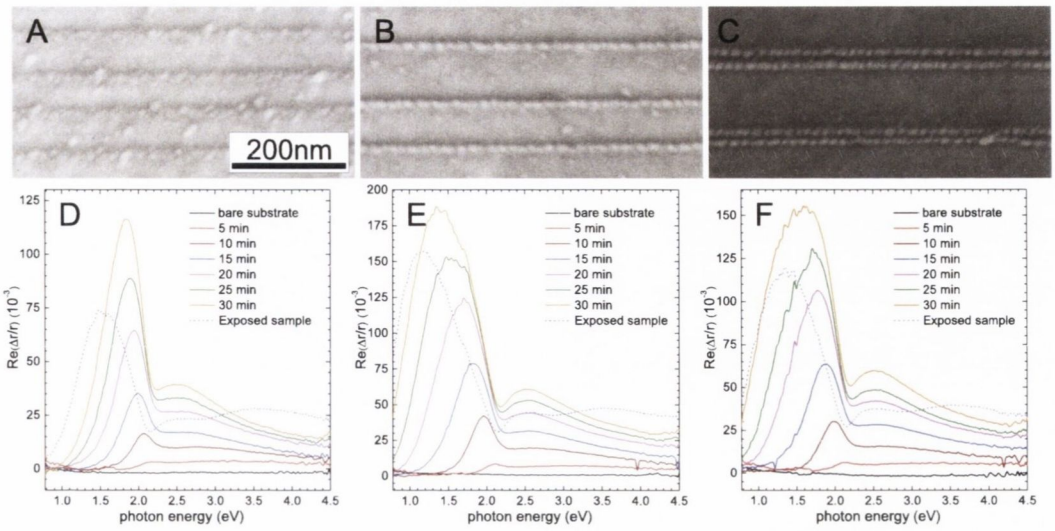

Figure 4.10: SEM images and RAS spectra of the Cu NP arrays grown by GLAD deposition for 60 nm (A), 100 nm (B), 140 nm (C) template periodicity.

Samples	Au (A)	Au (B)	Au (C)	—	Cu (A)	Cu (B)	Cu (C)
D_x (nm)	15.2±2.9	21.6±2.8	22.3±3.5		17.1±3.1	24.2±5.4	21.9±4.9
D_y (nm)	11.4±2.2	13.8±2	16.2±2.6		12.3±2.6	16.2±2.8	15.8±3.6
D_z (nm)	9	12	15		9	12	15
L_x (nm)	15.9±7	25.4±12.6	24.6±10		17.6±6.4	26.5±6.5	23.8±7.4
L_y (nm)	60±15	100±21	140±28		60±15	100±21	140±28

Table 4.2: Average morphology of Au and Cu NP arrays as a function of the substrate groove periodicity.

intense positive peak at ~1.8 eV and a broad structure at higher energy. The negative peak (y resonance) is not easy to see due to presence of the inter-band transitions for both Au and Cu at high energies [57].

In order to understand the origin of RAS signature, a sample which Au NP arrays grown on Al_2O_3 was measured by UV-Vis spectroscopy and RAS with same procedure as described in Section 4.2. The absorption and RAS comparison is shown in Figure 4.11. As expected, the difference of the two absorption peaks $E_x - E_y$ is equal to the RAS response, and the y resonance is now clearly visible in the absorption spectrum (see Figure 4.11 blue line). The main resonance of RAS spectrum has been attributed

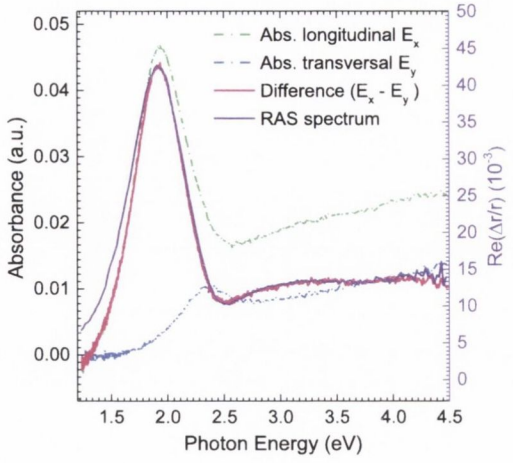

Figure 4.11: The comparison between the absorbance and RAS of Au NP arrays grown on Al_2O_3.

to the x plasmonic resonance, whose amplitude is smaller than Ag ($\sim$200 - 300 RAS units) due to the different dielectric function of this metal.

Exposure of the sample to atmosphere causes a shift in the main peak position similar to the one measured for Ag but the shifts are minimal for Au (0.06 eV for all samples) and much more pronounced (0.34 eV) for Cu. The different amplitude of the shifts confirm the high stability of Au upon exposure to atmosphere and the ease of oxidation that takes place for Cu. To get quantitative information the curves were fitted with a Gaussian fitting function, with the peak intensity and peak position of the RAS spectra plotted as a function of deposition thickness. Both positive peak intensities increase and peak position shifts to lower energy with increasing depositing thickness (see Figure 4.12).

The resonance can also be tuned by changing the initial template periodicity. This effect was previously investigated for Ag by our group [39], and it showed a red shift in the main x resonance proportional to the initial template periodicity. The same effect is observed for both Au and Cu where the period is changed from 60 nm to 100 nm. However, once larger periodicities are utilised, a blue shift and a reduction

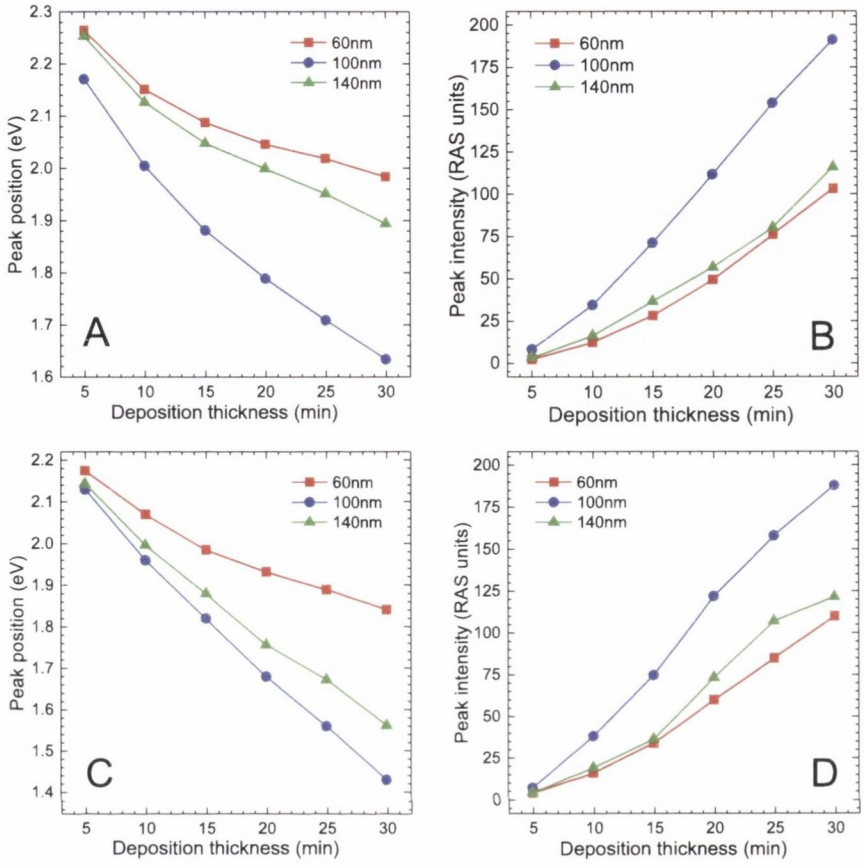

Figure 4.12: The peak intensity and peak position of Au (A, B) and Cu (C, D) NPs RAS spectra plotted as a function of deposition thickness. The intensity of each peak increases and its position shifts to lower energy with increasing thickness.

of intensity are observed. The anomalous behaviour of the 140 nm periodicity can be explained by SEM analysis. In this case, double NP chains are formed on the larger steps, as shown in Figure 4.9C and 4.10C. In this case the neighbouring NP chains are quite strongly coupled in the y-direction, as well as along the x-direction. This has the effect lowering the anisotropy and therefore reducing the RAS intensity for the resonance. The presence of such double chains is explained by a smaller adatom diffusion coefficient for Au and Cu if compared with Ag. For these materials, as the diffusion is much smaller, in the early stage of the deposition, seeds are most likely formed on a double line. As the deposition continues, the NP size increases, forming

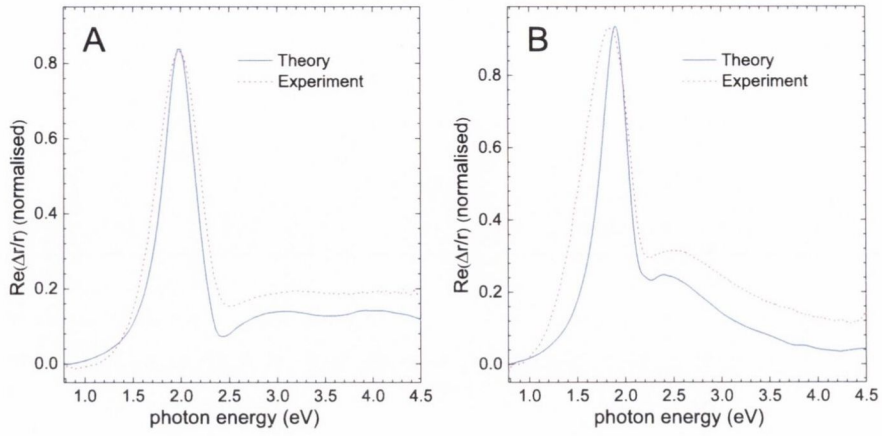

Figure 4.13: Comparison of the RAS spectra of Au (sample A from Figure 4.9) and Cu (sample A from Figure 4.10) NP arrays with the analytical model.

the double chain observed here.

The analytical model described in Section 1.6.2 was applied to simulate the measured RAS spectra of Au and Cu. The morphological parameters listed in Table 4.2 were used and the thin film dielectric functions of Au and Cu were taken from the literature for the calculations [98]. The simulated RAS spectra of Au and Cu NPs arrays grown on the Al_2O_3 sample with periodicity 60 nm are shown in Figure 4.13. The simulations show a quantitative agreement between theory and experiment.

This experimental work demonstrates that Au and Cu NP arrays can be produced by GLAD techniques and their plasmonic resonance positions appear in different energy ranges. Such dichroic plasmonic resonances can be candidates for enhanced spectroscopy [42] with a resonance energy that can be controlled by choosing the material, the initial template periodicity and the deposition thickness.

4.7 The Influence of Capping Material

In-situ optical monitoring plays an important role in the investigation of the capping influence, as the optical response can be measured without any of the tarnishing that

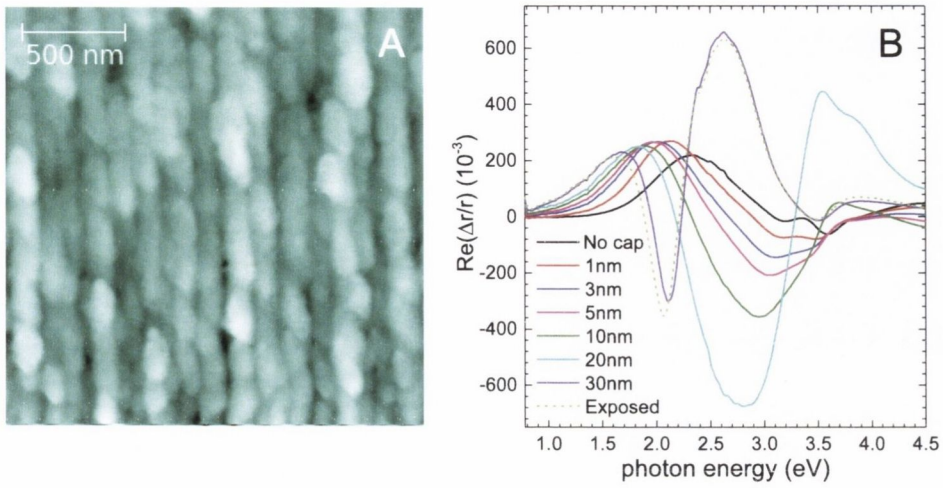

Figure 4.14: *Ex-situ* AFM image of the morphology of the Ag NPs after capping MgO (A) and the *in-situ* RAS spectra of Ag NP arrays during capping procedure (B).

takes place with *ex-situ* measurements. The MgO is a transparent material, however, since the presence of the capping layer changes the composition of the medium surrounding the NP, it will impact on their resonance behaviour and produce a shift of their resonance energy. Such a shift would depend on the thickness and refractive index of the capping layer. A number of studies have reported that refractive index based biosensors can be designed based on this principle [99–101] allowing the identification of materials through a shift in the resonance energy of underlying NPs.

In order to investigate the influence of capping material on the plasmonic resonance, an Ag NP array was grown on an Al_2O_3 substrate with periodicity of 115 nm. Once the NP growth was completed, MgO was subsequently deposited onto the Ag NP array in the same UHV chamber at an angle of 50° with respect to the sample normal. The *in-situ* optical response was recorded with RAS during the capping at intervals of 1 nm. 30 nm MgO was capped on the Ag NP arrays so that they were fully covered. The *in-situ* RAS spectra recorded during capping and *ex-situ* AFM image are shown in Figure 4.14. A $\sim$ 0.2 eV shift to lower energy and slight increase in RAS intensity

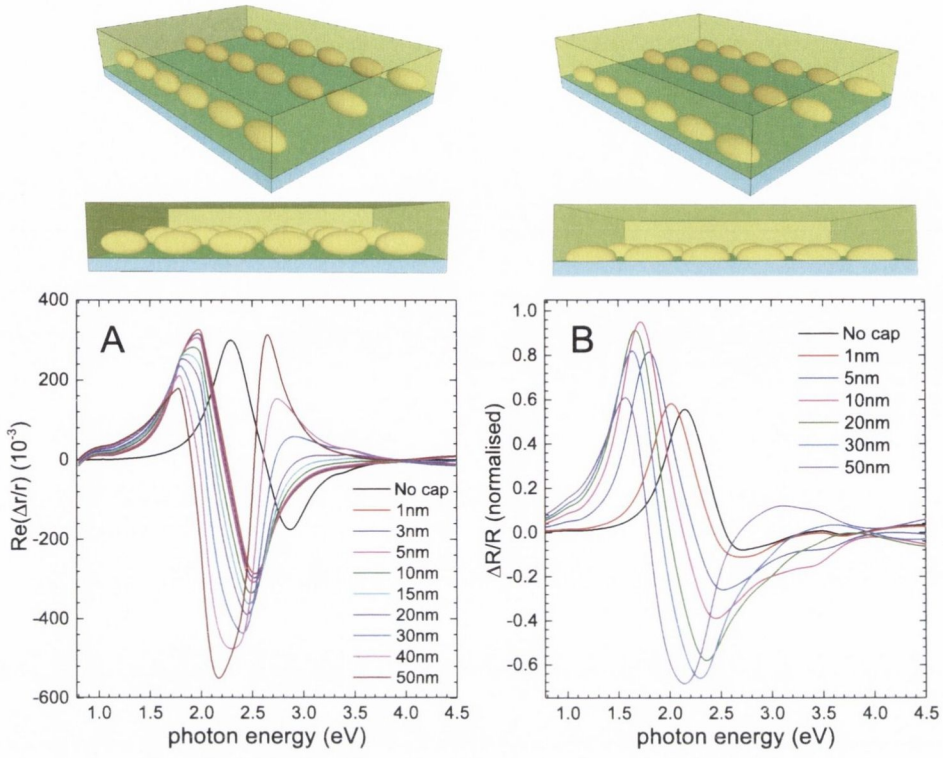

Figure 4.15: Simulated RAS spectra of Ag NP arrays under capping the MgO by an analytical (A) an a numerical (B) model. The 3D diagrams above represent the assumed geometries in each case. For the analytical model on the left the NPs are assumed to be whole ellipsoids, while for the numerical simulations on the right they are assumed to be truncated ellipsoids.

were observed for just 1 nm of MgO. As the capping layer thickness increases the resonance position shifts to lower energies and the RAS intensity gets lower. The large positive peak located at $\sim$ 2.6 eV for the 30 nm cap layer and post-exposure spectra represents a Fabry-Pérot like mode [102], but it is not the focus of the current discussion. To compare the experimental results with theory, both analytical (transfer matrix formalism) and numerical (FEM) models have been applied. In order to derive the dimensional parameters of the Ag NPs capped by MgO, Ag was deposited onto a similar Al_2O_3 substrate and left with out any capping layer. The sample was scanned using SEM and the in-plane parameters of the NPs were extracted by analysis. These

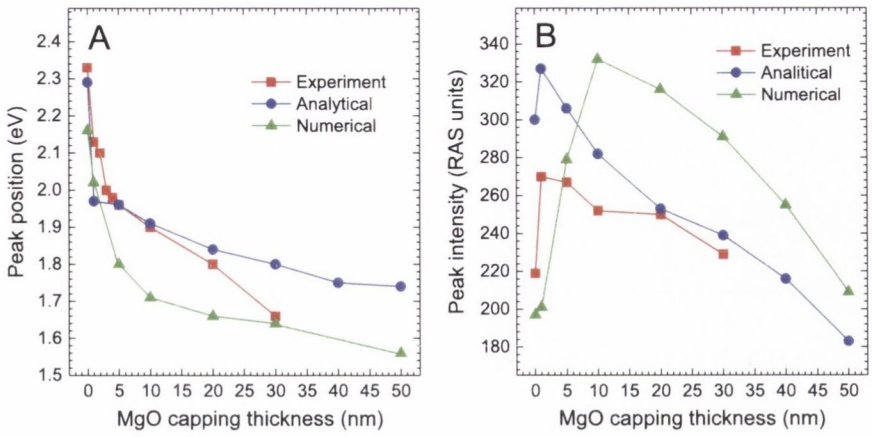

Figure 4.16: The experimental and theoretical plasmonic resonance position and intensity of Ag NP arrays were plotted as a function of capping material thickness.

parameters were then used to simulate the MgO-capped sample. The analytical and numerical simulations are shown in Figure 4.15. In the analytical model, the NPs were considered to be whole ellipsoidal (see sketches inserted in Figure 4.15) and in the numerical model they were assumed to be truncated ellipsoids. The truncated ellipsoid shape is closer to the actual form of GLAD-based NPs and in the following chapter the cross section TEM image of an Ag NP will be shown. The shifts of plasmon resonances and intensity changes are compared in Figure 4.16. In both theory and experiment, the resonance positions were red-shifted, and the intensities slightly increased once capping started and then decreased due to a reduction in the anisotropy of the system.

Conclusion

In this chapter has been shown how GLAD can produce highly ordered Ag NP arrays, and how RAS can monitor the changes in their optical behaviour *in-situ*. It was demonstrated that tunability of the dipolar plasmonic resonances can be achieved by modifying the substrate temperature during annealing. In this case modification of the NP aspect ratio is caused by an increase in adatom diffusion on the faceted tem-

plates. Also, a higher energy resonance has been observed and related to a quadrupolar resonance associated with sharp edges between the substrate and NPs, a conclusion supported by analytical and numerical modelling. These results suggest a way to engineer the NP morphology by post-annealing the sample and it is shown that this can be effectively achieved by exposing the surface to an intense broadband light source. This allows the NPs to be physically manipulated by external means over large areas. It has also been shown that is possible to fabricate Au and Cu NP arrays by the GLAD technique, and their plasmonic resonance positions appeared in different energy ranges from those of the Ag NPs. The resonance energy can then be further controlled by choosing the material, the initial template periodicity and the deposition thickness. The experimental work was compared with theoretical simulation. Finally, the capping influence on the plasmonic resonances of Ag NP arrays has been investigated and this behaviour was treated with an analytical and a numerical model.

Chapter 5

Investigation of The Out-of-plane Optical Response

> The process of scientific discovery is, in effect, a continual flight from wonder.
>
> Albert Einstein

Spectroscopic ellipsometry (SE) has been used to measure the full optical response of plasmonic structures. Firstly, the simple case of an anisotropic thin plasmonic layer supported on a transparent substrate is analysed by introducing a quantity named anisotropic surface excess function (ASEF). Such a quantity can be directly extracted from the experiment and simulated using either analytical or numerical methods. The formalism is then generalised using a transfer matrix method. In this way, effects on the ellipsometric spectra of thick plasmonic films, anisotropic substrates, and plasmonic structures grown as part of a multilayer system are described in terms of changes in the effective (pseudo) dielectric function of the system. The formalism developed is supported by experimental evidence obtained by measuring the response of anisotropic

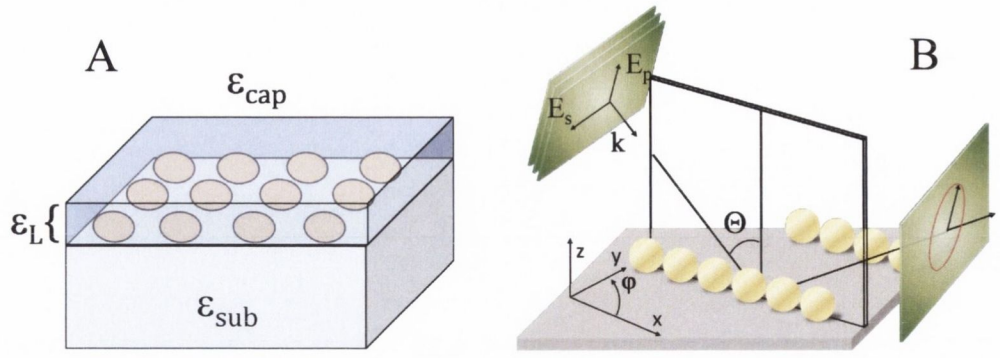

Figure 5.1: (A) Sample representation with the definitions used in this chapter. (B) Sketch for the SE measurement of Ag NP arrays in the parallel configuration. The axis and angle definitions are also indicated.

NP arrays grown at glancing angle. The agreement between theory and experiment is clear, suggesting that SE can be conveniently employed to measure the spectroscopic response of plasmonic structures. It is also demonstrated that the figure of merit of the plasmonic resonance for refractive index sensing can be greatly improved with optimized measurement configurations using polarized spectroscopy. Finally, compared to conventional transmission spectroscopies, SE can measure the out-of-plane response of the plasmonic systems, providing a more stringent test for models of the far field response of a plasmonic system.

5.1 Introduction

5.1.1 Plasmonic Studies Using Spectroscopic Ellipsometry

The optical properties of the nanostructures are usually analysed using conventional spectroscopic methods in the far field, but recently their charge distribution has been also addressed using more specific characterisation methods such as cathodoluminescence [103, 104], TEM and electron energy loss spectroscopy [105, 106]. The main

limitation of conventional absorption spectroscopies is that it allows one to monitor only in-plane properties of the plasmonic structures due to the inherent difficulties in the measurement geometry. To overcome this problem SE can be utilised as it can analyse changes in the polarization state of a linearly polarized beam reflected at oblique angles of incidence [47, 107]. The frequency value of plasmonic resonance of the NPs measured by SE is directly related to the size and surface coverage of the NPs and the constituent dielectric function [108]. Recently, SE analysis has been extended to magnetic or anistropic samples using generalised ellipsometry [109, 110]. Scattering and depolarization properties of the samples can also be addressed and separated by normal specular reflection. Also SE can be used to investigate bio-molecular interactions with metal surfaces [111] and bio-sensing measurements based on phase changes [112].

5.1.2 ASEF and Plasmonic Modelling

SE spectra are difficult to analyse as the response of the whole system needs to be modelled and compared with experiment to address the properties of the samples investigated [107]. For this reason, the number of studies of plasmonic structures using SE is still limited [46, 113–116]. Previously it was demonstrated by our research group [117] that a quantity, named Anisotropic Surface Excess Function (ASEF). The advantage of introducing the ASEF method relies on its simplicity as it depends only on the response of the plasmonic layer alone and can therefore be modeled using simple analytical or numerical methods [118, 119]. In particular, the plasmonic layer investigated here has been modelled as a collection of supported identical ellipsoids placed on a rectangular lattice, and interacting through dipolar forces. This method has been previously used to reproduce the anisotropic optical response of similar NP arrangements [39, 117]. However, the validity of this approach appears to be limited to very

specific cases (for only an ultrathin plasmonic layer <10 nm).

In general, the properties of a single layer cannot be directly extracted analytically from SE experiments. Multiple internal reflections modify the final expression of the anisotropic pseudo-dielectric function $< \varepsilon_j >$ of the system considered as an homogeneous medium along the j-th direction. Plasmonic nanostructures are even more complicated, as the layer is not homogeneous. However, if the dimension of the structures involved are much smaller than the wavelength of the exciting light, the nanocomposite layer can be treated as a continuous and homogeneous layer with an effective dielectric function ε_L which may be anisotropic. Further simplification occurs for uncapped samples using a three phase approach (substrate, plasmonic layer and air), if the nanocomposite layer is thin, the substrate response is isotropic and the optical axes are aligned with the symmetry axis of the system. In this case, the additivity between the response of each layer can be assumed to hold to the first order and the ASEF can be extracted directly from the experiment as [118–120]

$$\xi_j = \frac{i\lambda(\varepsilon_{sub} - 1)}{4\pi\varepsilon_{sub}\sqrt{\varepsilon_{sub} - \sin^2\Theta}}(< \varepsilon_j > -\varepsilon_{sub}). \tag{5.1}$$

In equation 5.1 λ, is the vacuum wavelength in nm, Θ is the angle of incidence, ε_{sub} is the substrate dielectric function and air is the surrounding medium (assumed as $\varepsilon_m = 1$).

Usually, ellipsometric observables are expressed in terms of the complex reflection ratio $\rho = r_p/r_s$ and the psuedo-(effective) dielectric function for the whole bulk system appearing in equation 5.1 can be extracted from the raw measurements using equation 2.6. If the substrate dielectric function is known, the ASEF can be extracted directly from the experiment using 5.1. The advantage of introducing the ASEF relies on its simplicity as it depends on the response of the (anisotropic) plasmonic layer alone,

which can then be modelled by [118]

$$\xi_j = d\left[\left(\Delta\varepsilon_j + \varepsilon_{sub}\Delta\frac{1}{\varepsilon_z}\right) + (\Delta\varepsilon_j - \Delta\varepsilon_k)\left(\frac{1}{\varepsilon_{sub}} - \frac{\cos^2\Theta}{\sin^2\Theta}\right)\right], \tag{5.2}$$

where $j,k = (x,y)$. The coefficients in 5.2 are defined by

$$\Delta\varepsilon_j = \varepsilon_{L,j} - \varepsilon_{sub} \qquad \Delta\frac{1}{\varepsilon_z} = \frac{1}{\varepsilon_{L,z}} - \frac{1}{\varepsilon_{sub}}, \tag{5.3}$$

and d is the effective thickness of the NP layer. The nanocomposite response can then be extracted by equation 5.1 and any suitable model capable of calculating the dielectric function of the plasmonic layer can be directly compared with the experiment using equation 5.2. The problem of analysing the response of the whole system has been reduced in this case to the determination of the plasmonic layer dielectric function.

5.2 Experiment

Ag and Au NP arrays have been produced by GLAD on the Al_2O_3 templates as described in Section 3.2. SE measurements were recorded within a few hours of the samples being exposed to atmospheres using a Woollam M2000 variable angle SE system, equipped with a rotating compensator and a high speed CCD camera. The sample was aligned at each angle of incidence and rotated manually around the surface normal. A SE measurement also carried out for for bare Al_2O_3 substrate. After measurements, Ag NP samples were capped with a 50 nm Si_3N_4 layer to facilitate TEM analysis. The deposition was performed using Plasma Enhanced chemical vapour deposition using 5% SiH_4 and NH_3 as precursors (1:6 ratio). In order to analyse the out-of-plane morphology of the Ag capped sample, TEM out-of-plane sections were prepared using a Carl Zeiss Auriga CrossBeam FIB-SEM as described in Section 2.7. Once prepared,

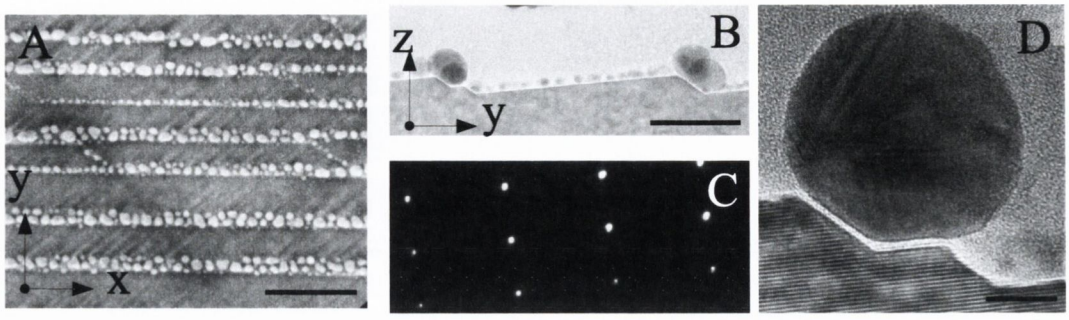

Figure 5.2: (A) Scanning electron micrograph of the Ag NP arrays deposited at a glancing angle of 6°. Cross-section TEM images with low (B) and high magnification (D) are shown together with the axes as defined in the text. Rows of NP arrays are clearly visible along the step edge of the faceted template. The TEM micrographs were measured with a $[10\bar{1}0]$ zone axis of the substrate (see diffraction pattern in C). The scale bar in (A), (B) and (D) correspond to 200 nm, 120 nm and 8 nm respectively.

the section was imaged by a Titan TEM operated at 300 kV. The substrate was aligned to the $[10\bar{1}0]$ zone axis for imaging. In all cases the images were acquired in bright-field mode.

5.3 Results and Discussion

The SEM of the in-plane structure deposited at glancing angle is shown in Figure 5.2A. The structure appears as an array of ordered NPs aligned along the step edges as previously reported. The in-plane semi-axes (average $R_x = 12\,\text{nm}$ and $R_y = 10\,\text{nm}$) are well below the optical diffraction limit and the plasmonic layer can therefore be considered as a homogeneous anisotropic layer. In order to fully characterize the sample, the out-of-plane morphology has been also analysed by TEM (see Figure 5.2B and C). This analysis shows that the NPs appear as truncated ellipsoids of height $H = 17\,\text{nm}$.

The response of the structures grown have been first analysed by SE using a fixed angle of incidence $\Theta = 61°$, and by changing the azimuth of the sample in the plane of incidence by an angle φ (see Figure 5.1). This first incidence angle was chosen as

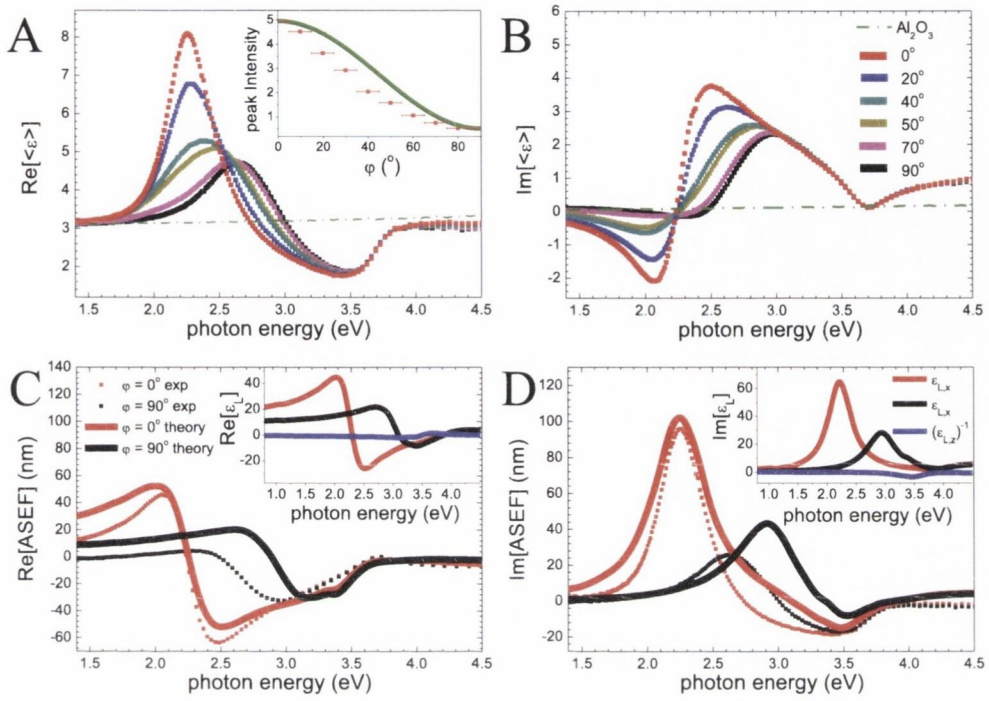

Figure 5.3: Real (A) and imaginary (B) parts of the pseudo-dielectric function $< \varepsilon >$ of Ag NP arrays grown at glancing angle for different azimuthal angle rotations φ and $\Theta = 61°$. The intensity of the x resonance at 2.2 eV follows a $\varepsilon_{L,x} \cos^2 \varphi + \varepsilon_{L,y} \sin^2 \varphi$ dependency (inset in Figure A). In C and D experimental (dotted lines) and simulated (continuous) ASEF for the parallel ($\varphi = 0°$) and perpendicular ($\varphi = 90°$) measurement configurations are shown. The insets show the modelled plasmonic layer dielectric function, ε_L.

it is close to the Brewster angle of the Al_2O_3 substrate in the visible region. In this case, as discussed in previous studies by our group on the plasmonic response of similar structures [117], the ratio between the p and s components is maximised and the response of the system can be analyzed more accurately. The measured azimuthal real and imaginary response of the structure are shown in Figure 5.3A and B respectively. Superimposed onto the featureless substrate behaviour additional features are clearly visible. The ASEF extracted from the experiment using equation 5.1 and modelled by equation 5.2 and 1.35 are shown in Figure 5.3C and D. A semi-quantitative agreement

is clearly observable using the average NP dimensions and separation obtained from SEM and TEM images. The limitation in the model is most clearly seen in the small discrepancy in the y resonance position. However, it is stressed that no fitting parameter has been introduced in the simulation and that the simulated spectra are obtained using only morphological parameters measured by micrographic analysis.

From Figure 5.3A, for the measurement configuration parallel to the array ($\varphi = 0°$), a positive peak can be observed at $\sim 2.2\,\mathrm{eV}$, together with a minima present at higher energies. As previously discussed and suggested by the theory (see, e.g., the dielectric function of the layer in the inset of Figure 5.3C, D) the positive feature in the imaginary part of the ASEF is related to resonances along the x direction [117], while the minimum at higher energy correspond to the z resonance. The opposite sign in the out-of-plane z resonance is due to the discontinuity of the perpendicular component of the electric field in Maxwell Boundary conditions [121]. By rotating the sample towards the measurement configuration perpendicular to the array ($\varphi = 90°$) the intensity of the 2.2 eV decreases monotonically. The behaviour can be explained by rotating the sample symmetry axis away from the optical axis. In this case the rotation of the layer dielectric tensor in equation 1.35 can be expressed by the matrix

$$A(\varphi) = \begin{pmatrix} \cos\varphi & -\sin\varphi & 0 \\ \sin\varphi & \cos\varphi & 0 \\ 0 & 0 & 1 \end{pmatrix}. \tag{5.4}$$

Defining now A^T as the transpose of A and remembering that the dielectric tensor of the plasmonic layer upon in-plane rotation can be expressed as $A^T \varepsilon_L A$, the 2.2 eV peak height is given by $\varepsilon_{L,x} \cos^2\varphi + \varepsilon_{L,y} \sin^2\varphi$. The inset in Figure 5.3A reproduces the trend of the axis rotation expression.

Figure 5.3 also shows that, for thin plasmonic films and transparent substrates,

the absorptive component of the plasmonic layer is present in the real part of the pseudo-dielectric function. This reversal between Re[$< \varepsilon >$] and Im[ε_L] arises from the imaginary term i present in equation 5.1. While the validity of the ASEF approach is constrained to ultrathin plasmonic layers and isotropic bulk responses [118], for such systems a direct comparison between theory and experiment can be achieved by assessing the response of the anisotropic thin plasmonic layer along the sample anisotropic main axes (φ=0° and 90°) at the substrate Brewster angle. This minimises the mixing between p and s components of the reflection coefficients (hence mixing of the response of both x and y resonances), and the resonances can be immediately attributed to the in-plane and out-of-plane resonances along the symmetry directions of the system. Clearly, the measurement for isotropic samples is further simplified as the dependency on the azimuthal rotation angle is removed.

5.4 Extension to A More General Formalism

In the previous section it was shown that the ASEF approach can be successfully applied to the analysis of ultrathin plasmonic layers. It was also shown that the simulation reproduced the results even when the optical axes were not aligned with the principal axes of the system, provided a rotation of the dielectric tensor was performed. However, the ASEF approach becomes inaccurate when multilayer structures or thick plasmonic layers are considered.

In this section we will show that the transfer matrix formalism introduced in Section 1.6.2 can also monitor the ellipsometric complex ratio ρ. The complex reflection coefficients were readily calculated and ρ was obtained as r_p/r_s. This ratio $\rho = r_p/r_s$ is used in equation 2.6 to obtain the pseudo-dielectric function to be compared with experiment. The only input parameters required for the application of this method

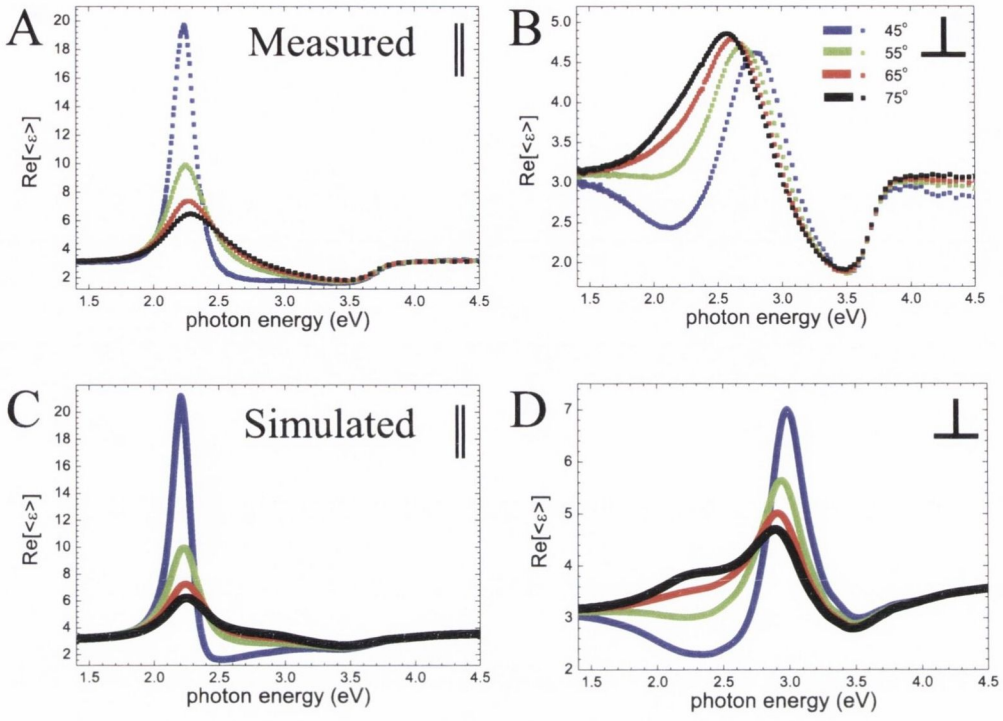

Figure 5.4: Real part of the pseudo-dielectric function for the measurement configuration parallel $\parallel$, $\varphi = 0°$ (A) and perpendicular $\perp$, $\varphi = 90°$(B) to the array, for different angles of incidence Θ. The simulated pseudo-dielectric functions for the two cases calculated using the transfer matrix formalism are shown in (C) and (D) respectively.

are the dielectric function of each layer and the respective thickness. Any method which allows one to model the dielectric function of the plasmonic layer can then be compared directly with the response measured by SE. In the following the effect of different factors on the spectra as measured by SE will be discussed.

The validity of the approach is first tested, on the same sample, for parallel and perpendicular configurations by comparing the simulations with spectra measured at different angles of incidence. The resonances appear in the real part of the pseudo-dielectric functions, which are compared for the configurations parallel and perpendicular to the arrays in Figure 5.4. Good agreement between experiment and theory was found for both the real and imaginary component. It is clear that the pseudo-dielectric

function of the whole system depends heavily on the angle of incidence. As the sample is anisotropic, the reflection is different along the two orthogonal in-plane directions. Varying the angle of incidence alters the contribution of the p and s components, resulting in a strong change in the reflection ratio and hence in the pseudo-dielectric function. For the perpendicular configuration (5.4B and D), the y resonance peak shift is correctly reproduced for various angle of incidence, but the changes in intensity are not. The disagreement is due to a shift between the simulated y resonance and the measured one, mentioned previously.

Of particular interest is the fact that, for the $\varphi = 0°$ measurement configuration (Figure 5.4A) the intensity of the positive peak at 2.2 eV increases by a factor of ~ 3 when going from $\Theta = 61°$ to $\Theta = 45°$ and at the same time the resonance sharpens. These effects are well reproduced by the simulation.

In the case of anisotropic samples, the possibility of measuring such sharp resonances could be of great interest, as the figure of merit (FOM) of the sharp resonance structure is greatly increased. Usually, FOM describes the resonance shift upon changes of the refractive index of the dielectric medium covering the particle. For this system, $\Theta = 45°$ produces an increase of the FOM by a factor of ~ 15 compared with $\Theta = 70°$. The simulations suggest that the FOM for this system can be even further increased at a measurement angle of $\sim 35°$, a possibility that instrumental limitations did not allow us to explore. These results suggest that the sensitivity of refractive index plasmon-based biosensors can be increased significantly by choosing an appropriate angle of incidence and measuring polarized reflectance ratios.

As a representative example, in Figure 5.5 a comparison is shown between the simulated absorption and SE spectra when the NP arrays are surrounded by different dielectric media. The absorption profiles were obtained using the relation $A_{\mathrm{abs},x} \propto \mathrm{Im}[\varepsilon_{L,x}]/\lambda$ [55]. As expected, an increase in the refractive index surrounding the NPs

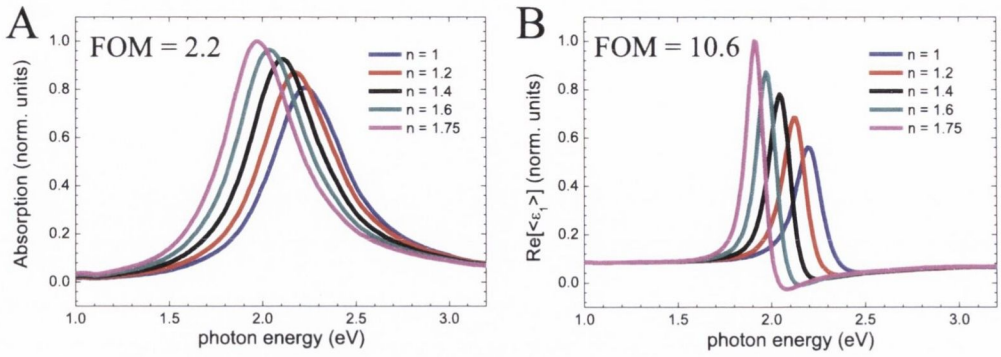

Figure 5.5: Simulation of the absorption along the NP arrays (A) and of the pseudo-dielectric function (B) in the parallel configuration at $\Theta = 45°$ upon changes of the dielectric medium covering the particles. Red shifts in the x resonance are observed with increasing refractive index. The simulated FOM is significantly increased using SE when compared with conventional absorption spectroscopy.

red shifts the x resonances. However, a much sharper profile is obtained for the pseudo-dielectric function, leading to a FWHM approximately 5 times smaller than that for the simulated absorption spectra. Similar enhancements have been recently reported for in-plane symmetric systems when measuring the phase difference between the p and s polarized components as a function of the incidence angle [116]. It is clear that measuring relative changes in p and s polarized reflection, using an optimised measurement configuration, offers the possibility of significant improvement in the FOM of plasmonic sensors. Phase sensitive measurements appear then as a sensitive route which can lead to single molecule recognition, as recently discussed [112].

To understand the origin of the observed changes in the pseudo-dielectric function intensity, the simulated $\tan\Psi$ and Δ have been plotted in Figure 5.6 for two angles of incidence ($\Theta = 65°$ and $\Theta = 45°$). It can be noticed that at resonance a 180° phase difference between r_p and r_s occurs for both angles of incidence. However, at a shallower angle of incidence, the complex ratio amplitude $\tan\Psi$ reaches larger values as the intensity of the p- and s-polarized reflection is comparable. In this way, the

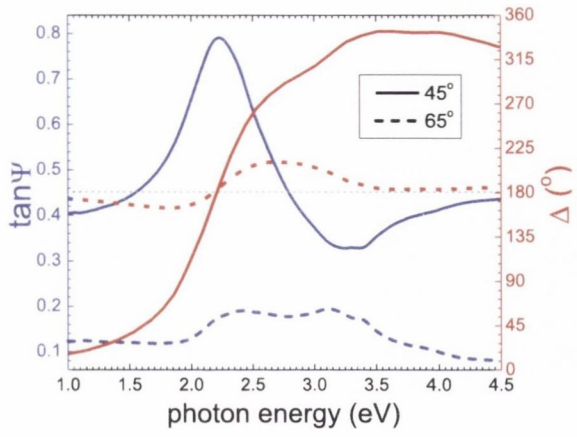

Figure 5.6: Simulation of the ellipsometric angles at $\Theta = 65°$ and $\Theta = 45°$. At the 2.2 eV resonance a $\Delta = 180°$ phase shift occurs upon reflection. At the same time, for the 45° incidence angle, the amplitude ratio $\tan\Psi$ reaches values close to one, hence explaining the increase in the intensity of the resonance observed in Figure 5.4.

denominator in equation 2.6 approaches zero and a singularity appears for the overall system response. Sharper and more intense resonances can be measured whenever the intensity of the reflection coefficients are comparable and at the same time a phase retardation of π takes place. This is a general condition which can be verified for different anisotropic systems.

The transfer formalism can also be adapted to other optical characterization methods, such as RAS [122] and different materials. The theory could be extended to magnetically active systems [66] and core-shell plasmonic structures[123], and a complete analysis on the behaviour of each reflection coefficient becomes possible. This more general approach appears to be a more suitable and convenient method to simulate and analyse the spectroscopic response of plasmonic structures, even included within multilayer structures.

In the following, the effect of increasing the NP layer thickness is finally addressed, while the NP size and distribution on the substrate remains fixed. As previously pointed out, simulations using the transfer matrix method require a given optical thick-

ness for each layer composing the stack. For the inhomogeneous plasmonic layer as the one here investigated, its effective thickness is not equivalent to the NP height. During previous simulations, a thickness of 1.5 nm was considered, in line with the nominal deposited Ag thickness for the system of 1.3 nm. While this is a crude estimation it resulted in amplitudes comparable to those measured in the experiment.

Figure 5.7 shows the simulated SE spectra for increasing layer thickness d. To simplify the analysis, the plasmonic layer was assumed to be in-plane isotropic ($R_x = R_y = 20\,\text{nm}$ and $R_z = 7.5\,\text{nm}$), and with Ag particle spacing large enough to disregard any inter-particle coupling ($N = 7 \times 10^{13}\,\text{NP/m}^2$). The self-image charge contribution is still taken into account. With these parameters, the dielectric function of the layer is shown in Figure 5.7A. As the sample is in-plane isotropic, $< \varepsilon >$ is now independent of the azimuthal rotation angle φ. Figure 5.7B and C show that changes in the plasmonic film thickness result in a strong modification of the SE response.

In particular, it can be noticed that for ultrathin structures, the plasmonic resonances appear in $\text{Re}[< \varepsilon >]$ and its imaginary part assumes unphysical negative values. These changes are related to the presence of the plasmonic layer, which heavily modifies the polarization properties of the reflected beam as also shown in the experiment in Figure 5.3. These phenomena are characteristic for ultrathin layers, as it can be shown that $\text{Re}[< \varepsilon >] \propto \text{Im}[\varepsilon_L]$. In particular, this proportionality relation is valid whenever the plasmonic film is thin, i.e., [117]

$$d \ll \frac{\lambda}{4\pi\sqrt{\varepsilon_{L,j} - \sin^2\theta}}. \tag{5.5}$$

Figure 5.7 now allows a more precise quantification of equation 5.5: Even for an effective plasmonic layer of 5 nm a mixture between the layer and effective dielectric functions takes place and the simple proportionality is no longer valid. It would be

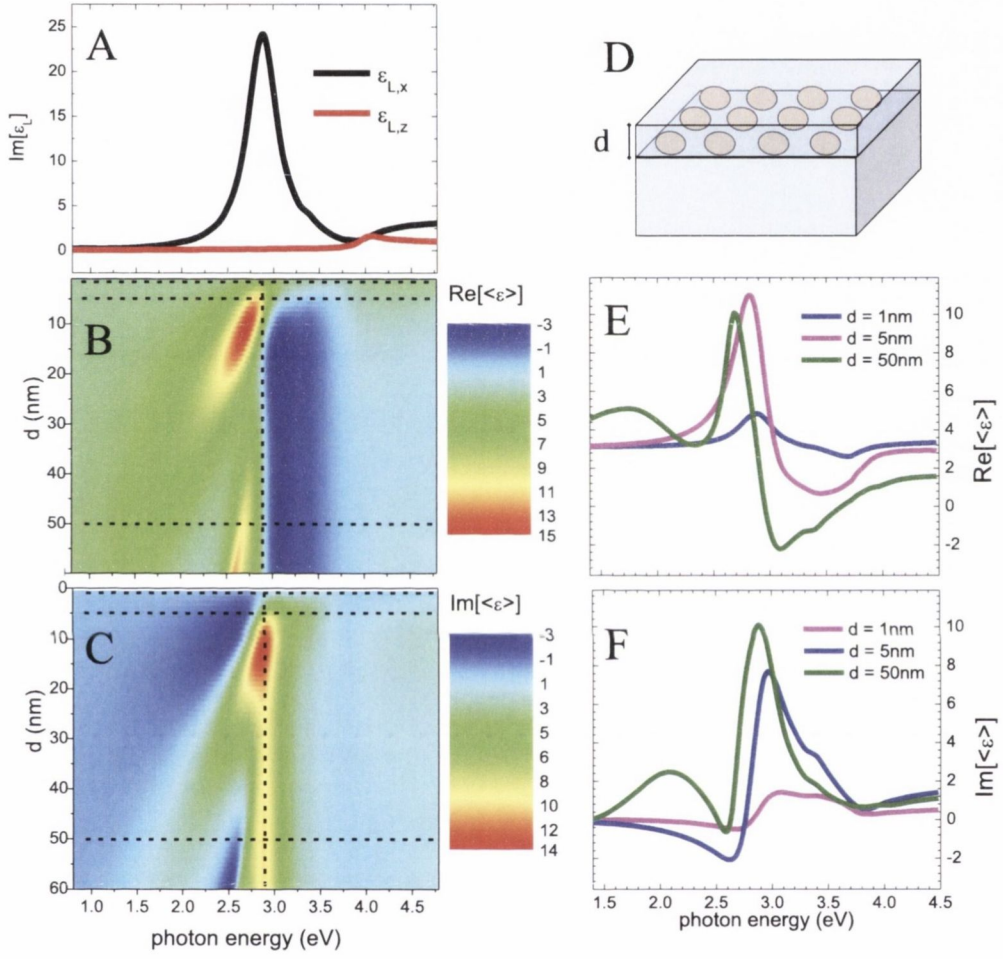

Figure 5.7: (A) Simulated imaginary part of the dielectric function of supported isotropic spheroids along the x and z direction. The contour plot of the real and imaginary part of the calculated psuedo-dielectric function for different plasmonic layer thickness d (see sketch in D) are shown in B and C respectively. The vertical dotted line shows the position of the x resonance and it is used as a guideline. For clarity, in E and F the real and imaginary part of the dielectric function for different thicknesses d are also shown. These are effectively cross sections of the contour plots in B and C taken at the locations of the dotted lines.

then of great interest to understand how the NP height affects the effective plasmonic layer thickness. This possibility cannot be easily investigated using the glancing angle deposition method described here as the NP produced are usually smaller than 20 nm. However, it appears that large layer thickness results in an even more complex behaviour that is difficult to relate directly to the plasmonic features, but can be addressed easily using the transfer matrix approach.

During the simulation throughout the text, the anisotropy of the substrate has been disregarded. Even though Al_2O_3 is a well known birefringent material, no change were observed in the simulations by using its ordinary or extraordinary refractive index. For simplicity, the ordinary refractive index has been used. The transfer matrix approach has been formulated in a fully anisotropic picture [65, 66], and hence our limitation to an anisotropic simulation is just a simplification for convenience.

The SE response from by plasmonic structures depends on many contributing factors, such as NP morphologies, material composition, and substrate dielectric function. The overall response can be heavily modified by changes in any of them. In particular, it has to be noted that the discussion of the FOM by directly using the pseudo-dielectric function is another simplification allowed by the use of a transparent substrate. Once non-transparent substrates are used the dielectric properties of the NP layers have to be extracted by optical models, as it is standard practice in ellipsometric analysis. Using the general approach described here, the unknown parameters can be treated as fitting parameters and the modelling refined using the standard ellipsometric approach to multilayer structures. In this case, clearly, analytical models for the NP dielectric function, as used here, are much more suited for fast convergence.

The SE response originated by plasmonic structures depends on many contributing factors, such as NP morphologies, material composition and substrate dielectric function, and the overall response can be heavily modified by changes in any of them.

Using the general approach described here, the unknown parameters can be treated as fitting parameters and the modelling refined using the standard ellipsometric approach to multilayer structures [107]. In this case, clearly, analytical simulations such as the one introduced here are much more suited for fast convergence.

5.5 Extensive Investigation: Au NP Arrays

The transfer matrix approach developed in this thesis can be used to simulate the optical response measured with other spectroscopic techniques and can be utilised with different materials. As GLAD is independent on the deposited material as was shown in previous chapter, Au NP arrays can also be produced and their response measured using SE (see Figure 5.8A for a SEM image of the surface after deposition). The real part of the pseudo-dielectric function as measured by SE in the configuration parallel and perpendicular to the array are shown in Figure 5.8B and C for multiple incidence angles. The optical response shows clear differences when compared with Ag NPs. The main x resonance is placed further in the near IR (1.66 eV) and higher energy features measured for the Ag case are screened now by strong and broad features related to interband transitions [42]. This was also simulated using the transfer matrix approach. The Au dielectric function was taken from literature [98], and the free electron response corrected in order to take into consideration the reduced dimensions of the NPs [39, 68]. In order to simplify the discussion, the same morphological parameters as those used for Ag NPs are used during this simulations. These results support the validity of the methodology applied for different NP materials.

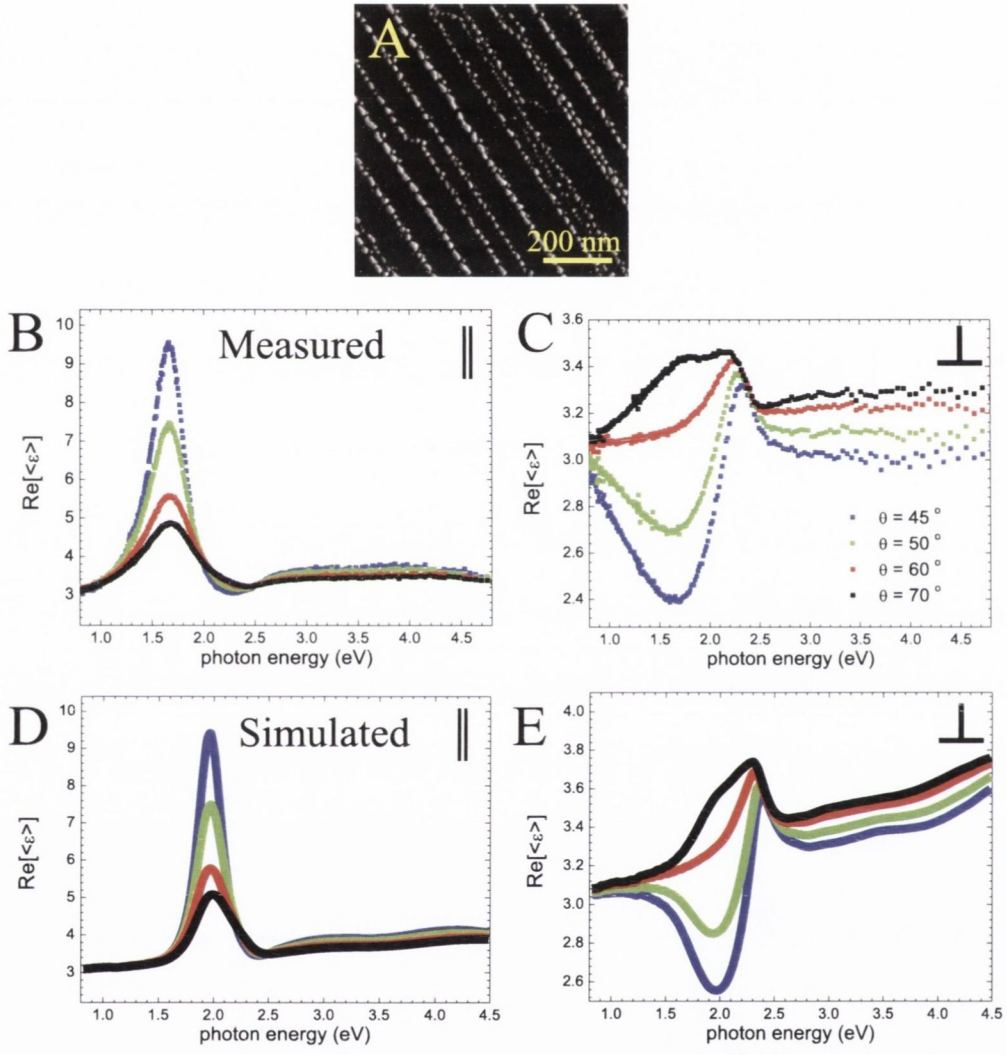

Figure 5.8: SE response of Au NP arrays. (A) SEM image of the in-plane morphology of the sample, where gold NP arrays were produced by glancing angle deposition. Measured pseudo-dielectric function for the measurement configuration parallel (B) and perpendicular (C) to the array. The simulated behaviour for the two cases are shown in (C) and (D) respectively.

Conclusions

In conclusion, this chapter has demonstrated and developed a methodology to investigate the spectral response of complex plasmonic material systems. Simulations were compared with the response of anisotropic NP arrays grown at glancing angles and measured using SE. First, the Anisotropic surface Excess Function (ASEF) was introduced and it was shown how the plasmonic response of a layer can be directly extracted. The formalism is further generalised utilising a transfer matrix method. Different effects that can lead to a modification in the response of the system were discussed and the methodology for a complete analysis outlined. The approach can be used for thick NP layers, anisotropic systems and different materials, and can be extended to magnetic systems and core-shell structures [123].

The results show two advantages over other approaches. First, as SE can measure both the in-plane and out-of-plane response, this technique provides a more stringent test of the validity of models of the plasmonic response. Second, for these anisotropic layers the resonance FOM can be significantly increased at a particular angle of incidence. Measuring the reflectance change in the p and s polarized reflectance at an optimum angle of incidence could lead to a great improvement in the sensitivity of biological sensors based on the detection of changes in the dielectric medium surrounding the NP layer.

Chapter 6

Ag Nanoparticle Arrays for SERS Applications

Research is creating new knowledge.

Neil Armstrong

This chapter will demonstrate that GLAD-based Ag NP arrays can be used as a surface-enhanced Raman spectroscopy (SERS) substrate and a comprehensive study into their applicability for this purpose is presented. The dependence of the SERS enhancement on the plasmonic resonance energy and the polarization of the input light are investigated. It is shown that SERS enhancement factor can be as high as $\sim 3.7 \times 10^6$. Finally the experimental SERS enhancement factors are compared to finite element calculations for quantitative and qualitative analysis.

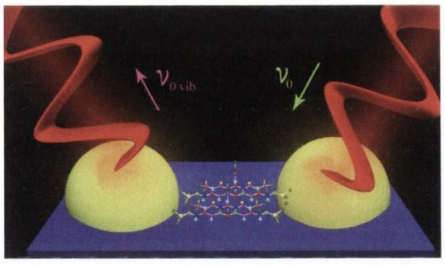

Figure 6.1: Schematic view of the SERS measurement, where the highest electric field occurs between the coupled NPs at the "hotspots".

6.1 Introduction: SERS in Plasmonic Nanostructures

Surface-enhanced Raman spectroscopy (SERS) is a widely explored technique that can provide non-destructive and ultra-sensitive characterization down to the single molecular level [124, 125]. The SERS intensity of Raman signals can be amplified by two main mechanisms, the chemical enhancement and the electromagnetic (EM) enhancement. The EM enhancement originates from the EM fields that have enhanced intensity and are highly localised between NPs composed of noble metals. The EM fields are concentrated by incident light caused by localised plasmonic resonance [126–130]. The SERS signal can be further enhanced when two NPs are closly coupled [131], therefore creating a strong EM field enhancement in the gap. These are referred to as "hot spots" [132–138]. A number of studies highlight the importance of reducing the gap distance between coupled NPs. When the gap is becoming narrower a giant electric field can be produced [125, 139–142]. Moreover, the EM field is largest at the plasmonic resonance maximum, thus the highest SERS enhancement can be achieved by optimizing the plasmonic resonance energies [143–148].

Great challenges still remain in the preparation of optimized substrates for SERS such as fabricating well ordered NPs with a precisely controlled narrow inter-particle

gap, the ability to tune the plasmonic resonance of the arrays, and developing a technique that can generate large areas of NPs quickly and cheaply. Fabricating arrays for use in Raman enhancement is also desirable.

The nanostructure fabrication of GLAD is based on self-assembly and can produce highly ordered one dimensional plasmonic NP chains. We have demonstrated the tunability of the NP dimension, morphology, inter-particle distance (gap) and plasmonic resonance over the whole visible range in previous chapters. These advantages can overcome the SERS substrate production challenges. In order to perform a systematic study of SERS, our focus was to control the gap distance and to precisely tune the plasmonic resonance peak position λ_p. The inter-particle spacing gap d_x, dimension of NP and distance between NP rows (L_y) are controlled by changing the deposition thickness and faceting period of the template.

6.2 Experimental Details

For initial SERS studies, a solution of rhodamine 6G (R6G) as obtained from Sigma-Aldrich (99% dye content) was diluted in methanol without further purification. R6G is a dye and common test molecule for SERS studies [149]. 10 mg R6G were dissolved in 10 ml of methanol and diluted further in Millipore water to reach the desired concentration. Ag NP arrays were grown on the Al_2O_3 in the usual fashion as described in Section 3.2. During growth, the *in-situ* optical signature of the samples was monitored via RAS allowing us to get the required plasmonic resonance position λ_p. For the Ag NP grown sample 1×10^{-6} M concentrated 10 µl R6G solution was drop-cast and left in air for 3 hours to dry. The Raman response was then recorded a few hours after drying using a WITec Alpha 300R Raman spectrometer with laser wavelength $\lambda_i = 532$ nm, laser power $P_i = 37.5$ µW, integration time $t_s = 20$ s. The final Raman spectra was

averaged from 5 different areas of measurement.

A second experiment to investigate the importance of the resonance conditions was carried out with a sample set of Ag NPs grown onto 60 nm, 115 nm and 180 nm faceted templates. For this study 1×10^{-3} M concentrated 20 µl R6G solutions were drop-cast onto samples and left in air for 3 hours to dry. Samples were measured using the WITec Raman spectrometer with $\lambda_i = 532\,\text{nm}$, $P_i = 20\,\mu\text{W}$, $t_s = 2\,\text{s}$, and 25 measurements at different sample points were averaged. Subsequently the samples were examined with the incoming polarization perpendicular and parallel to the NP chains. R6G shows a strong fluorescence signal when excited at 532 nm, hence the background was calculated by fitting a third order polynomial in the region of the spectra where no peak for R6G is known to exist and subtracted from the measured signal. The same spectral region was chosen for each of the samples measured.

In order to compare the enhancement factor on and off resonance, the samples were also examined with a Renishaw inVia Raman spectrometer, equipped with a HeNe-laser ($\lambda_i = 633\,\text{nm}$) operating at $P_i = 500\,\mu\text{W}$. The integration time was chosen to be $t_s = 10\,\text{s}$ and 5 different sample areas were averaged. The laser power was deliberately kept low enough to ensure that the Raman signal from R6G was not degraded during the measurement.

In order to measure the R6G Raman signal on a bare substrate without Ag NP, a much higher concentration of 1×10^{-2} M was required in order to obtain a good enough signal to noise ratio in the Raman measurements. The incident laser ($\lambda_i = 532\,\text{nm}$), laser power ($P_i = 37.5\,\mu\text{W}$), integration time ($t_s = 20\,\text{s}$) and polarization were kept constant. The sample was measured at 25 different areas and average spectra are presented.

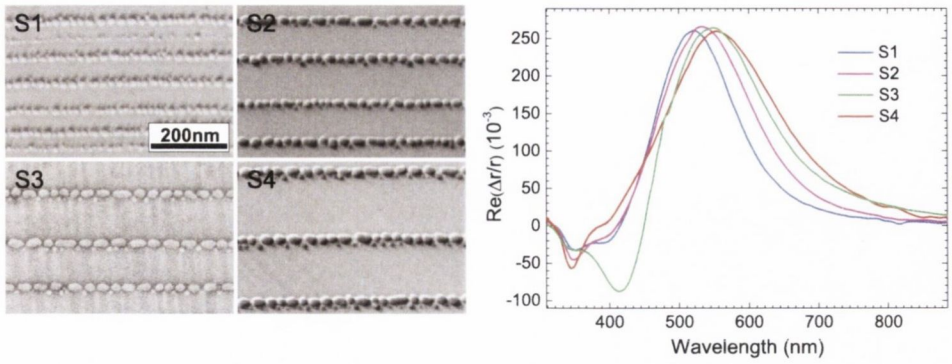

Figure 6.2: (S1, S2, S3, S4) SEM images of a set of Ag NP-arrays grown on 60, 115, 133, 180 nm Al_2O_3 stepped templates. The scale bar is the same for all samples. (Right) *ex-situ* RAS spectra of the all samples. The plasmonic resonance maxima are given in Table 6.1.

Sample Nr.	S1	S2	S3	S4
D_x (nm)	19(6)	22(7)	25(8)	29(11)
D_y (nm)	16(4)	19(5)	22(7)	23(8)
D_z (nm)	10	12	13	15
L_x (nm)	21(10)	25(12)	28(11)	31(14)
L_y (nm)	60(15)	115(19)	133(21)	180(28)
d_x (nm)	2(1)	3(2)	3(2)	2(1)
λ_p, nm	521	535	537	553
d_x/L_x	0.1	0.12	0.1	0.06

Table 6.1: Average morphological parameters of different Ag NP-arrays as derived from a statistical analysis of the SEM images. Values in brackets indicate standard deviation.

6.3 Experimental Results

Ag NP arrays were grown on different stepped Al_2O_3 templates. A set of SEM images of four different samples with the Ag NP arrays is shown in Figure 6.2. The right hand side of Figure 6.2 shows the RAS spectra for all four samples after exposure to atmosphere. The combination of RAS and GLAD techniques provides a reliable and straightforward way of producing highly ordered self-assembled NP arrays where the plasmonic resonance energy can be tuned precisely within the whole visible range [42].

Sample S3 was chosen to demonstrate the potential for the use of Ag NP arrays as

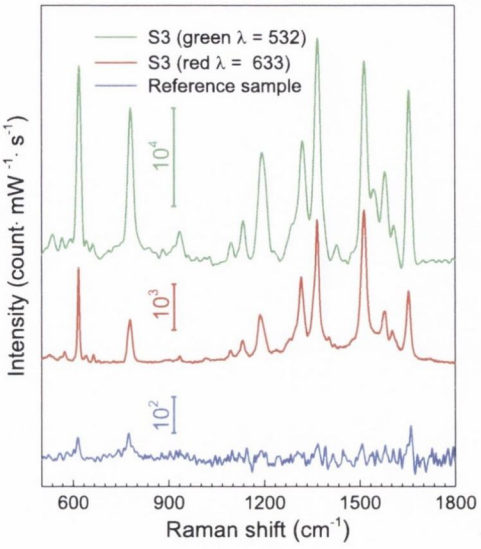

Figure 6.3: Raman spectra of R6G adsorbed on Ag NP substrate (sample S3) after coating with 10^{-6} M R6G aqueous solution. The sample was measured with a green laser (green line) $\lambda_i = 532$ nm and a red laser (red line) $\lambda_i = 633$ nm. The blue line represents the Raman spectrum of a reference sample. 10^{-2} M concentrated R6G solution was coated on an Al_2O_3 bare substrate. Fluorescence background of green and blue lines were subtracted by using the same mask.

SERS substrate, it had an average inter-paticle gap of 3 nm and an *ex-situ* plasmonic resonance with incident light wavelength of 546 nm. The correlation between the plasmonic resonance maximum and SERS enhancement will be shown in Section 6.5. After the optical analysis of the S3 sample, 10^{-6} M concentrated R6G aqueous solutions was applied by drop-cast. The sample was then scanned by Raman spectroscopy and the results are shown in Figure 6.3 (green line). R6G has a strong fluorescence background for excitation with a green laser and a background subtraction as described in the experimental section was required. The Raman peaks observed were related to known peaks for R6G found in a previous report [150], and the vibrational modes corresponding to the main peaks are listed in Table 6.2. These measurements already demonstrate that the Ag NP arrays show an excellent Raman enhancement.

For confirmation of the results, the same sample S3 was investigated with a HeNe

Raman peaks, $\overline{\nu}$ (cm^{-1})	λ_r^a, nm	λ_r^b, nm	assignment[c]
617	550.06	658.73	C-C-C in-plane XRD
778	554.97	665.79	C-H out-of-plane bend
1133	566.12	681.91	C-H in-plane bend
1320	572.18	690.71	in-plane XRB N-H bend
1368	573.76	693.01	XRS, in-plane C-H bend
1514	578.60	700.09	XRS, C-N stretch, C-H bend
1579	580.79	703.29	XRS, in-pane N-H bend
1654	583.33	707.02	XRS, in-plane C-H bend

λ_r^a is for 532 nm green laser, λ_r^b is for 633 nm red laser. [c] XRD: xanthene ring deformations. XRB: xanthene ring breath. XRS: xanthene ring stretch

Table 6.2: Measured Raman peaks of the R6G in experiments and their vibrational mode wavelengths when excited by green (λ_i=532 nm) and red (λ_i=633 nm) laser. The vibrational modes of the R6G for these peaks are also shown. λ_r is Raman signal wavelength.

laser (λ_i = 633 nm) (see Figure 6.3 red line). A high SERS enhancement from the sample was also observed. However, this enhancement is lower than the SERS enhancement obtained with a green laser (λ_i = 532 nm). This is because the wavelength of the red laser is farther from the plasmonic resonance maximum of the sample compared to the green laser.

6.4 SERS Enhancement Dependence on Input Light Polarization

It was decide to investigate the dependence of the Raman intensity on the polarization of incoming light with respect to the lines of NPs. GLAD grown NP arrays can be considered as a well-coupled one dimensional anisotropic system. Their plasmonic resonance depends on the polarization of the incident light. As the NP spacing along the chain (d_x) is substantially lower, the resonance for light polarized along the NP chain is much stronger than when polarized perpendicular. Hence SERS enhance-

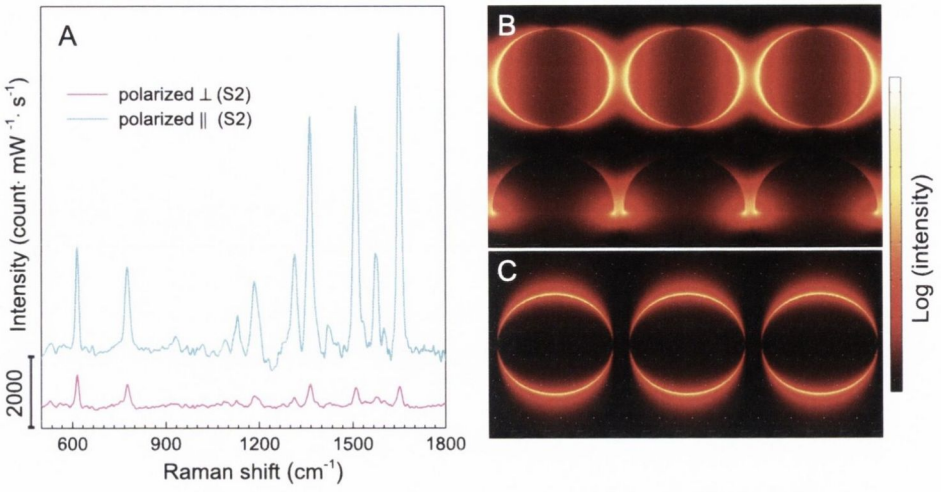

Figure 6.4: (A) Raman spectra of Ag NP arrays with the incident light polarised parallel (cyan line) and perpendicular (magenta line) to the chains of NPs. (B, C) Simulated electric field maps for Ag NP chains subjected to light which is polarized parallel (B, showing both top view and cross section) and perpendicular (C, showing top view) to the NP chains.

ment is expected to depend on the polarization of the incident light. For nanoparticle dimers, numerous studies have reported this polarization dependence of SERS, showing strongest Raman signals for incident light polarized across the dimer junctions [151, 152]. In cases of infinite chains of NPs this effect is even more pronounced. To demonstrate the influence of light polarization, sample S2 was used. The light was polarized along and perpendicular to the NP chains by rotating the sample, keeping the Raman scattering geometry constant. As expected, a strong enhancement only occurs once light is polarized along the NP chains (see Figure 6.4A) and the Raman intensity is approximately 60 times greater compared to the case where the light is polarized perpendicularly to the arrays. As before, the same background signal is subtracted for both spectra.

In order to understand the electric field enhancement at the incident wavelength for a chain of NPs, a FEM simulation using COMSOL Multiphysics® was performed.

For simplicity the average NP size of D_x, D_y, D_z, and average displacement L_x, and L_y of sample S2 as given in Table 6.1 were used to build a model periodic array of identical NPs. The electric field in the gap region between two NPs was calculated for $\lambda_i = 532\,\text{nm}$. Figure 6.4B shows the calculated electric field map for two different polarizations; parallel and perpendicular to the chains. The highest electric field is observed for light polarized along the chains and is located between the NPs. As the FEM calculation, the average electric field intensity is approximately 10 times greater for parallel polarization compared to the perpendicular case. This confirms the importance of the small inter-particle gap for use of NP arrays as SERS substrates.

6.5 SERS Enhancement Dependence on Plasmonic Resonance Maximum

In recent years it has been shown that Ag NP-arrays offer good tunability of the plasmonic resonance [39, 42, 117]. In order to quantify how the plasmonic resonance wavelengths of such samples affects the SERS enhancement, three samples (S1, S2, S4) were investigated (see Figure 6.2 and Table 6.1). C. L. Haynes *et al.* have shown that the highest SERS enhancement was obtained when the plasmonic resonance maximum λ_p was located between the incident λ_i and Raman signal wavelength λ_r [153]. Usually, Raman shifts are typically in wavenumbers $\overline{\nu}$ and it is related to λ_i and λ_r by

$$\overline{\nu} = \left(\frac{1}{\lambda_i} - \frac{1}{\lambda_r}\right) \times 10^7. \tag{6.1}$$

In our case, the experiment was performed by varying the plasmonic resonance maximum relative to a fixed laser wavelength $\lambda_i = 532\,\text{nm}$. The plasmonic resonance energies for the light polarized along the chains of NPs were measured by RAS to be

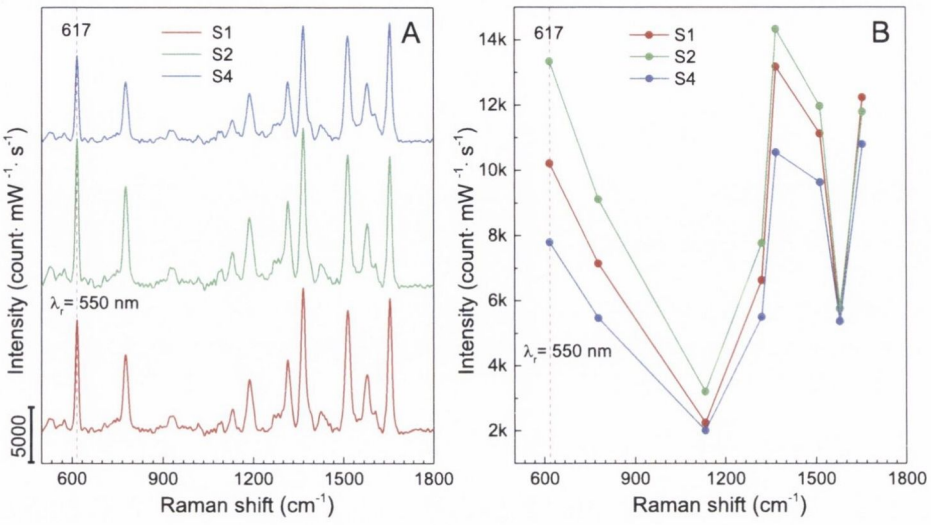

Figure 6.5: (A) Raman spectra of R6G measured on Ag NPs samples (S1, S2, S4) with different plasmonic resonance maximum. The fluorescence of these Raman spectra was subtracted by using the same mask. The dashed magenta line shows the Raman peak of the R6G used for investigation (ν_{vib}=617 cm^{-1}). (B) The dependence of the R6G peak intensity on the plasmonic resonance energy.

521 nm, 535 nm and 553 nm, respectively. A Raman peak of the R6G ($\overline{\nu}$ = 617 cm^{-1}, see the vertical magenta dashed line in Figure 6.5A) was chosen for the investigation and its signal wavelength is λ_r = 550 nm for the incident green laser (see Table 6.2). Therefore, the resonance maximum of 535 nm of S2 is located between λ_i = 532 nm and λ_r = 550 nm while the other two samples (S1 and S4) have resonance maxima outside of this range. Raman spectroscopy was performed on these three samples, the highest SERS enhancement was obtained for the sample S2 with the plasmonic resonance maximum at 535 nm (see Figure 6.5A). The dependence of R6G peak intensity on the plasmonic resonance energy is shown in Figure 6.5B. As expected, the highest SERS enhancement occurred for sample S2 whose value of λ_p lies within the range λ_i - λ_r. These experiments highlight the importance of tuning the plasmonic resonance of the NP array for SERS measurements.

6.6 Enhancement Factor, Comparison of Theory and Experiment

The SERS enhancement factor EF is related to the electric field g at the location of the Raman active molecule for the laser frequency ω_i and the Stokes-shifted frequency of the Raman scattered photon ω_s [154]:

$$EF = [g(\omega_i)]^2[g(\omega_s)]^2 \tag{6.2}$$

For small Raman shifts and relatively broad plasmonic resonances as discussed here, we can assume that the electric field at the incident wavelength and Stokes-shifted frequency are approximately the same. In this case the EF will be equal to the fourth power of the electric field at incident wavelength. The electric field in the Ag NP array at incident wavelength $\lambda_i = 532\,\text{nm}$ was calculated by COMSOL Multiphysics®. For a normalized incident electric field ($E_0 = 1$) the maximum electric field in the Ag NP array was calculated to be $E = 90$. Applying equation 6.2 a local enhancement factor of $EF = 6.5\times10^7$ is expected.

To calculate the effective SERS enhancement factor of a sample (EF_s) from the measurements the same experimental conditions were used for the plasmonic and the bare reference substrate. The only difference is the concentration of R6G in the solution. We had to use more concentrated R6G on the bare substrate as the Raman signal was weaker that on the SERS substrate. In the case of such differences EF is typically expressed in terms of the measured intensity ratio of the plasmonic substrate (I_p) and the reference substrate (I_r) and the ratio of the number of molecules present in both samples (N_p, N_r) [139, 155]. In an ideal case when the same amount of solution stays on both substrates after coating the latter is proportional to the concentration of R6G

applied to the substrates (C_p, C_r):

$$EF_s = \frac{I_p}{I_r}\frac{N_r}{N_p} = \frac{I_p}{I_r}\frac{C_r}{C_p} \tag{6.3}$$

From the experiments I_p, I_r and C_p, C_r are known, and the obtained EF_s of the sample S3 using the equation 6.3 is $EF \sim 3.7 \times 10^6$ ($\overline{\nu} = 617$ was used for calculation).

Conclusion

Self-assembled Ag NP arrays were used as a SERS substrate for detection of R6G. The results showed remarkable SERS enhancement from a GLAD-based SERS substrate of $EF \sim 3.7 \times 10^6$. The dependence of SERS enhancement on plasmonic resonance and polarization was studied. The dependence of EF on polarization was via the plasmonic resonance control: by changing the polarization we tuned in and out of the plasmonic resonance in our linear NP arrays. Finally experimental results were compared with theoretical simulation, confirming the effect of the small NP gaps on the enhancement factor. The GLAD-grown Ag NPs can be used as a SERS substrate for any type of laser as the plasmonic resonance frequency and morphology of NP arrays can be tuned by changing the growth parameters. This overcomes the SERS substrate fabrication challenges and proposes a new avenue for producing SERS substrates as the technique allows for accurate tuning of the frequency as well as ultrasmall NP gaps for vicinal substrates.

Chapter 7

Conclusions and Future Work

The science of today is the
technology of tomorrow

E. Teller

7.1 Conclusion

In this thesis, a method to fabricate highly ordered plasmonic nanostructures by self-assembly using a simple glancing angle deposition (GLAD) technique has been discussed. The possibility of preparing different faceted substrates such as MgO, $SrTiO_3$ and Al_2O_3 for GLAD, their tunable features and transparent optical properties have been shown. The non-specificity of the substrate material opens the door to a wide field of analysis and application.

Highly ordered Ag NP arrangements were successfully produced on different substrates using the GLAD technique and thereby expanding the range of possibilities for this technique and the fabrication of NP arrays generally. Tuning of the NPs geometry through choice of changing the initial substrate's periodicity was extensively studied. The optical properties of the NP arrays have been investigated by both RAS

and UV-Vis spectroscopy. As well as demonstrating the ability of RAS to measure the plasmonic resonances of the arrays, the close relationship between RAS and absorption spectra was also outlined. Furthermore, it was shown that RAS can be used to monitor the growth of the NP arrays *in-situ*.

The possibility of tuning the NP shape by changing the substrate temperature during deposition and using radiation annealing has been demonstrated. Detailed statistical analysis of the shapes of the NPs revealed the influence of heating on their morphology, and RAS was used to analyse the impact of the morphology on their plasmonic properties. Furthermore, multipolar resonances due to sharp edge effects between NP and substrate were observed. Analytical and numerical methods have been used to explain the experimental results and extract semi-quantitative information on the morphology of the NPs. Moreover, alternative materials such as Au and Cu were deposited onto the stepped sapphire substrate by GLAD. The dependence of the NP dimensions and plasmonic resonance on the substrate step periodicities have been studied and their plasmonic resonance positions appear in different energy ranges. Such dichroic plasmonic resonances may be suitable candidates for enhanced spectroscopy with a resonance energy that can be controlled by choosing the material, the initial template periodicity and the deposition thickness. The fact that RAS was carried out as capping deposition took place is a good achievement. The cap caused a shift which is interesting and agree with theory. The RAS signal was also unaffected by exposure to atmosphere when the NPs were capped. This is important for application purpose and an important result.

Spectroscopic ellipsometry (SE) has been used to measure the full out-of-plane optical response of plasmonic structures. Simulations were compared with the response of anisotropic NP arrays grown at glancing angles. The Anisotropic surface Excess Function was introduced and it was shown how the plasmonic response of a layer can be

directly extracted. A more general formalism was then introduced and effects which induce changes in the optical properties in the whole were systematically analysed. It was also shown that polarized spectroscopy has some key advantages in monitoring changes in the refractive index of the medium surrounding the probed NPs when compared with absorption spectroscopy. Sharper resonances can be measured and increases in the figure of merit (FOM), (defined as the shift in resonance with changes in refractive index divided by the width of the peak of the resonance) of up to 15 times have been measured for particular measurement configurations. This could improve the detection limit of refractive index based sensors.

Finally, we have examined the GLAD-grown NP arrays for use as a substrate in surface enhanced Raman spectroscopy (SERS) studies. The dependence of SERS enhancement on input polarization and plasmonic resonances were investigated. Experimental results were compared with theoretical simulations, confirming the effect of the small NP gaps on the enhancement factor. The results showed a remarkable SERS enhancement on the order of 3.7×10^6. This overcomes many challenges with SERS substrate fabrication and opens up a new avenue for the production of SERS substrates.

7.2 Future work

In the course of this thesis detailed experimental and theoretical studies on the self-assembled NP arrays have been performed. There are different important aspects which would then be very interesting for further exploration and represent the core of a possible long term project.

Temperature controlled manipulation of Au and Cu NP arrays: As mentioned in the introduction chapter, great challenges still remain in fabrication of plasmonic nanostructures. The advantages of GLAD based NP arrays to overcome the

challenges faced by traditional methods of NPs fabrication were introduced. The possibility of tuning Ag NP morphology through choice of substrate temperature and through post annealing using a radiative source have been demonstrated. This offers further possibilities for manipulation and optimization of NPs morphology. NP arrays of Au and Cu were also grown. It would be interesting to see if they respond to annealing in similar fashion as the Ag NPs. This may provide insight into the mobility parameters of these materials and may extend the range of resonance energies that NP arrays can be tuned too.

Single molecule SERS investigation: In the last chapter a SERS study has been performed using GLAD based Ag NP arrays. This opens up a new avenue for the production of SERS substrates. As mentioned in this thesis, the size, gap distance and plasmonic resonance of NP arrays are tunable. These features play an important role for SERS substrates. The next aim is to examine GLAD based NP arrays for analysis of solutions of even lower concentration, perhaps even down to single molecule detection. Furthermore, Au NP arrays could be more inserting for SERS investigation, since Au is more stable against affects such as tarnishing and oxidization than the other metals investigated. This is evidenced in the RAS study of Au NP arrays, which showed very little change between the *in-situ* and *ex-situ* measurements. This also implies that the resonance energy of the array can be accurately defined during the growth, since the shift upon exposure to atmosphere is minimal.

A concept of SERS based sensing device: The SERS investigation of GLAD grown nanostructures offers a new possibility for creating a sensing device. The substrate (Al_2O_3) is an insulator and transparent. A schematic illustration of the proposed device is shown in Figure 7.1. Two of the side faces of the substrate are cut at a slight angle, and polished to allow unimpeded transmittance of light. A laser beam is directed through one side towards the NP array on the top surface from beneath. The

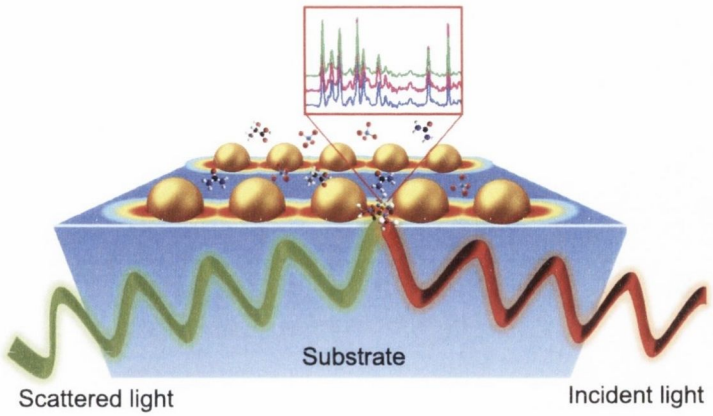

Figure 7.1: A schematic illustration of the concept of SERS based sensing device.

electric field enhancement caused by the NPs causes a strong resonance of the material to be detected. The reflected light then passes through the opposite side face of the substrate to a detector.

The shape of the nanoparticle is effectively a protruding extruded sphere, and the particles are very close coupled, thereby generating strong electric field in the gap region. These features make it a promising candidate for use in a sensing device. Such a device could be used to determine unknown gases, liquids and solid materials and could be use in industrial applications. The main advantages of this device over other techniques is that it is independent of the thickness of the material under investigation. The technique can be used to allow the laser beam to travel to the hotspot on the substrate surface, which allows to perform an accurate measurements and thereby avoids photobleaching and penetration depth problems.

References

[1] S. A. Maier. *Plasmonics: Fundamentals and Applications.* Springer, 2007.

[2] H. J. Chen, F. Wang, K. L, K. C. Woo, J. f. Wang, Q. Li, L. D. Sun, X. Zhang, H. Q. Lin, and C. H. Yan. Plasmonic Percolation: Plasmon-Manifested Dielectric-to-Metal Transition. *ACS Nano*, 6(8):7162–7171, 2012.

[3] S. K. Ghosh and T. Pal. Interparticle Coupling Effect on the Surface Plasmon Resonance of Gold Nanoparticles: From Theory to Applications. *Chemical Reviews*, 107(11):4797–4862, 2007.

[4] Y. H. Su, S. L. Tu, S. W. Tseng, Y. C. Chang, S. H. Chang, and W. M. Zhang. Influence of surface plasmon resonance on the emission intermittency of photoluminescence from gold nano-sea-urchins. *Nanoscale*, 2:2639–2646, 2010.

[5] S. Nie and S. R. Emory. Probing Single Molecules and Single Nanoparticles by Surface-Enhanced Raman Scattering. *Science*, 275(5303):1102–1106, 1997.

[6] N. Engheta. Circuits with Light at Nanoscales: Optical Nanocircuits Inspired by Metamaterials. *Science*, 317(5845):1698–1702, 2007.

[7] D. Yu. Fedyanin, A. V. Krasavin, A. V. Arsenin, and A. V. Zayats. Surface Plasmon Polariton Amplification upon Electrical Injection in Highly Integrated Plasmonic Circuits. *Nano Letters*, 12(5):2459–2463, 2012.

[8] U. Kreibig and M. Vollmer. *Optical Properties of Metal Clusters.* Springer, Berlin, 1957.

[9] A. Bouhelier, R. Bachelot, J. S. Im, G. P. Wiederrecht, G. Lerondel, S. Kostcheev, and P. Royer. Electromagnetic Interactions in Plasmonic Nanoparticle Arrays. *The Journal of Physical Chemistry B*, 109(8):3195–3198, 2005.

[10] L. Shao, K. C. Woo, H. J. Chen, Z. Jin, J. F. Wang, and H. Q. Lin. Angle - and Energy-Resolved Plasmon Coupling in Gold Nanorod Dimers. *ACS Nano*, 4(6): 3053–3062, 2010.

[11] M. Quinten, A. Leitner, J. R. Krenn, and F. R. Aussenegg. Electromagnetic energy transport via linear chains of silver nanoparticles. *Optics Letters*, 23(17): 1331–1333, Sep 1998.

[12] B. Lamprecht, G. Schider, R. T. Lechner, H. Ditlbacher, J. R. Krenn, A. Leitner, and F. R. Aussenegg. Metal Nanoparticle Gratings: Influence of Dipolar Particle Interaction on the Plasmon Resonance. *Physical Review Letters*, 84:4721–4724, May 2000.

[13] A. M. Stefan, G. K. Pieter, A. A. Harry, M Sheffer, H. Elad, E. K. Bruce, and A. G. R. Ari. Local detection of electromagnetic energy transport below the diffraction limit in metal nanoparticle plasmon waveguides. *Nature Materials*, 2: 229–232, April 2003.

[14] C. Hanske, M. Tebbe, C. Kuttner, V. Bieber, V. V. Tsukruk, M. Chanana, T. A. F. König, and A. Fery. Strongly Coupled Plasmonic Modes on Macroscopic Areas via Template-Assisted Colloidal Self-Assembly. *Nano Letters*, 14(12):6863–6871, 2014.

[15] G. Pellegrini, G. Mattei, and P. Mazzoldi. Tunable, directional and wavelength selective plasmonic nanoantenna arrays. *Nanotechnology*, 20(6):065201, 2009.

[16] H. A. Atwater and A. Polman. Plasmonics for improved photovoltaic devices. *Nature Materials*, 9:205–213, March 2010.

[17] P. Jain, X. H. Huang, I. El-Sayed, and M. El-Sayed. Review of Some Interesting Surface Plasmon Resonance-enhanced Properties of Noble Metal Nanoparticles and Their Applications to Biosystems. *Plasmonics*, 2:107–118, 2007.

[18] S. Zou and G. C. Schatz. Silver nanoparticle array structures that produce giant enhancements in electromagnetic fields. *Chemical Physics Letters*, 403(1-3):62 – 67, 2005.

[19] S. Kim, J. Jin, Y. J. Kim, I. Y. Park, Y. Kim, and S. W. Kim. High-harmonic generation by resonant plasmon field enhancement. *Nature*, 453:757–760, June 2008.

[20] Z. F. Kinkhabwala, Yu, S. H. Fan, Y. Avlasevich, K. Mullen, and W. E. Moerner. Large single-molecule fluorescence enhancements produced by a bowtie nanoantenna. *Nature Photonics*, 3:654–657, Novamber 2009.

[21] A. N. Grigorenko, N. W. Roberts, M. R. Dickinson, and Y. Zhang. Nanometric optical tweezers based on nanostructured substrates. *Nature Photonics*, 2:365–370, June 2008.

[22] E. M. Hicks, S. L. Zou, G. C. Schatz, K. G. Spears, R. P. Van Duyne, L. Gunnarsson, T. Rindzevicius, B. Kasemo, and M. Käll. Controlling Plasmon Line Shapes through Diffractive Coupling in Linear Arrays of Cylindrical Nanoparticles Fabricated by Electron Beam Lithography. *Nano Letters*, 5(6):1065–1070, 2005.

[23] S. Aksu, A. A. Yanik, R. Adato, A. Artar, M. Huang, and H. Altug. High-Throughput Nanofabrication of Infrared Plasmonic Nanoantenna Arrays for Vibrational Nanospectroscopy. *Nano Letters*, 10(7):2511–2518, 2010.

[24] B. Radha and G. U. Kulkarni. An electrical rectifier based on Au nanoparticle array fabricated using direct-write electron beam lithography. *Advanced Functional Materials*.

[25] S. Tripathy, R. Marty, V. K. Lin, S. L. Teo, E. Ye, A. Arbouet, L. Saviot, C. Girard, M. Y. Han, and A. Mlayah. Acousto-plasmonic and surface-enhanced Raman scattering properties of coupled gold nanospheres/nanodisk trimers. *Nano Letters*, 11(2):431–437, 2011.

[26] A. R. Tao, S. Habas, and P. Yang. Shape Control of Colloidal Metal Nanocrystals. *Small*, 4(3):310–325, 2008.

[27] S. Imamova, N. Nedyalkov, A. Dikovska, P. Atanasov, M. Sawczak, R. Jendrzejewski, G. Sliwinski, and M. Obara. Near field properties of nanoparticle arrays fabricated by laser annealing of thin Au and Ag films. *Applied Surface Science*, 257(3):1075 – 1079, 2010.

[28] C. L. Haynes and R. P. Van Duyne. Nanosphere Lithography: A Versatile Nanofabrication Tool for Studies of Size-Dependent Nanoparticle Optics. *The Journal of Physical Chemistry B*, 105(24):5599–5611, 2001.

[29] S. W. Lee, K. S. Lee, J. Ahn, J. J. Lee, M. G. Kim, and Y. B. Shin. Highly Sensitive Biosensing Using Arrays of Plasmonic Au Nanodisks Realized by Nanoimprint Lithography. *ACS Nano*, 5(2):897–904, 2011.

[30] L. M. Kukreja, S. Verma, D. A. Pathrose, and B. T. Rao. Pulsed laser deposition of plasmonic-metal nanostructures. *Journal of Physics D: Applied Physics*, 47 (3):034015, 2014.

[31] T. Donnelly, S. Krishnamurthy, K. Carney, N. McEvoy, and J.G. Lunney. Pulsed laser deposition of nanoparticle films of Au. *Applied Surface Science*, 254(4): 1303–1306, 2007.

[32] T. S. Ahmadi, Z. L. Wang, T. C. Green, A. Henglein, and M. A. El-Sayed. Shape-Controlled Synthesis of Colloidal Platinum Nanoparticles. *Science*, 272 (5270):1924–1925, 1996.

[33] A. Panáček, L. Kvítek, R. Prucek, M. Kolář, R. Večeřová, N. Pizúrová, V. K. Sharma, T. Nevěčná, and R. Zbořil. Silver Colloid Nanoparticles: Synthesis, Characterization, and Their Antibacterial Activity. *The Journal of Physical Chemistry B*, 110(33):16248–16253, 2006.

[34] S. Camelio, D. Babonneau, D. Lantiat, and L. Simonot. Self-organized growth and optical properties of silver nanoparticle chains and stripes. *Europhysics Letters*, 79(4):47002, 2007.

[35] T. W. H. Oates, A. Keller, S. Facsko, and A. Mücklich. Aligned Silver Nanoparticles on Rippled Silicon Templates Exhibiting Anisotropic Plasmon Absorption. *Plasmonics*, 2(2):47–50, 2007.

[36] I. V. Shvets, H. C. Wu, V. Usov, F. Cuccureddu, S. K. Arora, and S. Murphy. Concept of a nanowire array magnetoresistance device. *Applied Physics Letters*, 92(2):023107, 2008.

[37] F. Cuccureddu, S. Murphy, I. V. Shvets, M. Porcu, and H. W. Zandbergen. Plasmon Resonance in Silver Nanoparticles Arrays Grown by Atomic Terrace Low-Angle Shadowing. *Nano Letters*, 8(10):3248–3256, 2008.

[38] R. Verre, K. Fleischer, R. G. S. Sofin, N. McAlinden, J. F. McGilp, and I. V. Shvets. *In situ* characterization of one-dimensional plasmonic Ag nanocluster arrays. *Physical Review B*, 83(12):125432–125440, Mar 2011.

[39] R. Verre, K. Fleischer, J. F. McGilp, D. Fox, G. Behan, H. Zhang, and I. V. Shvets. Controlled *in situ* growth of tunable plasmonic self-assembled nanoparticle arrays. *Nanotechnology*, 23(3):035606, 2012.

[40] K. Robbie and M. J. Brett. Sculptured thin films and glancing angle deposition: Growth mechanics and applications. *Journal of Vacuum Science & Technology A*, 15(3):1460–1465, 1997.

[41] M. J. Brett and M. M. Hawkeye. New Materials at a Glance. *Science*, 319(5867): 1192–1193, 2008.

[42] R. Verre, K. Fleischer, O. Ualibek, and I. V. Shvets. Self-assembled broadband plasmonic nanoparticle arrays for sensing applications. *Applied Physics Letters*, 100(3):031102, 2012.

[43] R. Lazzari and J. Jupille. Quantitative analysis of nanoparticle growth through plasmonics. *Nanotechnology*, 22(44):445703, 2011.

[44] P. Politi, G. Grenet, A. Marty, A. Ponchet, and J. Villain. Instabilities in crystal growth by atomic or molecular beams. *Physics Reports*, 324(56):271–404, 2000.

[45] A. Dolatshahi-Pirouz, M. B. Hovgaard, K. Rechendorff, J. Chevallier, M. Foss, and F. Besenbacher. Scaling behavior of the surface roughness of platinum films grown by oblique angle deposition. *Physical Review B*, 77:115427, Mar 2008.

[46] P. C. Wu, T. H. Kim, A. S. Brown, M. Losurdo, G. Bruno, and H. O. Everitt. Real-time plasmon resonance tuning of liquid Ga nanoparticles by *in situ* spectroscopic ellipsometry. *Applied Physics Letters*, 90(10):103119, 2007.

[47] M. Losurdo, M. Bergmair, G. Bruno, D. Cattelan, C. Cobet, A. de Martino, K. Fleischer, Z. Dohcevic-Mitrovic, N. Esser, M. Galliet, R. Gajic, D. Hemzal,

K. Hingerl, J. Humlicek, R. Ossikovski, Z. V. Popovic, and O. Saxl. Spectroscopic ellipsometry and polarimetry for materials and systems analysis at the nanometer scale: state-of-the-art, potential, and perspectives. *Journal of Nanoparticle Research*, 11(7):1521–1554, 2009.

[48] K. Vedam. Spectroscopic ellipsometry: a historical overview. *Thin Solid Films*, 313314(0):1–9, 1998.

[49] K. L. Kelly, E. Coronado, L. L. Zhao, and G. C. Schatz. The Optical Properties of Metal Nanoparticles: The Influence of Size, Shape, and Dielectric Environment. *The Journal of Physical Chemistry B*, 107(3):668–677, 2003.

[50] U. Leonhardt. Optical metamaterials: Invisibility cup. *Nature Photonics*, 1: 207–208, April 2007.

[51] M. R. Gartia, A. Hsiao, A. Pokhriyal, S. Seo, G. Kulsharova, B. T. Cunningham, T. C. Bond, and G. L. Liu. Colorimetric Plasmon Resonance Imaging Using Nano Lycurgus Cup Arrays. *Advanced Optical Materials*, 1(1):68–76, 2013.

[52] M. Faraday. The Bakerian Lecture: Experimental Relations of Gold (and Other Metals) to Light. *Philosophical Transactions of the Royal Society of London*, 147, January 1857.

[53] Gustav Mie. Beiträge zur Optik trüber Medien, speziell kolloidaler Metallösungen. *Annalen der Physik*, 330(3):377–445, 1908.

[54] P. Drude. Zur Elektronentheorie der Metalle. *Annalen der Physik*, 306(3):566–613, 1900.

[55] C. F. Bohren and D. R. Huffman. *Absorption and scattering of light by small particles*. Wiley, New York, 1983.

[56] R. Lazzari, S. Roux, I. Simonsen, J. Jupille, D. Bedeaux, and J. Vlieger. Multipolar plasmon resonances in supported silver particles: The case of Ag/α-Al_2O_3(0001). *Physical Review B*, 65:235424, Jun 2002.

[57] Ruggero Verre. *PhD thesis: Spectroscopic studies of self-assembled plasmonic nanoparticle arrays*. Trinity College Dublin, September 2011.

[58] A. Pinchuk, A. Hilger, G. Plessen, and U. Kreibig. Substrate effect on the optical response of silver nanoparticles. *Nanotechnology*, 15(12):1890, 2004.

[59] T. Yamaguchi, S. Yoshida, and A. Kinbara. Optical effect of the substrate on the anomalous absorption of aggregated silver films. *Thin Solid Films*, 21(1): 173–187, 1974.

[60] R. G. Barrera, M. del Castillo-Mussot, G. Monsivais, P. Villaseor, and W. L. Mochán. Optical properties of two-dimensional disordered systems on a substrate. *Physical Review B*, 43:13819–13826, Jun 1991.

[61] M. Valamanesh, Y. Borensztein, C. Langlois, and E. Lacaze. Substrate Effect on the Plasmon Resonance of Supported Flat Silver Nanoparticles. *The Journal of Physical Chemistry C*, 115(7):2914–2922, 2011.

[62] J. D. E. McIntyre and D. E. Aspnes. Differential reflection spectroscopy of very thin surface films. *Surface Science*, 24(2):417–434, 1971.

[63] M. Born and E. Wolf. *Principles of Optics*. Cambridge University Press, seventh edition, 1999.

[64] D. W. Berreman. Optics in Stratified and Anisotropic Media: 4 × 4 - Matrix Formulation. *Journal of the Optical Society of America*, 62(4):502–510, Apr 1972.

[65] M. Schubert. Polarization-dependent optical parameters of arbitrarily anisotropic homogeneous layered systems. *Physical Review B*, 53:4265–4274, Feb 1996.

[66] M. Schubert, T. E. Tiwald, and J. A. Woollam. Explicit Solutions for the Optical Properties of Arbitrary Magneto-Optic Materials in Generalized Ellipsometry. *Applied Optics*, 38(1):177–187, Jan 1999.

[67] L. Persechini, R. Verre, N. McAlinden, J. J. Wang, M. Ranjan, S. Facsko, I. V. Shvets, and J. F. McGilp. An analytic approach to modeling the optical response of anisotropic nanoparticle arrays at surfaces and interfaces. *Journal of Physics: Condensed Matter*, 26(14):145302, 2014.

[68] H. Hövel, S. Fritz, A. Hilger, U. Kreibig, and M. Vollmer. Width of cluster plasmon resonances: Bulk dielectric functions and chemical interface damping. *Physical Review B*, 48:18178–18188, Dec 1993.

[69] P. M. Martin. *Handbook of Deposition Technologies for Films and Coatings (Third Edition)*. William Andrew Publishing, Boston, third edition edition, 2010.

[70] E. C. Jelks, G. L. Kerber, and H. A. Wilcox. A simple method for fabricating lines of 0.15-μ width using optical lithography. *Applied Physics Letters*, 34(1): 28–30, 1979.

[71] L. F. Johnson, K. A. Ingersoll, and G. W. Kammlott. An oblique shadow deposition technique for altering the profile of grating relief patterns on surfaces. *Applied Physics Letters*, 34(9):578–580, 1979.

[72] F. Cuccureddu, V. Usov, S. Murphy, C. O. Coileain, and I. V. Shvets. Planar nanowire arrays formed by atomic-terrace low-angle shadowing. *Review of Scientific Instruments*, 79:053907, 2008.

[73] P. Weightman, D. S. Martin, R. J. Cole, and T. Farrell. Reflection anisotropy spectroscopy. *Reports on Progress in Physics*, 68(6):1251, 2005.

[74] D. E. Aspnes and A. A. Studna. Anisotropies in the Above-Band-Gap Optical Spectra of Cubic Semiconductors. *Physical Review Letters*, 54:1956–1959, Apr 1985.

[75] J. T. Zettler. Characterization of epitaxial semiconductor growth by reflectance anisotropy spectroscopy and ellipsometry. *Progress in Crystal Growth and Characterization of Materials*, 35(1):27–98, 1997.

[76] H. Fujiwara. *Spectroscopic Ellipsometry: Principles and Applications*. John Wiley & Sons, Ltd, 2007.

[77] G. Binnig, C. F. Quate, and Ch. Gerber. Atomic Force Microscope. *Physical Review Letters*, 56:930–933, Mar 1986.

[78] D. Sarid. *Scanning Force Microscopy: With Applications to Electric, Magnetic, and Atomic Forces*. Oxford University Press, 1994.

[79] G. Lawes. *Scanning electron microscopy and X-ray microanalysis*. Published on behalf of ACOL by Wiley, 1987.

[80] Dieringer J. A. Shah N. C. Van Duyne R. P. Stiles, P. L. Surface-enhanced Raman spectroscopy. *Annual Review of Analytical Chemistry*, 1(1):601–626, 2008.

[81] R. Gabai, A. Ismach, and E. Joselevich. Nanofacet Lithography: A New Bottom-Up Approach to Nanopatterning and Nanofabrication by Soft Replication of Spontaneously Faceted Crystal Surfaces. *Advanced Materials*, 19(10):1325–1330, 2007.

[82] J. R. Heffelfinger, M. W. Bench, and C. B. Carter. Steps and the structure of the (0001) α-alumina surface. *Surface Science*, 370(1):L168–L172, 1997.

[83] L. Pham Van, O. Kurnosikov, and J. Cousty. Evolution of steps on vicinal (0001) surfaces of α-alumina. *Surface Science*, 411(3):263–271, 1998.

[84] R. Verre, R.G.S. Sofin, V. Usov, K. Fleischer, D. Fox, G. Behan, H. Zhang, and I.V. Shvets. Equilibrium faceting formation in vicinal Al_2O_3 (0001) surface caused by annealing. *Surface Science*, 606(23-24):1815–1820, 2012.

[85] V. E. Henrich. Thermal faceting of (110) and (111) surfaces of MgO. *Surface Science*, 57(1):385–392, 1976.

[86] S. B. Lee, W. Sigle, W. Kurtz, and M. Rühle. Temperature dependence of faceting in $\Sigma5(310)[001]$ grain boundary of $SrTiO_3$. *Acta Materialia*, 51(4):975–981, 2003.

[87] A. Syrlybekov1, E. Arca, R. Verre, C. O. Coileain, O. Toktarbaiuly, A. Khalid, H. Zhang, and I. V. Shvets1. Induced morphological changes on vicinal MgO (100) subjected to high temperature annealing: step formation and surface stability. *Submitted to Surface Science.*

[88] A. Syrlybekov, E. Arca, R. Verre, C. O. Coileain, R.G.S Sofin, R. Ramos, O. Toktarbaiuly, A. Khalid, H. Zhang, and I. V. Shvets1. Surface faceting of vicinal $SrTiO_3$ (100). *In preparation.*

[89] M. Kitayama and A. M. Glaeser. The Wulff Shape of Alumina: III, Undoped Alumina. *Journal of the American Ceramic Society*, 85(3):611–622, 2002.

[90] T. Sano, D. M. Saylor, and G. S. Rohrer. Surface Energy Anisotropy of $SrTiO_3$ at 1400 °C in Air. *Journal of the American Ceramic Society*, 86(11):1933–1939, 2003.

[91] E. T. Dong, P. Shen, L. X. Shi, D. Zhang, and Q. C. Jiang. Wetting and adhesion at Mg/MgO interfaces. *Journal of Materials Science*, 48(17):6008–6017, 2013.

[92] J. N. Anker, W. P. Hall, O. Lyandres, N. C. Shah, J. Zhao, and R. P. Van Duyne. Biosensing with plasmonic nanosensors. *Nature Materials*, 7:442–453, Jun 2008.

[93] A. Marmier and S. C. Parker. *Ab initio* morphology and surface thermodynamics of α - Al_2O_3. *Physical Review B*, 69:115409, Mar 2004.

[94] C. T. Campbell. Ultrathin metal films and particles on oxide surfaces: structural, electronic and chemisorptive properties. *Surface Science Reports*, 27(1):1–111, 1997.

[95] M. M. Burns, J. Fournier, and J. A. Golovchenko. Optical binding. *Physical Review Letters*, 63:1233–1236, Sep 1989.

[96] M. Righini, C. Girard, and R. Quidant. Light-induced manipulation with surface plasmons. *Journal of Optics A: Pure and Applied Optics*, 10(9):093001, 2008.

[97] V. Garcés-Chávez, R. Quidant, P. J. Reece, G. Badenes, L. Torner, and K. Dholakia. Extended organization of colloidal microparticles by surface plasmon polariton excitation. *Physical Review B*, 73:085417, Feb 2006.

[98] P. B. Johnson and R. W. Christy. Optical Constants of the Noble Metals. *Physical Review B*, 6:4370–4379, Dec 1972.

[99] Y. Shen, J. Zhou, T. Liu, Y. Tao, R. Jiang, M. Liu, G. Xiao, J. Zhu, Z. K. Zhou, X. Wang, C. Jin, and J. Wang. Plasmonic gold mushroom arrays with refractive index sensing figures of merit approaching the theoretical limit. *Nature Communications*, 4:17435–17442, August 2013.

[100] M. Piliarik, P. Kvasnička, N. Galler, J. R. Krenn, and J. Homola. Local refractive index sensitivity of plasmonic nanoparticles. *Optics Express*, 19(10):9213–9220, May 2011.

[101] L. Tian, E. Chen, N. Gandra, A. Abbas, and S. Singamaneni. Gold Nanorods as Plasmonic Nanotransducers: Distance-Dependent Refractive Index Sensitivity. *Langmuir*, 28(50):17435–17442, 2012.

[102] T. Abhilash, M. Balasubrahmaniyam, Anuradha Patra, and S. Kasiviswanathan. Plasmon resonance mediated enhancement in Fabry-Pérot cavity modes. *Applied Physics Letters*, 104(24):–, 2014.

[103] R. Gomez-Medina, N. Yamamoto, M. Nakano, and F. J. Garcia de Abajo. Mapping plasmons in nanoantennas via cathodoluminescence. *New Journal of Physics*, 10(10):105009, 2008.

[104] E. J. R. Vesseur, F. J. Garcia de Abajo, and A. Polman. Modal Decomposition of Surface-Plasmon Whispering Gallery Resonators. *Nano Letters*, 9(9):3147–3150, 2009.

[105] J. A. Scholl, A. L. Koh, and J. A. Dionne. Quantum plasmon resonances of individual metallic nanoparticles. *Nature*, 483:421–427, March 2012.

[106] J. Nelayah, M. Kociak, O. Stephan, F. J. Garcia de Abajo, M. Tence, L. Henrard, D. Taverna, I. Pastoriza-Santos, L. M. Liz-Marzan, and C. Colliex. Mapping surface plasmons on a single metallic nanoparticle. *Nature Physics*, 3:348–353, 2007.

[107] R. M. A. Azzam and N. M. Bashara. *Ellipsometry and polarized light*. North Holland, 1977.

[108] T. W. H. Oates, H. Wormeester, and H. Arwin. Characterization of plasmonic effects in thin films and metamaterials using spectroscopic ellipsometry . *Progress in Surface Science*, 86(1112):328–376, 2011.

[109] K. Mok, N. Du, and H. Schmidt. Vector-magneto-optical generalized ellipsometry. *Review of Scientific Instruments*, 82(3):033112, 2011.

[110] Y. Lo, W. Hsieh, Y. Chung, and S. Tsai. An Approach for Measuring the Ellipsometric Parameters of Isotropic and Anisotropic Thin Films Using the Stokes Parameter Method. *Journal of Lightwave Technology*, 30(14):2299–2306, Jul 2012.

[111] R. S. Moirangthem, Y. C. Chang, and P. K. Wei. Ellipsometry study on gold-nanoparticle-coated gold thin film for biosensing application. *Biomedical Optics Express*, 2(9):2569–2576, Sep 2011.

[112] V. G. Kravets, F. Schedin, R. Jalil, L. Britnell, R. V. Gorbachev, D. Ansell, B. Thackray, K. S. Novoselov, A. K. Geim, A. V. Kabashin, and A. N. Grigorenko. Singular phase nano-optics in plasmonic metamaterials for label-free single-molecule detection. *Nature Materials*, 12(4):304–309, 2013.

[113] J. M. Flores-Camacho, L. D. Sun, N. Saucedo-Zeni, G. Weidlinger, M. Hohage, and P. Zeppenfeld. Optical anisotropies of metal clusters supported on a birefringent substrate. *Physical Review B*, 78:075416, Aug 2008.

[114] P. C Wu, M. Losurdo, T. H. Kim, B. Garcia-Cueto, F. Moreno, G. Bruno, and A. S. Brown. Ga-Mg Core-Shell Nanosystem for a Novel Full Color Plasmonics. *The Journal of Physical Chemistry C*, 115(28):13571–13576, 2011.

[115] K. Lodewijks, W. Van Roy, G. Borghs, L. Lagae, and P. Van Dorpe. Boosting the Figure-Of-Merit of LSPR-Based Refractive Index Sensing by Phase-Sensitive Measurements. *Nano Letters*, 12(3):1655–1659, 2012.

[116] S. Zhu, T. P. Chen, Y. C. Liu, Y. Liu, and S. F. Yu. Influence of SiO_2 Layer on the Dielectric Function of Gold Nanoparticles on Si Substrate. *Electrochemical and Solid-State Letters*, 15(1):K5–K9, 2012.

[117] R. Verre, K. Fleischer, C. Smith, N. McAlinden, J. F. McGilp, and I. V. Shvets. Probing the out-of-plane optical response of plasmonic nanostructures using spectroscopic ellipsometry. *Physical Review B*, 84:085440, Aug 2011.

[118] M. K. Kelly, S. Zollner, and M. Cardona. Modelling the optical response of surfaces measured by spectroscopic ellipsometry: application to Si and Ge. *Surface Science*, 285(3):282–294, 1993.

[119] Über die bestimmung der optischen konstanten dünnster oberflächenschichten und das problem der schichtdicke. *Surface Science*, 64(2):484–496, 1977.

[120] P. V. Santos, B. Koopmans, N. Esser, W. G. Schmidt, and F. Bechstedt. Optical Properties of Ordered As Layers on InP(110) Surfaces. *Physical Review Letters*, 77(4):759–762, Jul 1996.

[121] T. Yamaguchi, S. Yoshida, and A. Kinbara. Anomalous optical absorption of aggregated silver films. *Thin Solid Films*, 18(1):63–70, 1973.

[122] O. Ualibek, R. Verre, B. Bulfin, V. Usov, K. Fleischer, J. F. McGilp, and I. V. Shvets. Manipulating and probing the growth of plasmonic nanoparticle arrays using light. *Nanoscale*, 5:4923–4930, 2013.

[123] M. Abe and T. Suwa. Surface plasma resonance and magneto-optical enhancement in composites containing multicore-shell structured nanoparticles. *Physical Review B*, 70:235103, Dec 2004.

[124] K. Kneipp, H. Kneipp, I. Itzkan, R. R. Dasari, and M. S. Feld. Surface-enhanced Raman scattering and biophysics. *Journal of Physics: Condensed Matter*, 14 (18):R597, 2002.

[125] J. F. Li, Y. F. Huang, Y. Ding, Z. L. Yang, S. B. Li, X. S. Zhou, F. R. Fan, W. Zhang, Z. Y. Zhou, D. Y. Wu, B. Ren, Z. L. Wang, and Z. Q. Tian. Shell-isolated nanoparticle-enhanced Raman spectroscopy. *Nature*, 464(7287):392–395, Mar 2010.

[126] K. A. Willets and R. P. Van Duyne. Localized Surface Plasmon Resonance Spectroscopy and Sensing. *Annual Review of Physical Chemistry*, 58(1):267–297, 2007.

[127] F. J. García-Vidal and J. B. Pendry. Collective Theory for Surface Enhanced Raman Scattering. *Physical Review Letters*, 77:1163–1166, Aug 1996.

[128] M. Moskovits. Surface-enhanced spectroscopy. *Reviews of Modern Physics*, 57: 783–826, Jul 1985.

[129] H. X. Xu, J. Aizpurua, M. Käll, and P. Apell. Electromagnetic contributions to single-molecule sensitivity in surface-enhanced Raman scattering. *Physical Review E*, 62:4318–4324, Sep 2000.

[130] Zhong-Qun Tian, Bin Ren, and De-Yin Wu. Surface-Enhanced Raman Scattering: From Noble to Transition Metals and from Rough Surfaces to Ordered Nanostructures. *The Journal of Physical Chemistry B*, 106(37):9463–9483, 2002.

[131] N. Pazos-Perez, W. Ni, A. Schweikart, R. A. Alvarez-Puebla, A. Fery, and L. M. Liz-Marzan. Highly uniform SERS substrates formed by wrinkle-confined drying of gold colloids. *Chemical Science*, 1:174–178, 2010.

[132] J. P. Camden, J. A. Dieringer, Y. M. Wang, D. J. Masiello, L. D. Marks, G. C. Schatz, and R. P. Van Duyne. Probing the Structure of Single-Molecule Surface-Enhanced Raman Scattering Hot Spots. *Journal of the American Chemical Society*, 130(38):12616–12617, 2008.

[133] G. Chen, Y. Wang, M. X. Yang, J. Xu, S. J. Goh, M. Pan, and H. Y. Chen. Measuring Ensemble-Averaged Surface-Enhanced Raman Scattering in the Hotspots of Colloidal Nanoparticle Dimers and Trimers. *Journal of the American Chemical Society*, 132(11):3644–3645, 2010.

[134] C. E. Talley, J. B. Jackson, C. Oubre, N. K. Grady, C. W. Hollars, S. M. Lane, T. R. Huser, P. Nordlander, and N. J. Halas. Surface-Enhanced Raman Scattering from Individual Au Nanoparticles and Nanoparticle Dimer Substrates. *Nano Letters*, 5(8):1569–1574, 2005.

[135] W. Y. Li, P. H. C. Camargo, X. M. Lu, and Y. N. Xia. Dimers of Silver Nanospheres: Facile Synthesis and Their Use as Hot Spots for Surface-Enhanced Raman Scattering. *Nano Letters*, 9(1):485–490, 2009.

[136] S. Y. Lee, L. Hung, G. S. Lang, J. E. Cornett, I. D. Mayergoyz, and O. Rabin. Dispersion in the SERS Enhancement with Silver Nanocube Dimers. *ACS Nano*, 4(10):5763–5772, 2010.

[137] X. Wang, M. H. Li, L. Y. Meng, K. Q. Lin, J. M. Feng, T. X. Huang, Z. L. Yang, and B. Ren. Probing the Location of Hot Spots by Surface-Enhanced Raman Spectroscopy: Toward Uniform Substrates. *ACS Nano*, 8(1):528–536, 2014.

[138] R. Jin. Nanoparticle Clusters Light Up in SERS. *Angewandte Chemie International Edition*, 49(16):2826–2829, 2010.

[139] W. J. Cho, Y. Kim, and J. K. Kim. Ultrahigh-Density Array of Silver Nanoclusters for SERS Substrate with High Sensitivity and Excellent Reproducibility. *ACS Nano*, 6(1):249–255, 2012.

[140] D. K. Lim, K. S. Jeon, J. H. Hwang, H. Kim, S. Kwon, Y. D. Suh, and J. M. Nam. Highly uniform and reproducible surface-enhanced Raman scattering from DNA-tailorable nanoparticles with 1-nm interior gap. *Nature Nanotechnology*, 6 (7):452–460, July 2011.

[141] K. D. Alexander, S. Zhang, A. R. H. Walker, H. X. Xu, and R. Lopez. Relationship between Length and Surface-Enhanced Raman Spectroscopy Signal Strength in Metal Nanoparticle Chains: Ideal Models versus Nanofabrication. *Journal of Nanotechnology*, 83(840245):1–7, Mar 2012.

[142] J. Clara-Rahola, R. Contreras-Caceres, B. Sierra-Martin, A. Maldonado-Valdivia, M. Hund, A. Fery, T. Hellweg, and A. Fernandez-Barbero. Structure and plasmon coupling of gold-poly(N-isopropylacrylamide) coreshell microgel arrays with thermally controlled interparticle gap. *Colloids and Surfaces A: Physicochemical and Engineering Aspects*, 463(0):18–27, 2014.

[143] X. Y. Zhang, A. Hu, T. Zhang, W. Lei, X. J. Xue, Y. Zhou, and W. W. Duley. Self-Assembly of Large-Scale and Ultrathin Silver Nanoplate Films with Tunable Plasmon Resonance Properties. *ACS Nano*, 5(11):9082–9092, 2011.

[144] M. G. Banaee and K. B. Crozier. Mixed Dimer Double-Resonance Substrates for Surface-Enhanced Raman Spectroscopy. *ACS Nano*, 5(1):307–314, 2011.

[145] R. A. Alvarez-Puebla, D. J. Ross, G. A. Nazri, and R. F. Aroca. Surface-Enhanced Raman Scattering on Nanoshells with Tunable Surface Plasmon Resonance. *Langmuir*, 21(23):10504–10508, 2005.

[146] H. Wang and A. Vial. Plasmonic Resonance Tunability and Surface-Enhanced Raman Scattering Gain of Metallic Nanoparticles Embedded in a Liquid Crystal Cell. *The Journal of Physical Chemistry C*, 117(46):24537–24542, 2013.

[147] R. Alvarez-Puebla, B. Cui, J. P. Bravo-Vasquez, T. Veres, and H. Fenniri. Nanoimprinted SERS-Active Substrates with Tunable Surface Plasmon Resonances. *The Journal of Physical Chemistry C*, 111(18):6720–6723, 2007.

[148] C. Lu, H. Möhwald, and A. Fery. Plasmon Resonance Tunable by Deaggregation of Gold Nanoparticles in Multilayers. *The Journal of Physical Chemistry C*, 111 (27):10082–10087, 2007.

[149] A. M. Schwartzberg, C. D. Grant, A. Wolcott, C. E. Talley, T. R. Huser, R. Bogomolni, and J. Z. Zhang. Unique Gold Nanoparticle Aggregates as a Highly Active Surface-Enhanced Raman Scattering Substrate. *The Journal of Physical Chemistry B*, 108(50):19191–19197, 2004.

[150] L. Jensen and G. C. Schatz. Resonance Raman Scattering of Rhodamine 6G as Calculated Using Time-Dependent Density Functional Theory. *The Journal of Physical Chemistry A*, 110(18):5973–5977, 2006.

[151] H. Wei, F. Hao, Y. Huang, W. Wang, P. Nordlander, and H. Xu. Polarization Dependence of Surface-Enhanced Raman Scattering in Gold Nanoparticle-Nanowire Systems. *Nano Letters*, 8(8):2497–2502, 2008.

[152] M. Fan, G. F. S. Andrade, and A. G. Brolo. A review on the fabrication of substrates for surface enhanced Raman spectroscopy and their applications in analytical chemistry. *Analytica Chimica Acta*, 693(1-2):7–25, 2011.

[153] C. L. Haynes and R. P. Van Duyne. Plasmon-Sampled Surface-Enhanced Raman Excitation Spectroscopy. *The Journal of Physical Chemistry B*, 107(30):7426–7433, 2003.

[154] J. P. Camden, J. A. Dieringer, J. Zhao, and R. P. Van Duyne. Controlled Plasmonic Nanostructures for Surface-Enhanced Spectroscopy and Sensing. *Accounts of Chemical Research*, 41(12):1653–1661, 2008.

[155] E. C. Le Ru, E. Blackie, M. Meyer, and P. G. Etchegoin. Surface Enhanced Raman Scattering Enhancement Factors: A Comprehensive Study. *The Journal of Physical Chemistry C*, 111(37):13794–13803, 2007.